UNIVERSITY OF UDINE

Department of Electrical, Management and Mechanical Engineering

Doctorate School in Industrial and Information Engineering

- XXVIII cycle -

Doctoral Thesis

PARAMETER ESTIMATION OF CYCLIC PLASTICITY MODELS AND STRAIN-BASED FATIGUE CURVES IN NUMERICAL ANALYSIS OF MECHANICAL COMPONENTS UNDER THERMAL LOADS

Supervisor:	Candidate:
Prof. Denis Benasciutti	Jelena Srnec Novak

2016

Dedicated to my family…

"All models are wrong; some models are useful."

George E.P. Box

Abstract

The aim of this thesis is to set up a methodological approach to assess a fatigue life of components under cyclic thermal loads. Therefore, a copper mould used for continuous steel casting is considered as a case study. During the process, the molten steel passes through a water cooled mould. The inner part of the component is subjected to a huge thermal flux. Consequently large temperature gradients occur across the component, especially in the region near to the meniscus, and cause elastic and plastic strains.

The finite-element thermo-mechanical analysis is performed with a three-dimensional numerical model. One of the challenging tasks is choosing a suitable material model which is going to be applied in a simulation; since the amount of resulting plastic and elastic strain is strongly controlled by the material model implemented to perform the analysis. Therefore, four different material models (linear kinematic, combined, stabilized and accelerated material model) are investigated and compared in this thesis. It has been found that the combined model requires huge computational time to reach a stabilized stress-strain loop. On the other hand, the use of the stabilized model overestimates the plasticization phenomena already in the first cycle. Accordingly, the alternative accelerated material model, where stabilization is reached earlier, is thus proposed, proofing that it is able to give suitable and safe life estimation for design purposes.

Material coefficients for all applied material and fatigue life models are estimated from experimental, isothermal low cycle fatigue data of CuAg alloy at three temperature levels (20 °C, 250 °C, 300 °C).

A strain-based fatigue model, appropriate to assess a service life of the component, is necessary to apply once the material model is chosen and the finite-element analysis is performed. A fatigue model

compatible and suitable for a daily industrial practice due to its simplicity; however in the same time able to predict precisely a fatigue life. The fatigue life of analysed component is assessed depending on different material models and fatigue models (Universal Slopes equation, Modified Universal Slopes equation, the 10% Rule and 20% Rule), as well as design curves (deterministic approach, tolerance interval, EPI).

Contents

Notation

$\%RA$	Reduction in area
$2N_\mathrm{D}$	Number of reversals to failure with a probability β – Deterministic approach
$2N_\mathrm{f}$	Number of reversals to failure
$2N_\mathrm{t}$	Transition fatigue life
$2N_\mathrm{T}$	Number of reversals to failure – Tolerance interval method
$2N_\mathrm{S}$	Number of reversals to failure with probability β – Student's distribution
A	Actual cross-section area
A_0	Initial cross-section area
A_f	Final cross-section area
b	Speed of stabilization
b^*	Fatigue strength exponent
C	Initial hardening modulus
c	Fatigue ductility exponent
C_in	Initial hardening modulus - initial
C_lin	Initial hardening modulus – Prager's model
D	Ductility

$\mathrm{d}\boldsymbol{\alpha}$	Back stress tensor
$\mathrm{d}\varepsilon$	Strain increment
$\mathrm{d}\varepsilon_{\mathrm{el}}$	Elastic strain increment
$\mathrm{d}\boldsymbol{\varepsilon}_{\mathrm{pl}}$	Plastic strain rate tensor
$\mathrm{d}\varepsilon_{\mathrm{pl,acc}}$	Accumulated plastic strain increment
$\mathrm{d}\lambda$	Scalar of proportionality
$\mathrm{d}\sigma$	Stress increment
E	Young's modulus
e	Residual
E_1	Young's modulus – tensile portion of 1st loop
E_{s}	Young's modulus – stabilized loop
E_{t}	Tangent modulus
F	Force
g	Plastic potential function
h	Beam height
$\boldsymbol{I}$	Unit tensor
k	Elastic-exponential hardening model - material constant
K	Ramsberg-Osgood model - material constant
$K_{\beta,\delta}$	One-side tolerance interval
l	Beam length
l_0	Original length
l_{f}	Total elongation

l_u	Uniform length - elongation
m	Ramsberg-Osgood model - material constant
n	Elastic-exponential hardening model - material constant
N	Number of cycles
n	Sample size
N_f	Number of cycles to failure
p	Probability of survival
q	Thermal flux
q_max	Maximum thermal flux
R	Drag stress
R^2	R-squared - coefficient of determination
R_∞	Saturation stress
R_ε	Strain ratio
S	Standard deviation
S_0	Equivalent standard deviation
S^2	Variance
S_e	Equivalent standard deviation
S_o	Equivalent constant standard deviation
SSE	Sum of squared errors
SSR	Sum of squares due to regression
SST	Total sum of squares
T	Temperature

$\overline{x}$	Mean
X, Y	Coefficient terms of total strain life relation
x, y	Exponent terms of total strain life relation
z	Standard normal variable
α_0	Initial back stress
α_{max}	Maximum back stress
α_{min}	Minimum back stress
β	Probability of survival
γ	Nonlinear recovery parameter
γ_{in}	Nonlinear recovery parameter- initial
δ	Confidence level
$\Delta\varepsilon$	Total strain range
$\Delta\varepsilon_{\mathrm{el}}$	Elastic strain range
$\Delta\varepsilon_{\mathrm{eq}}$	Equivalent strain range
$\Delta\varepsilon_{\mathrm{MUS}}$	Total strain range calculated by Modified Universal Slopes equation
$\Delta\varepsilon_{\mathrm{pl}}$	Plastic strain range
$\Delta\varepsilon_{\mathrm{US}}$	Total strain range calculated by Universal Slopes equation
$\Delta\sigma$	Stress range
$\boldsymbol{\varepsilon}$	Strain tensor
ε	Total strain
$\mathrm{\varepsilon}$	Random variable error
$\varepsilon_{1,2,3}$	Principal strain in 1,2,3 direction

ε_{a}	Strain amplitude
$\varepsilon_{\mathrm{el}}$	Elastic strain
$\varepsilon_{\mathrm{el,a}}$	Elastic strain amplitude
$\varepsilon_{\mathrm{el,x,y,z}}$	Elastic strain in x, y, z direction
$\varepsilon_{\mathrm{f}}'$	Fatigue ductility coefficient
ε_{m}	Mean strain
$\varepsilon_{\mathrm{pl}}$	Plastic strain
$\varepsilon_{\mathrm{pl,0}}$	Initial plastic strain
$\varepsilon_{\mathrm{pl,a}}$	Plastic strain amplitude
$\varepsilon_{\mathrm{pl,acc}}$	Accumulated plastic strain
$\varepsilon_{\mathrm{pl,max}}$	Maximum plastic strain
$\varepsilon_{\mathrm{pl,min}}$	Minimum plastic strain
$\varepsilon_{\mathrm{pl,x,y,z}}$	Plastic strain in x, y, z direction
ε_{t}	True strain
κ	Hardening parameter
ν	Poisson's ratio
σ	Stress
$\boldsymbol{\sigma}$	Stress tensor
$\boldsymbol{\sigma}'$	Stress deviator tensor
σ_0	Initial yield stress
σ_{0*}	Actual yield stress
$\sigma_{1,2,3}$	Principal stress in 1,2,3 direction

σ_{a}	Stress amplitude
$\sigma_{\mathrm{a}*}$	Axial stress
σ_{f}'	Fatigue strength coefficient
$\boldsymbol{\sigma}_{\mathrm{H}}$	Hydrostatic stress tensor
σ_{h}	Hoop stress
σ_{m}	Mean stress
σ_{max}	Maximum stress
$\sigma_{\mathrm{max,1}}$	Maximum stress in 1st cycle
$\sigma_{\mathrm{max},i}$	Maximum stress in i^{th} cycle
$\sigma_{\mathrm{max,s}}$	Maximum stress in stabilized cycle
σ_{min}	Minimum stress
σ_{r}	Radial stress
σ_{t}	True stress
σ_{uts}	Ultimate tensile strength
σ_{vM}	Von Mises stress

List of figures

List of tables

Chapter 1

Introduction

Majority of designed products may contain one or more mechanical components subjected to cyclic loading, causing failures which can be very costly and dangerous. Nowadays, shortening a development time and reducing expenses are just some of main requirements which have to be satisfied during a designing process of a component. Therefore, general practice of oversizing the most critical element cannot be used anymore. As a consequence during a designing process some complex phenomena as plasticity, creep and etc. are necessary take into consideration. Accurate life prediction is crucial to avoid possible catastrophic situations. Over the past few decades, due to expensive prototype testing, finite-element analyses have become very popular, getting important role in designing process. Choosing an appropriate constitutive material model is one of the most important steps during development of a numerical model. A material model has significant influence on design and optimization of components, directly affecting on a lifetime prediction. Very often the choice of a suitable material model is fundamental to produce meaningful results, noting the fact that reliability of lifetime prediction is strongly related with a material model. Depending on application, complex material model should often be used to simulate phenomena as Bauschinger effect, monotonic hardening, cyclic hardening or softening etc. However, complex material models are often characterized by high numbers of material parameters which are necessary to identify from experimental data as accurate as possible. Generally, performing extensive experimental testing is thus expensive and moreover time-consuming.

The aim of this work is to set up a methodological approach able to assess fatigue lives of components under cyclic thermal loads; for this purpose a case of a copper mould is considered as a typical example.

Revision of the state of the art has showed that often problems related with material characterisation and lifetime predictions are addressed separately. Therefore, as a contribution to material modelling and parameter identification, behaviour of a component subjected to cyclic loading and assessment of fatigue lives with respect to several material and fatigue models are described and presented. Furthermore, some gaps which have been found in a literature review will be clarified and explained more clearly.

In general, mechanical components in steelmaking plants are subjected to cyclic thermo-mechanical loading which cause cyclic elasto-plastic behaviour and fatigue damage. A mould is a crucial component of a continuous casting process which control shape and initial solidification of steel products, where a quality of final products is either created or lost. A high temperature of the molten steel causes thermal fluxes and temperature gradients in a mould. As a result, considerable stresses and plastic strains are induced, which leads to deformations and thermal cracks at the inner surface, see Figure 1.1 [Ansoldi, 2012, Ansoldi, 2013, Park, 2002b]. Components without cracks and with close dimensional tolerance contribute to safety in the working process, quality of a steel product and productivity [Park, 2002a, Thomas, 1997].

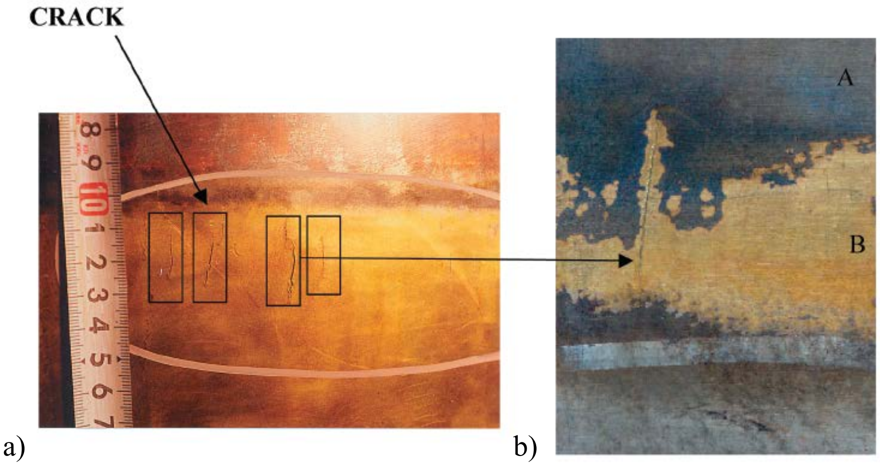

Figure 1.1: a) Photograph of mould cracks and b) magnified view [Park, 2002b]

The finite-element thermo-mechanical analysis is performed with three-dimensional numerical model of the copper mould. A mechanical analysis requires an appropriate material model, able to correctly represent with reasonable accuracy, material behaviour observed in experimental testing to compute a stress-strain distribution. Based on the computed stress-strain distribution is then possible predict the service life of a component. Choosing a suitable material model have to be done carefully, since the amount of resulting plastic and elastic strains is strongly controlled by a material model implemented in analysis.

In the first part of thesis, particular attention is focused on material models for cyclic elasto-plastic behaviour. Several theories concerning elasto–plastic material behaviour have been developed and described in the literature until now [Chaboche, 1983a, Chaboche, 1983b, Chaboche, 1986a, Chaboche, 1986b, Chaboche, 2008, Lemaitre, 1990]. Some of them have become implemented in commercial finite-element software used for every day industrial design. It may be sometimes difficult, especially for non-experienced engineer, to appreciate which model is the most suitable for their application and which material parameter do really affect on the material response. Therefore in Chapter 3, numerical simulations and sensitivity analyses are performed considering several models (Armstrong and Frederick' model, nonlinear isotropic and combined model). Purpose of numerical simulations is to get an overview and link between theoretical and practical use of the several material models. On the other hand, the main goal of sensitivity analyses is to better understand which parameters do really affect and how on the material response. Generally, material models are selected based on their capability to correctly simulate material behaviour observed in experimental testing. Among various elasto-plastic material models available in literature, the combined material model (nonlinear kinematic and nonlinear isotropic model), as suggested by [You, 2008], is found to be the most suitable for applications subjected to cyclic loading. Therefore, the combined material model is adopted for the thermo-mechanical analysis of the copper mould.

Once the material model is selected, the next step is to estimate material parameters by using a suitable identification procedure. By increasing a model complexity number of material parameters to be identified from experiments increases as well as computation time and numerical effort. One of the challenging issues is to find appropriate approach to identify material parameters for the nonlinear kinematic and the nonlinear isotropic models. Several identification procedures of material parameters have been suggested in the literature. Some authors propose to use complex numerical algorithms and optimization routines to estimate multiple parameters simultaneously [Broggiato, 2008, Franulović, 2009, Gong, 2009, Li, 2016, Tong, 2004, Zhao, 2001]. Calibration procedures of the nonlinear kinematic and the nonlinear isotropic parameters require low-cycle fatigue (LCF) experimental data. Thus in the present work, isothermal strain-based low-cycle fatigue experimental test are performed of a CuAg alloy at different temperature levels (20 ^{o}C, 250 ^{o}C and 300 ^{o}C). Numerical simulations with the estimated material parameters are performed. Comparison between simulated and experimental stress-strain loops confirmed that the combined model (nonlinear kinematic and nonlinear isotropic model) is perfectly adequate to represent cyclic elasto-plastic behaviour of CuAg alloy. In addition, mechanical analyses are performed also considering several material models (combined, stabilized, linear kinematic and accelerated model) in order to investigate influence of a material model on cyclic stress-strain response in a component.

Chapter 6 presents strain-based approaches of fatigue, as the Manson-Coffin-Basquin equation. Focus is also on approximated models (Universal Slopes equation, Modified Universal Slopes equation, 10% and 20% Rule proposed in [Manson, 1967, Manson, 1968, Manson, 2006]) that are especially suitable for industrial practice as they can be calibrated on tensile test data. Identification procedure of the Manson-Coffin-Basquin as well as of alternative models (Universal Slopes equation, Modified Universal Slopes equation) is described step-by-step. Furthermore, design curves calculated with deterministic approach, tolerance interval and EPI are presented at the end of Chapter.

As a final step, correlation between several material models (combined, linear kinematic, stabilized and accelerated) and several fatigue models as well as design curves is performed.

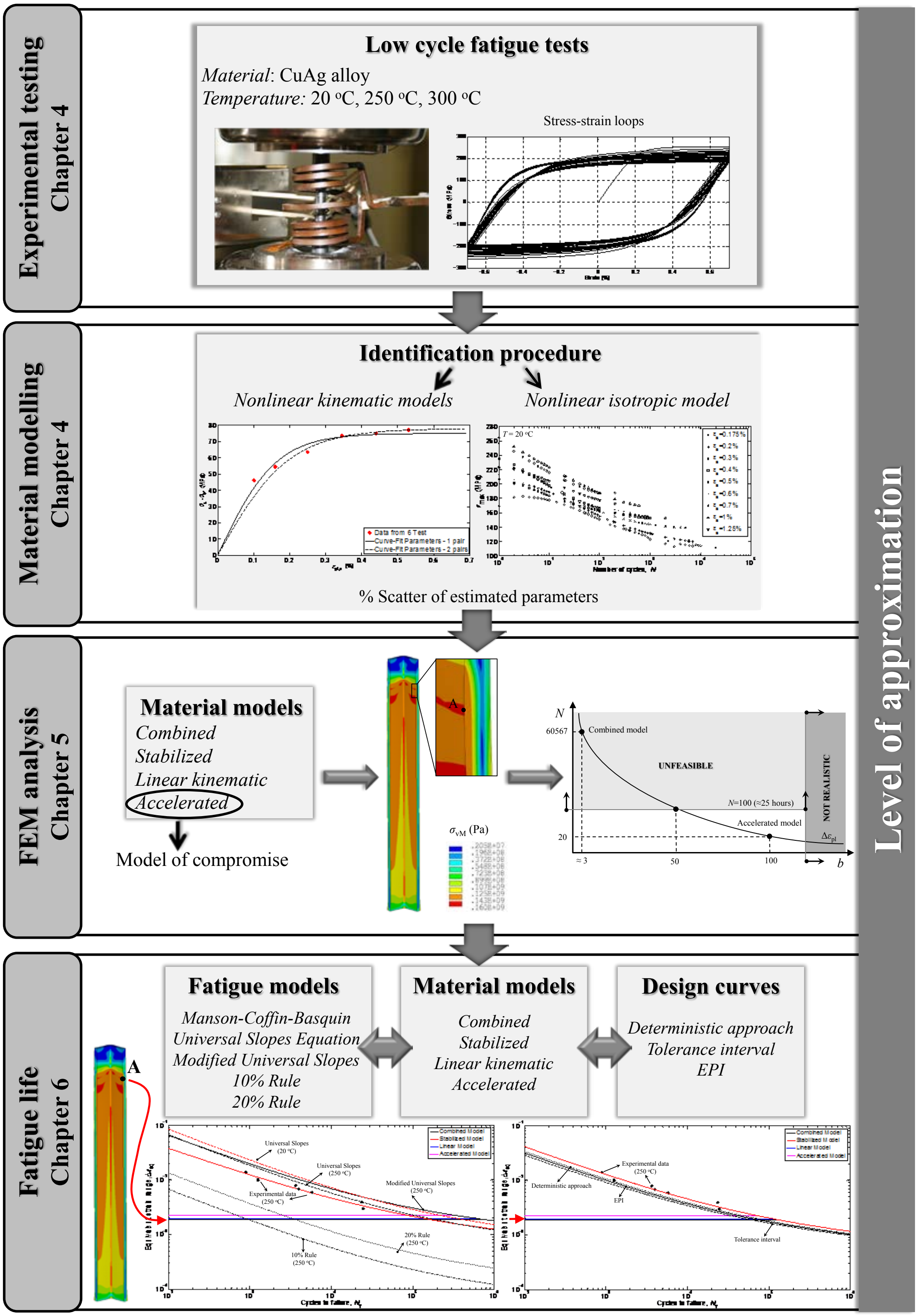

Figure 1.2: Structural organisation of thesis

Thesis is organized in seven chapters. Chapter 1 gives the motivation and the aim of this research work.

Chapter 2 gives an overview of the theoretical background required to understand monotonic and cyclic loading. Furthermore, some of phenomena which can be observed during cyclic loading are briefly described. Various simplified material models suitable to describe elasto-plastic deformation in case of uniaxial monotonic loading are also given.

Chapter 3 describes three main concepts that can be found in the theory of plasticity: the yield criterion, flow rules and hardening models. Hardening models could be divided in two specified groups, namely kinematic and isotropic hardening models. Many different hardening models, capable of capturing elasto-plastic material behaviour under cyclic loadings, have been proposed in the literature [Chaboche, 2008, Lemaitre, 1990]. Some of them are presented and described in this Chapter.

At the beginning of Chapter 4, isothermal low-cycle fatigue (LCF) experimental testing of CuAg alloy at three temperature levels is described. Furthermore, identification procedure of the nonlinear kinematic and the nonlinear isotropic material parameters is described. Calibration of the nonlinear kinematic and the nonlinear isotropic parameters is performed separately, based on isothermal LCF tests of CuAg alloy. Identification procedure of the material parameters for nonlinear kinematic model can be carried out by using different approaches. Parameters for the linear kinematic model are estimated considering the tensile test data. Particular attention, in the last section, is focused on importance of using correct parameters to obtain qualitative results.

Chapter 5 describes, as a case study, the thermo-mechanical analysis of a copper mould used in the continuous casting process. The mould is usually made of copper alloys because of their high conductivity that helps the solidification of the steel. Description of the component and working conditions is given at the beginning of Chapter 5. The material parameters estimated in Chapter 4 are used as input data for the structural analysis. The material behaviour response regarding various material models is evaluated as well. The metallurgical analysis of the copper mould and obtained results are discussed in this Chapter.

Chapter 6 describes several strain-based fatigue models (Manson-Coffin-Basquin equation, Universal Slopes equation, Modified Universal Slopes equation, 10% and 20% Rule), which due to their simplicity and ease of use, are suitable for industrial applications. Particular attention is focused on fatigue models whose parameters can be estimated using simple tensile test data. Parameters for the Universal Slopes equation, the Modified Universal Slopes equation are calibrated from experimental tensile tests data. The Manson-Coffin-Basquin parameters are determined from isothermal LCF test data. Afterwards, several design curves calculated with the deterministic and probabilistic methods are presented. Correlation between the material models (combined, stabilized linear and accelerated model) and the fatigue models (experimental lines, Universal Slopes equation, Modified Universal Slopes equation, 10% Rule and 20% Rule) as well as comparison between the material models and the design curves are performed.

Concluding remarks of the thesis are given in Chapter 7, which highlight the importance of choosing an appropriate material model and a fatigue model to accurately assess service life of a component.

Chapter 2

Behaviour of materials under monotonic and cyclic loading

Chapter 2 provides a short overview regarding materials subjected to monotonic and cyclic loading. Theoretical background of uniaxial monotonic loading is described briefly in order to introduce basic notation which is going to be used in the thesis. Several phenomena can be observed (e.g. hardening, softening, combination of hardening and softening and etc.) once a material is subjected to reversed loading; some phenomena are described in addition. Furthermore, several simplified material models able to quantitatively describe elasto-plastic deformation in case of monotonic loading are presented at the end of this Chapter.

2.1 Uniaxial monotonic test

Uniaxial tensile testing is commonly used for measuring mechanical properties of materials. During the tension test, load is applied to a standard test specimen and causes gradually elongation and eventual fracture of a specimen. Applied load and an amount of elongation are recorded and plotted on a load-elongation curve to calculate stresses and strains. Two types of stress-strain curves are possible to determine based on the load-elongation curve: an engineering stress-strain curve and a true stress-strain curve [ASTM, ASM, 2000, ASM, 2004, Stephens, 2001]. The engineering stress (σ) is defined as:

$$\sigma = \frac{F}{A_0} \tag{2.1}$$

where F is the applied force and A_0 is the initial cross-section area.

The engineering strain (ε) is defined as the ration of the change in length (l-l_0) and the original length (l_0):

$$\varepsilon = \frac{l - l_0}{l_0} = \frac{\Delta l}{l_0} \qquad 2.2$$

Figure 2.1 schematically represents an engineering curve for low carbon steel. The engineering stress-strain curve does not give exact information of material deformation because it is entirely based on the initial cross-section area of a specimen, while during testing the cross-section area is decreasing. The true stress (σ_t) is defined as a ratio of the applied force to the actual cross-section area (A):

$$\sigma_t = \frac{F}{A} \qquad 2.3$$

The true strain (ε_t) is given by:

$$\varepsilon_t = \ln \frac{A_0}{A} \qquad 2.4$$

It should be noted that the true stress is larger than the engineering stress, due to reduction of cross-section area during deformation.

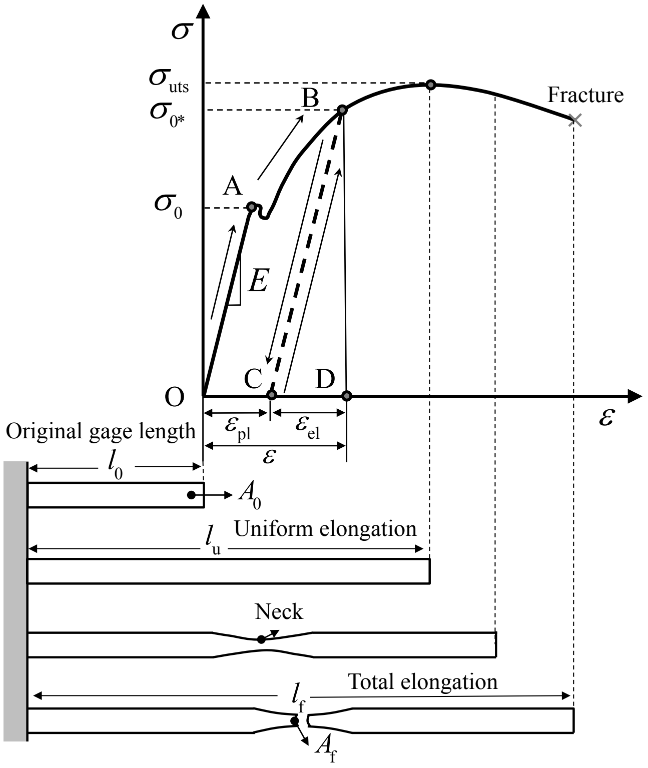

Figure 2.1: Engineering stress-strain curve

Linear portion of a stress-strain curve up to the initial yield stress (σ_0) is known as the elastic region, while a plastic region is placed beyond σ_0. In the elastic region $\sigma < \sigma_0$, the stress-strain relation is described by the Hook's law:

$$\sigma = E \cdot \varepsilon_{\mathrm{el}} \tag{2.5}$$

where E is the Young's modulus, a temperature dependent parameter and $\varepsilon_{\mathrm{el}}$ is the elastic strain. The specimen starts to deform both plastically and elastically with further increasing a load, exceeding the initial yield stress and entering in the plastic region. The total strain (ε) is the sum of the elastic and the plastic strain ($\varepsilon_{\mathrm{pl}}$) components, as shown in Figure 2.1:

$$\varepsilon = \varepsilon_{\mathrm{el}} + \varepsilon_{\mathrm{pl}} \tag{2.6}$$

The Young's modulus, the initial yield stress, the ultimate tensile stress (σ_{uts}) and the reduction in area (%RA) are material parameters obtained from the tension test. The percentage of reduction in area is expressed as:

$$\%RA = \left(\frac{A_0 - A_{\mathrm{f}}}{A_0} \right) \cdot 100 \tag{2.7}$$

where A_{f} is the area of specimen at fracture. Ductility (D) is degree of the plastic deformation that a material can undergo before fracture and it can be expressed by:

$$D = \ln\left(\frac{100}{100 - \%RA} \right) \tag{2.8}$$

2.2 Unloading and reloading

Considering a tensile test, see Figure 2.1, in which a specimen is initially loaded in tension until point B and then unloaded until point C. Both the elastic and the plastic strain occur in the point B. The plastic strain is permanent strain that remains after unloading, while the elastic strain vanishes after unloading. When the load is reduced, the strain decreases following the unloading path BC that is parallel to the initial path OA. Once the load is zero, the total strain is not zero due to amount of the plastic strain which remains in the point C. Amount of the plastic strain in the point C is equal to the OC line, while the CD line represents amount of the elastic strain. When the specimen is reloaded, the stress-strain curve follows the reloading path CB, which is identical with the unloading path BC. The specimen is elastic until the previous maximum reached stress in the point B. Stress in the point B is regarded as the actual yield stress (σ_{0*}), beyond which plastic deformation starts to occur again.

The stress-strain curve continues to rise although a slope becomes progressively less once the initial yield stress is reached; thus the actual yield stress increases with further straining. The effect when a material is able to withstand the greater stress after plastic deformation is known as the strain hardening or the work hardening [Chen, 1988, Lemaitre, 1990].

2.3 Reverse loading

In the late 19th century, Baushinger has observed that the stress-strain behaviour in monotonic tension or compression (Figure 2.2 a and b) is different from the stress-strain behaviour obtained once the cyclic load is applied (Figure 2.2 c). Baushinger has indicated that the magnitude of the yield stress is reduced, if the load is first applied in one direction causing plastic deformation (e.g. in tension) and then in the opposite direction (e.g. in compression). When a load is firstly applied in a tension and then in compression, as illustrated in Figure 2.2 c), the yield stress in compression (σ_{0**}) is significantly reduced regarding to initial yield stress in tension (σ_0). In fact the yield stress (σ_{0**}) is lower than the initial yield stress (σ_0) and much lower than the actual yield stress (σ_{0*}). Described phenomenon is known as the *Bauschinger effect* [Chen, 1988, Lemaitre, 1990].

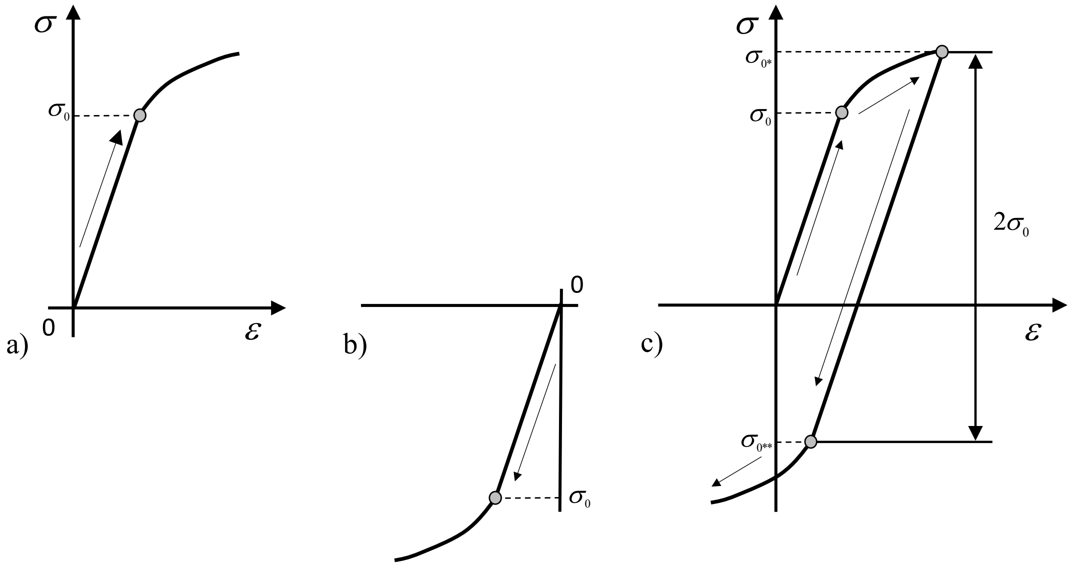

Figure 2.2: a) Loading in tension; b) Loading in compression; c) Tension loading followed by compression loading

2.4 Cyclic stress-strain behaviour

Assuming a material which is strain cyclically loaded between two fixed limits. Firstly, a material is strained up to the positive value $+\varepsilon_a$ by the tensile force; then the tensile force is removed and the compressive force is applied up to the value $-\varepsilon_a$. Briefly, a material is subjected to alternate strains $\pm \varepsilon_a$ indefinitely number of times. Figure 2.3 shows a stress-strain loop obtained after first cycle. The stress-strain loop is characterized by the total strain range ($\Delta\varepsilon$) and the stress range ($\Delta\sigma$).

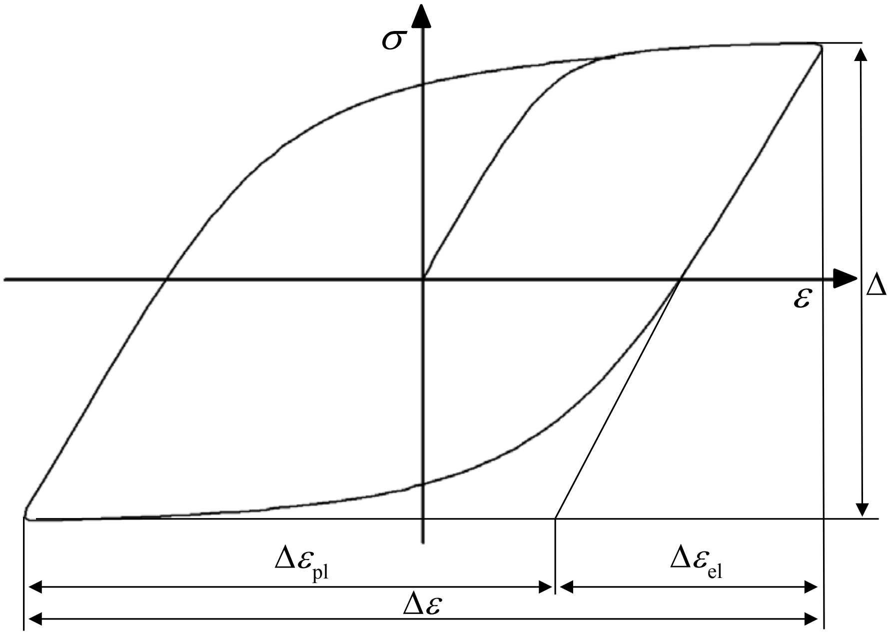

Figure 2.3: Stress-strain hysteresis loop

The total strain range can be decomposed into the elastic range ($\Delta\varepsilon_{el}$) and the plastic strain range ($\Delta\varepsilon_{pl}$) components [Chen, 1988, Lemaitre, 1990]:

$$\Delta\varepsilon = \Delta\varepsilon_{el} + \Delta\varepsilon_{pl} \tag{2.9}$$

The elastic strain range is related to the stress range ($\Delta\sigma \equiv \sigma_{max}-\sigma_{min}$) by:

$$\Delta\varepsilon_{el} = \frac{\Delta\sigma}{E} \tag{2.10}$$

Let

$$\varepsilon_a \equiv \frac{\Delta\varepsilon}{2};\ \varepsilon_{el,a} \equiv \frac{\Delta\varepsilon_{el}}{2};\ \varepsilon_{pl,a} \equiv \frac{\Delta\varepsilon_{pl}}{2}$$

define the strain amplitude (ε_{a}), the elastic strain amplitude ($\varepsilon_{\mathrm{el,a}}$) and the plastic strain amplitude ($\varepsilon_{\mathrm{pl,a}}$), respectively. With the stress amplitude ($\sigma_{\mathrm{a}} \equiv \Delta\sigma/2$), additional decomposition of the strain amplitude can be rewritten as:

$$\varepsilon_{\mathrm{a}} = \frac{\sigma_{\mathrm{a}}}{E} + \varepsilon_{\mathrm{pl,a}} \tag{2.11}$$

Material stress-strain response is affected by cyclic loading. A stress required to achieve straining, as shown in Figure 2.3, do not remain constant but change as cycling proceeds. The manner in which stress vary depends on type of a material and can be classify into three different categories: hardening, softening and combination of hardening and softening.

2.5 Effect of cyclic loading: hardening and softening

For strain controlled loading, the hardening is said to occur when the stress range progressively increases to maintain the same strain range as cycling proceeds, see Figure 2.4 a. The stress range settles down to an aproximately constant value after certain number of cycles. Value at which the stress settles down is known as the saturated stress range and depends on the imposed strain range. The saturated stress range is reached often within 10% to 40% of the total life. Since, the stress range is rather constant over a large part of live; the stabilized cycle is defined as the cycle that corresponds to the mid-life of the specimen, i.e. equal to the half number of cycles required to failure. In case of stress controlled loading, the hardening is said to occur when the strain range progressively decreases to maintain the same stress range as the cycling proceeds as can be seen in Figure 2.4 b, or when the stress range increases in a stress controlled test, see Figure 2.4 a. On the other hand, the softening is said to occure when the stress range decreases with successive cycles under controlled strain (Figure 2.4 c), or when the strain range increases in a stress controlled test, see Figure 2.4 d. [Coffin, 1972, Lemaitre, 1990, Manson, 1965, Manson, 1966, Stephens, 2001]

Hardening and/or softening phenomena are more pronounced at the beginning of cyclic loading. Some materials like copper, stainless steels show significant softening/hardening, while other materials (e.g. structural steel) do not show so obviously this phenomenon. Furthermore, some materials harden at the beginning of cyclic loading and after certain number of cycles start to soften. Properties of cyclic hardening or softening do not depend only on material microstructure, temperature, but also on loading amplitude or more generally on previous strain history. Both phenomena are believed to be associated with stability of the dislocation substructure within the metal crystal lattice of a material [Halama, 2012, Lemaitre, 1990].

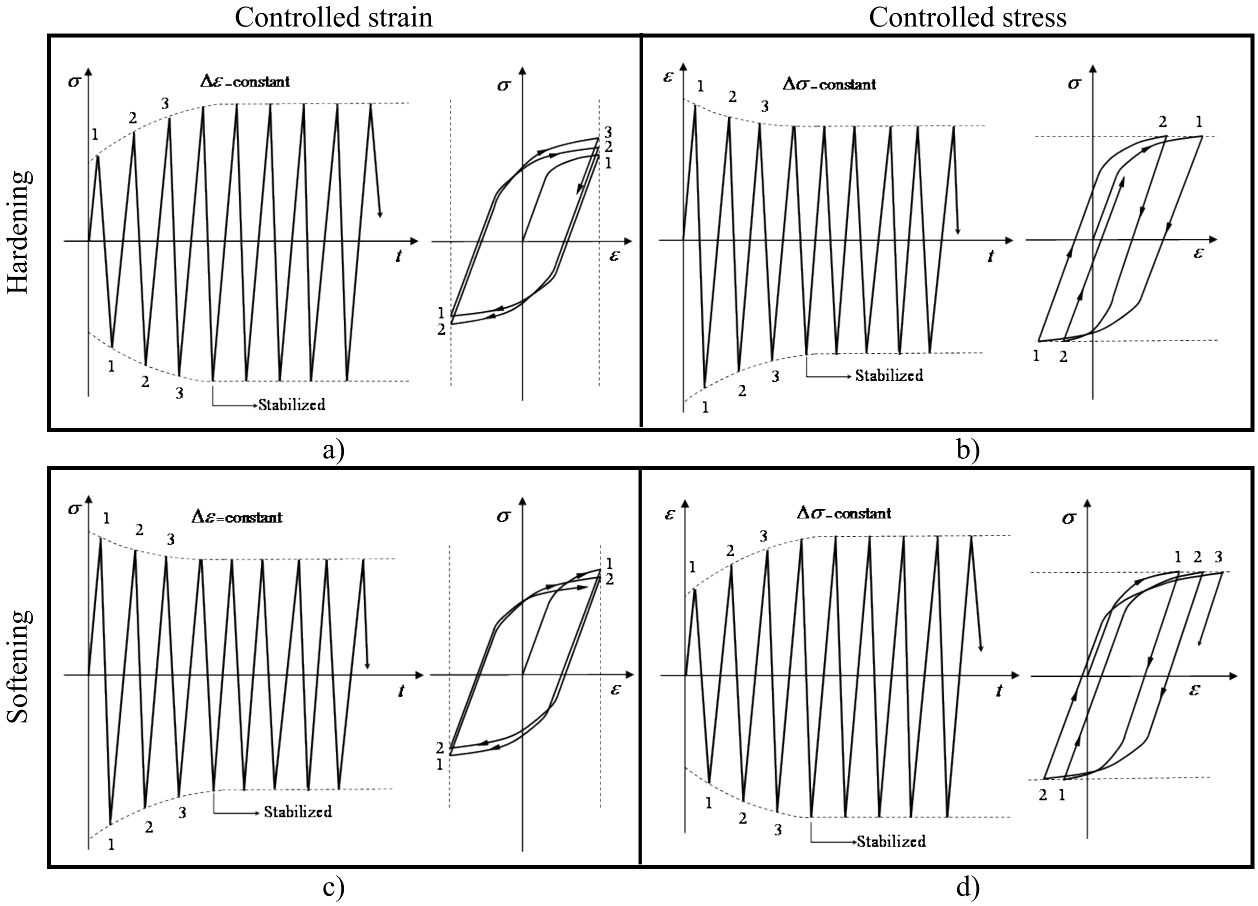

Figure 2.4: Phenomena of cyclic hardening and softening

Manson observed that the ration of monotonic ultimate strenght (σ_{uts}) to the 0.2% offset yield strenght (σ_0) can be used to predict whether the material will soften or harden. If $\sigma_{uts}/\ \sigma_0 >1.4$, a material is likely to cyclically strain harden; while a material is likely to soften if $\sigma_{uts}/\ \sigma_0<1.2$ [Manson, 2006].

2.6 Simplified uniaxial monotonic stress-strain curves

Several simplified models have been proposed in literature to describe quantitatively the elasto-plastic deformation of materials. Some of them are presented and described in the following paragraphs.

2.6.1 Elastic-perfectly plastic model

The elastic-perfectly plastic model assumes a null strain-hardening effect, i.e. the plastic deformation occurs as the stress reaches the yield stress. As can be seen in Figure 2.5, the uniaxial stress-strain diagram beyond the yield stress is approximated by a horizontal straight line with a constant stress level σ_0. The relation for the elastic-perfectly plastic model can be expressed as [Chen, 1988]:

$$\begin{cases} \varepsilon = \dfrac{\sigma}{E} & \text{for } \sigma < \sigma_0 \\ \varepsilon = \infty & \text{for } \sigma = \sigma_0 \end{cases} \qquad 2.12$$

Using elasto-perfectly plastic model can lead to drastic simplification of an analysis. However, in some applications (e.g. for studying processes where material is worked at a high temperature –such as hot rolling) are allowed and suitable to neglect the effect of strain hardening

2.6.2 Elastic-linear strain hardening model

The elastic-linear strain hardening model supposes that the continuous curve is approximated with two straight lines. As can be seen in Figure 2.6, the first line has a slope of Young's modulus, while the second straight line presents an idealization for the strain hardening range and has a slope which corresponds to the tangent modulus (E_t), where $E_t < E$. The stress-strain relation is expressed by [Chen, 1988]:

$$\begin{cases} \varepsilon = \dfrac{\sigma}{E} & \text{for } \sigma \le \sigma_0 \\ \varepsilon = \dfrac{\sigma_0}{E} + \dfrac{1}{E_t}(\sigma - \sigma_0) & \text{for } \sigma > \sigma_0 \end{cases} \qquad 2.13$$

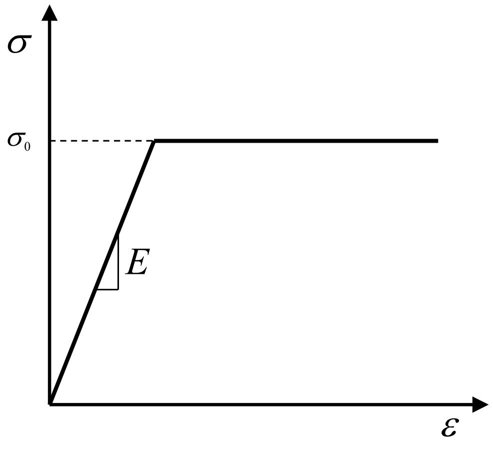

Figure 2.5: Elastic-perfectly plastic model

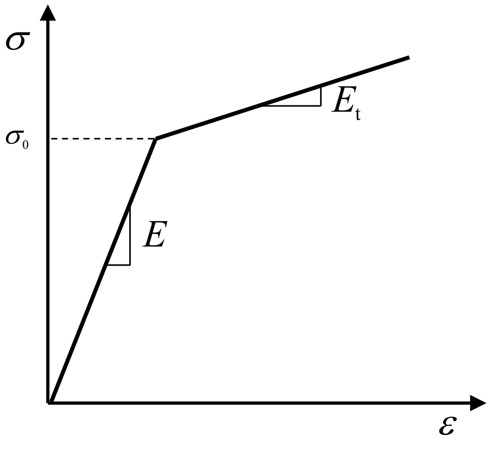

Figure 2.6: Elastic-linear strain hardening model

2.6.3 Elastic-exponential hardening model

As can be seen in Figure 2.7, the elastic-exponential hardening model is defined with the Hooke's law (valid within the elastic region) and with the power expression (valid in the plastic region when $\sigma > \sigma_0$):

$$\begin{cases} \sigma = E\varepsilon \ \text{ for } \sigma \le \sigma_0 \\ \sigma = k\varepsilon^n \ \text{ for } \sigma > \sigma_0 \end{cases} \tag{2.14}$$

where k and n are two material constants which should be determined from the experimental curve. The curve should pass through the point representing the yield stress and the corresponding elastic strain, if ε represents the total strain [Chen, 1988].

2.6.4 Ramberg-Osgood model

The Ramberg-Osgood model (1943) assumes decomposition of the total strain into the elastic and the plastic strain components:

$$\varepsilon = \varepsilon_{\text{el}} + \varepsilon_{\text{pl}} = \frac{\sigma}{E} + \left(\frac{\sigma}{K}\right)^{\frac{1}{m}} \tag{2.15}$$

where K and m are material constants. The initial slope of the stress-strain curve takes value of the Young's modulus at $\sigma = 0$ and decreases monotonically with increasing loading, Figure 2.8. Since the model has two parameters, it allows obtaining a better agreement between experimental and simulated curves. The value of m gives a measure of the material's strain hardening behaviour and it is usually between 0 and 0.5 [Chen, 1988, Stephens, 2001].

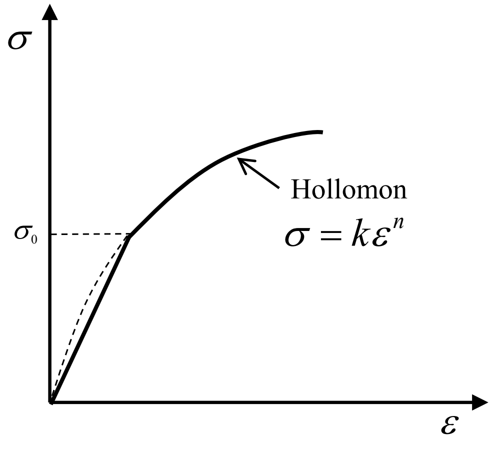

Figure 2.7: Elastic-exponential hardening model

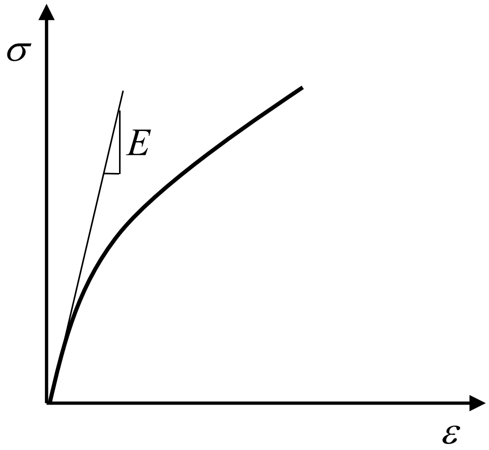

Figure 2.8: Ramberg-Osgood model

Chapter 2 gives briefly theoretical overview of several topics (uniaxial monotonic loading, cyclic loading, hardening and softening phenomena, and etc). Discussed topics are theoretical base of the work presented in the following sections. Notation used thought the thesis is also defined in this Chapter. Several simplified models (elastic-perfectly plastic, the elastic-linear strain hardening, the elastic-exponential hardening and Ramberg-Osgood model), suitable to quantitatively describe the plastic deformation for the monotonic case of loading, are presented. Following Chapter 3 presents models that can be used for both monotonic and cyclic loading cases as well as gives overview of three main concepts which can be found in the theory of plasticity.

Chapter 3

Theoretical plasticity models

Chapter 3 gives an overview of three main concepts which can be found in the theory of plasticity: the yield criterion, the flow rule and hardening models. The yield criterion is needed to define the limit of elasticity, i.e. the limit at which material becomes plastic. The flow rule describes the relationship between an applied stress increment and a resulting plastic strain increment once a material has become plastic. In addition, the rule defines magnitude and direction of the plastic flow. Hardening models take into consideration evolution of the yield surface by describing the change in the yield criterion as a function of plastic strain. The subsequent yield stress, of a material subjected to reversed loading, is usually determined by one of two models: kinematic and/or isotropic models. Several material models have been developed and described in the literature over the years. However, only few kinematic and isotropic models are theoretically presented in this Chapter.

Numerical simulations are performed considering the simple numerical model and adopting several material models. The goal of performed activities is to get an overview and a link between theoretical and practical use of material models. In addition, sensitivity analyses are done in order to understand better which parameters do really affect and how on a material response. Obtained results are described and presented in the second part of Chapter 3.

3.1 Stress deviator tensor and plastic strain increment tensor

In material modelling, the stress tensor ($\boldsymbol{\sigma}$) is convenient to split into two parts the hydrostatic stress tensor ($\boldsymbol{\sigma}_{\mathrm{H}}$) and the stress deviator tensor ($\boldsymbol{\sigma}'$). The stress tensor can be written [Chen, 1988, Lemaitre, 1990]:

$$\boldsymbol{\sigma}=\begin{bmatrix}\sigma_{11} & \sigma_{12} & \sigma_{13}\\ \sigma_{21} & \sigma_{22} & \sigma_{23}\\ \sigma_{31} & \sigma_{32} & \sigma_{33}\end{bmatrix}=\begin{bmatrix}\sigma_{\mathrm{H}} & 0 & 0\\ 0 & \sigma_{\mathrm{H}} & 0\\ 0 & 0 & \sigma_{\mathrm{H}}\end{bmatrix}+\begin{bmatrix}\sigma_{11}-\sigma_{\mathrm{H}} & \sigma_{12} & \sigma_{13}\\ \sigma_{21} & \sigma_{22}-\sigma_{\mathrm{H}} & \sigma_{23}\\ \sigma_{31} & \sigma_{32} & \sigma_{33}-\sigma_{\mathrm{H}}\end{bmatrix} \qquad 3.1$$

The hydrostatic stress is an average of the three stress components:

$$\sigma_{\mathrm{H}}=\frac{1}{3}\left(\sigma_1+\sigma_2+\sigma_3\right) \qquad 3.2$$

where σ_1, σ_2, σ_3 are principal stresses in 1, 2, and 3 direction, respectively. The hydrostatic stress tensor is given by:

$$\boldsymbol{\sigma}_{\mathrm{H}}=\sigma_{\mathrm{H}}\boldsymbol{I}=\begin{bmatrix}\sigma_{\mathrm{H}} & 0 & 0\\ 0 & \sigma_{\mathrm{H}} & 0\\ 0 & 0 & \sigma_{\mathrm{H}}\end{bmatrix} \qquad 3.3$$

where $\boldsymbol{I}$ is the unit tensor. The stress deviator tensor is obtained by subtracting the hydrostatic stress tensor from the stress tensor:

$$\boldsymbol{\sigma}'=\boldsymbol{\sigma}-\boldsymbol{\sigma}_{\mathrm{H}}=\begin{bmatrix}\sigma_{11}-\sigma_{\mathrm{H}} & \sigma_{12} & \sigma_{13}\\ \sigma_{21} & \sigma_{22}-\sigma_{\mathrm{H}} & \sigma_{23}\\ \sigma_{31} & \sigma_{32} & \sigma_{33}-\sigma_{\mathrm{H}}\end{bmatrix} \qquad 3.4$$

The plastic strain rate tensor ($\mathrm{d}\boldsymbol{\varepsilon}_{\mathrm{pl}}$) can be expressed as:

$$\mathrm{d}\boldsymbol{\varepsilon}_{\mathrm{pl}}=\begin{bmatrix}\mathrm{d}\varepsilon_{\mathrm{pl},11} & \mathrm{d}\varepsilon_{\mathrm{pl},12} & \mathrm{d}\varepsilon_{\mathrm{pl},13}\\ \mathrm{d}\varepsilon_{\mathrm{pl},21} & \mathrm{d}\varepsilon_{\mathrm{pl},22} & \mathrm{d}\varepsilon_{\mathrm{pl},23}\\ \mathrm{d}\varepsilon_{\mathrm{pl},31} & \mathrm{d}\varepsilon_{\mathrm{pl},32} & \mathrm{d}\varepsilon_{\mathrm{pl},33}\end{bmatrix} \qquad 3.5$$

The accumulated plastic strain increment ($\mathrm{d}\varepsilon_{\mathrm{pl,acc}}$) is defined as [Chaboche, 2008, Lemaitre, 1990]:

$$\mathrm{d}\varepsilon_{\mathrm{pl,acc}}=\sqrt{\frac{2}{3}\mathrm{d}\boldsymbol{\varepsilon}_{\mathrm{pl}}:\mathrm{d}\boldsymbol{\varepsilon}_{\mathrm{pl}}} \qquad 3.6$$

where the symbol ':' is called the double contracted product, or double dot product, of two second order tensors (e.g. $\boldsymbol{A}$ and $\boldsymbol{B}$). Multiply component by component and sum the terms gives a scalar quantity:

$$A:B=\sum_{i=1}^{n}\sum_{j=1}^{n}A_{ij}B_{ij} \qquad 3.7$$

3.2 Yield criterion

The limit of elasticity in uniaxial state of stress is defined by the yield stress. However, exact value at which material starts to plastically deform is not so trivial to give when several stress components are present and act simultaneously. The yield criterion defines the limit of elasticity of a material under combined state of stress and mathematically can be expressed as [Besson, 2010, Dunne, 2005, Lemaitre, 1990, Stephens, 2001]:

$$f\left(\boldsymbol{\sigma}\right)=0 \tag{3.8}$$

For isotropic materials, the yield function can be visualized as a yield surface in three dimensional stress space in which each of coordinate axes represents the one principal stress. The yield surface divides the stress space into the elastic and the plastic regions; the elastic deformation occurs when $f(\boldsymbol{\sigma}) < 0$, while the plastic deformation occurs when $f(\boldsymbol{\sigma}) = 0$. Several criterions can be found in literatures to describe the yield surface [Besson, 2010]. Only the von Mises yield criterion is considered here.

The von Mises is commonly used yield criterion for ductile materials [Besson, 2010, Dunne, 2005, Lemaitre, 1990, Stephens, 2001]:

$$f\left(\boldsymbol{\sigma}\right)=\sigma_{\mathrm{vM}}-\sigma_0=\sqrt{\frac{3}{2}\boldsymbol{\sigma}':\boldsymbol{\sigma}'}-\sigma_0=0 \tag{3.9}$$

where σ_{vM} is the von Mises stress. The von Mises stress can be expressed in terms of principal stresses as:

$$\sigma_{\mathrm{vM}}=\frac{1}{\sqrt{2}}\sqrt{\left(\sigma_1-\sigma_2\right)^2+\left(\sigma_2-\sigma_3\right)^2+\left(\sigma_3-\sigma_1\right)^2} \tag{3.10}$$

As can be seen in Figure 3.1, the von Mises criterion is visualized as a circular cylinder that is orthogonal to a deviatoric plane in the stress space and parallel to the hydrostatic axis $\sigma_1 = \sigma_2 = \sigma_3$. The criterion becomes an ellipse considering the plane state of stress ($\sigma_3 = 0$) as can be seen in Figure 3.2 [Besson, 2010, Dunne, 2005].

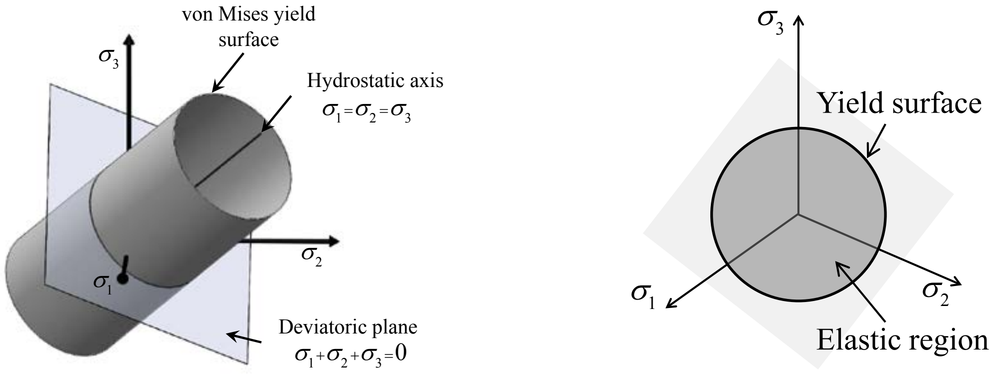

Figure 3.1: The von Mises yield surface

3.3 Flow rules

The flow rule relates stresses and plastic strains once the plastic deformation has begun. Equations which relate stress increments and plastic stains increments are called constitutive equations and are typically based on the normality condition. The normality condition states that the increment of a plastic strain caused by an increment of stress is such that the vector representing the plastic strain increment is normal to the yield surface during the plastic deformation [Stephens, 2001].

In 1928, von Mises proposed the concept of the plastic potential function (*g*), which is a scalar function of the stresses. The plastic flow equation, based on the plastic potential function, can be written in the form [Chen, 1988, Lee, 2012, Lemaitre, 1990]:

$$\mathrm{d}\boldsymbol{\varepsilon}_{\mathrm{pl}} = \mathrm{d}\lambda \frac{\partial g}{\partial \boldsymbol{\sigma}} \qquad 3.11$$

where dλ is a positive scalar of proportionality, which is nonzero only when the plastic deformation occur. Several flow rules have been proposed in the literature over the years, however, only the associated flow rule is considered and explained in addition.

The associated flow rule assumes that the plastic potential function and the yield function coincide ($g = f$). Based on this assumption, equation (3.11) is possible to rewrite as [Chen, 1988, Lee, 2012]:

$$\mathrm{d}\boldsymbol{\varepsilon}_{\mathrm{pl}} = \mathrm{d}\lambda \frac{\partial f}{\partial \boldsymbol{\sigma}} \qquad 3.12$$

Direction of the plastic strain increment is given with $\partial f/\partial \boldsymbol{\sigma}$ and it is a vector normal to surface. The strain increment can be plotted as a vector normal to the surface with a length determined by dλ, as shown in Figure 3.2.

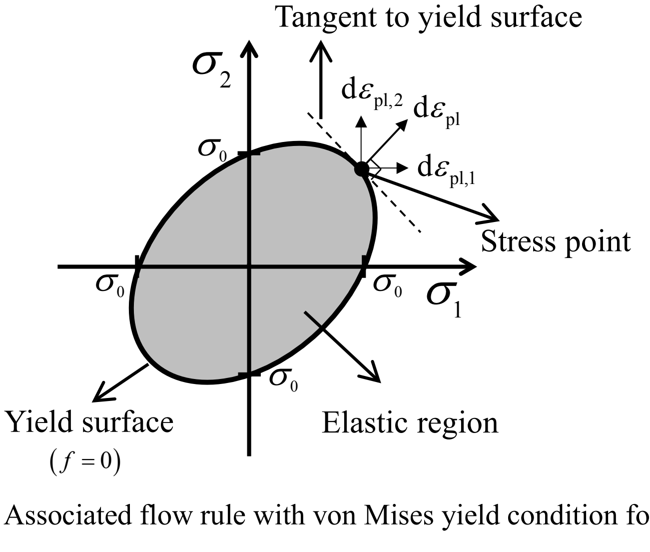

Figure 3.2: Associated flow rule with von Mises yield condition for plane stress

3.4 Loading surface

The subsequent yield surface for an elasto-plastically deformed material is called the loading surface. Three different conditions are possible to occur when a stress point is considered to be on the surface: unloading, neutral loading and loading, see Figure 3.3. The plastic deformation will not occur when the stress point is considered to be within loading surface. On the other hand, the additional plastic deformation occurs if the stress point is on the surface and tends to move out of the current loading surface, simultaneously causing change of the current loading surface. The loading surface can change size, shape, position and be described as [Chen, 1988, Lemaitre, 1990]:

$$f\left(\boldsymbol{\sigma},\kappa\right)=0 \tag{3.13}$$

where κ represents one or more hardening parameter (parameter may be scalar or higher order tensor), which changes during the plastic deformation and defines evolution of the yield surface. The hardening parameters are zero when material starts to deform plastically for a first time:

$$f\left(\boldsymbol{\sigma},0\right)=f_0\left(\boldsymbol{\sigma}\right) \tag{3.14}$$

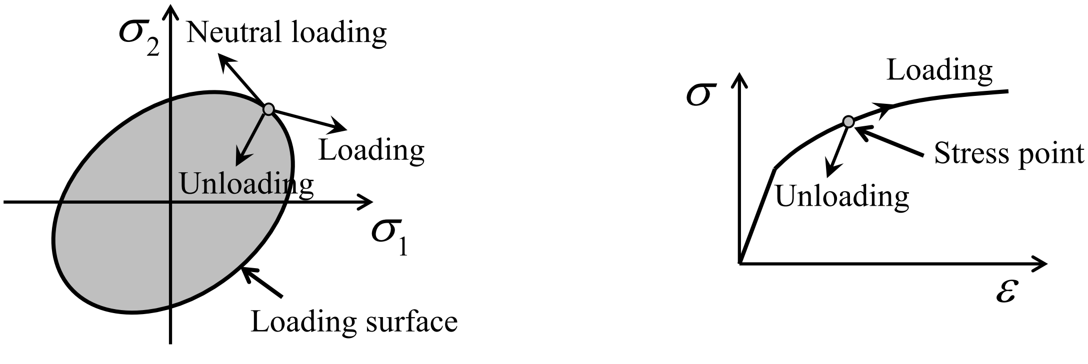

a) Multiaxial case b) Uniaxial case

Figure 3.3: Loading criterion for a strain hardening material

One of major problems in the strain hardening theory is to determine nature of the subsequent loading surface. Response of a material after initial yielding mainly depends on a considered plasticity model.

3.5 Hardening models

Many hardening models have been developed and described in literatures until now. Some of them can be found in [Chaboche, 1983a, Chaboche, 1983b, Chaboche, 1986a, Chaboche, 1986b, Chaboche, 1989, Chaboche, 2008, Lemaitre, 1990]. Hardening models describe change in the yield criterion as a function of the plastic strain. Generally, the hardening phenomenon is described with one of two specific types:

namely kinematic and isotropic hardening. The kinematic and the isotropic hardening are described in this section.

3.5.1 Kinematic hardening material models

Kinematic hardening material models assume translation of the loading surface as a rigid body in the stress space simultaneously maintaining size, shape and orientation of the initial yield surface. The kinematic hardening captures the Bauschinger effect as a consequence of an assumption that the loading surface translates as a rigid body (i.e. the elastic range is assumed to be unchanged during hardening) [Chen, 1988, Silvestre, 2015]. Considering the von Mises criterion, the yield function is convenient to write as [Dunne, 2005, Chaboche, 1986a, Lemaitre, 1990]:

$$f(\boldsymbol{\sigma},\kappa)=\sqrt{\frac{3}{2}(\boldsymbol{\sigma}'-\boldsymbol{\alpha}'):(\boldsymbol{\sigma}'-\boldsymbol{\alpha}')}-\sigma_0=0 \qquad 3.15$$

The back stress, $\boldsymbol{\alpha}$, indicates present position of the loading surface (i.e. centre of the loading surface), which may be shifted as a result of the kinematic hardening mechanism; while $\boldsymbol{\alpha}'$ is the deviatoric part of $\boldsymbol{\alpha}$. The back stress has the same components as the stress; therefore, it can be written as tensor and considered as a deviator because of the plastic incompressibility [Lemaitre, 1990].

3.5.1.1 Linear kinematic hardening – Prager's model

Prager (1949) proposed the linear kinematic hardening model which assumes collinear relation between increment of the kinematic variable (d$\boldsymbol{\alpha}$) and the plastic strain increment [Chaboche, 1986a, Chaboche, 2008, Dunne, 2005, Lemaitre, 1990]:

$$\mathrm{d}\boldsymbol{\alpha}=\frac{2}{3}C\mathrm{d}\boldsymbol{\varepsilon}_{\mathrm{pl}} \qquad 3.16$$

The initial hardening modulus, *C*, is temperature dependent material parameter. The yield surface, under applied load which causes the plastic deformation, translates to a new location. The initial centre is translated by $\boldsymbol{\alpha}$.

The Prager's model is schematically illustrated in Figure 3.4. Imagine a specimen which is firstly loaded up to the point B and then until the point B'. Both the elastic and the plastic deformations occur in the point B while only the elastic deformation appears between the points B and B'. However, the elasto-plastic deformation occurs again when an applied load pass the point B'. Radius of the yield surface is equal to the initial yield stress confirming that the linear kinematic hardening model is able to capture the Bauschinger effect. The main advantage of this model is having only one material parameter, *C*.

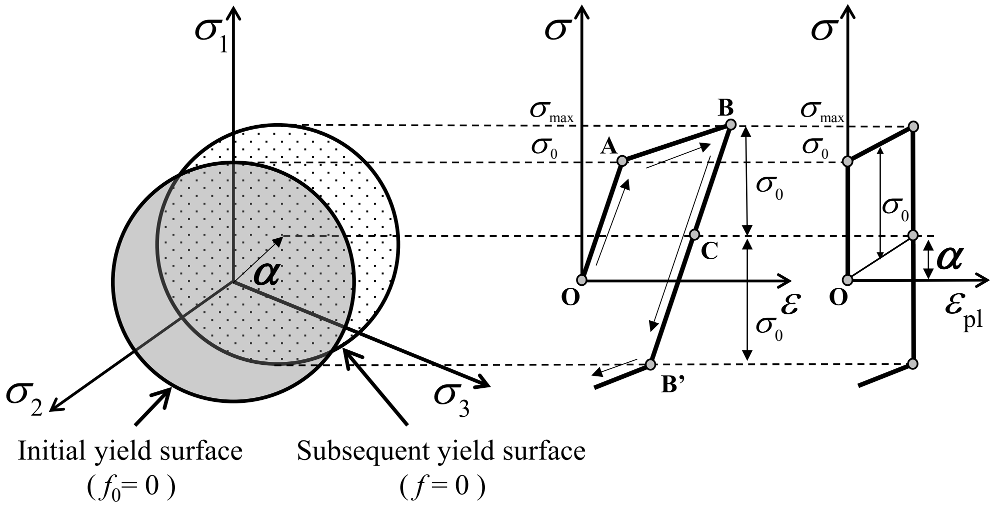

a) Stress space b) Tension-compression

Figure 3.4: Evolution of the linear kinematic hardening model

As can be seen in Figure 3.4, the negative aspect of the Prager's model is that transition from the elastic to the plastic region is not smooth; i.e. it is described with a sharp angle which connects two straight lines. It would be much better that transition is defined with a continuous curve in order to get more realistic curve.

3.5.1.2 Nonlinear kinematic hardening –Armstrong and Frederick's model

Armstrong and Frederick (1966) proposed more complex nonlinear kinematic hardening model to obtain smoother transition from the elastic to the plastic region. Proportionality between $\mathrm{d}\boldsymbol{\varepsilon}_{\mathrm{pl}}$ and $\mathrm{d}\boldsymbol{\alpha}$ is eliminated by adding, on the Prager's model, a recall term which introduces a fading memory effect to the strain path [Chaboche, 1986a, Chaboche, 2008, Lemaitre, 1990]:

$$\mathrm{d}\boldsymbol{\alpha} = \frac{2}{3} C \mathrm{d}\boldsymbol{\varepsilon}_{\mathrm{pl}} - \gamma \boldsymbol{\alpha} \mathrm{d}\varepsilon_{\mathrm{pl,acc}} \qquad 3.17$$

The nonlinear recovery parameter, γ, is temperature dependent material parameter while $\mathrm{d}\varepsilon_{\mathrm{pl,acc}}$ is the increment of the accumulated plastic strain. The recall term affects to the plastic flow differently for tensile or compressive loading because it depends on $|\mathrm{d}\varepsilon_{\mathrm{pl}}|$ and it is important in predicting a nonlinear stress-strain loop under cyclic loading [Khan, 1995]. The nonlinear recovery parameter controls the rate at which the initial hardening modulus decreases with increasing the plastic strain. Moreover, γ determines the rate of stress saturation. Evolution of the back stress instead of being linear is now exponential for monotonic uniaxial loading.

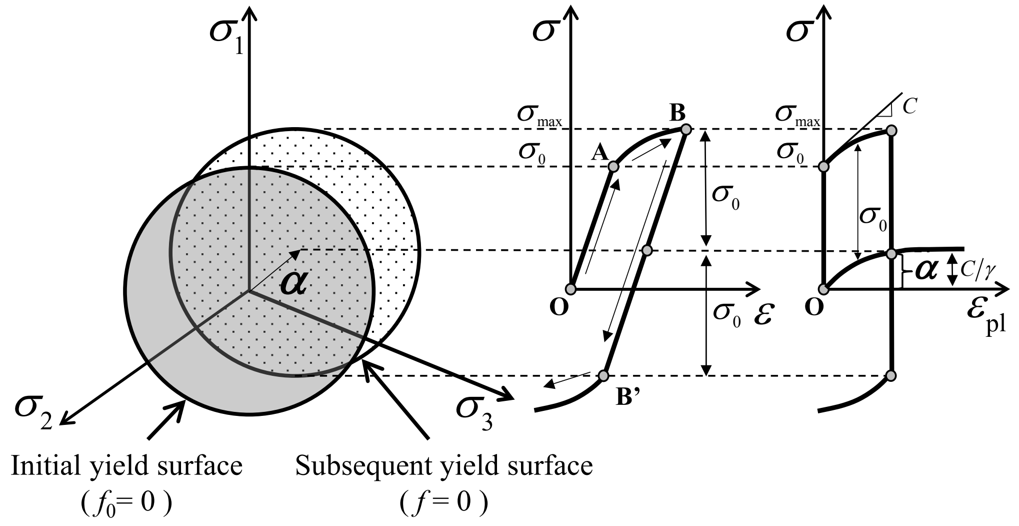

a) Stress space b) Tension-compression

Figure 3.5: Evolution of the nonlinear kinematic hardening model

Considering a component that has been loaded following the loading path O-A-B-B', see Figure 3.5, a material starts to elasto-plastic deform after passing the initial yield stress (the point A). In this case, the transition from the elastic to the plastic region is smooth. The back stress increases with the increasing the plastic strain and saturates to the value C/γ; giving the maximum saturated stress equal to $\sigma_0 + C/\gamma$. Shape of the stress-strain curve, obtained using the nonlinear kinematic hardening model, is more similar to the form of experimental stress-strain curves. For uniaxial case of loading, where $\sigma = \sigma_{11} \neq 0$ and $\sigma_{22} = \sigma_{33} = 0$, von Mises criterion (equation 3.15) can be written as [Chaboche, 1986a, Lemaitre, 1990]:

$$f = \left|\sigma - \alpha\right| - \sigma_0 = 0 \tag{3.18}$$

Considering assumption of the plastic incompressibility, $\mathrm{d}\varepsilon_{\mathrm{pl}} = \mathrm{d}\varepsilon_{\mathrm{pl},11} \neq 0$, $\mathrm{d}\varepsilon_{\mathrm{pl},22} = \mathrm{d}\varepsilon_{\mathrm{pl},33} = -1/2\ \mathrm{d}\varepsilon_{\mathrm{pl}}$, gives the accumulated plastic strain equal to:

$$\mathrm{d}\varepsilon_{\mathrm{pl,acc}} = \sqrt{\frac{2}{3}\mathrm{d}\boldsymbol{\varepsilon}_{\mathrm{pl}} : \mathrm{d}\boldsymbol{\varepsilon}_{\mathrm{pl}}} = \left|\mathrm{d}\varepsilon_{\mathrm{pl}}\right| \tag{3.19}$$

The nonlinear hardening model (expressed with equation 3.17) may be written as:

$$\mathrm{d}\alpha = C\mathrm{d}\varepsilon_{\mathrm{pl}} - \gamma\alpha\left|\mathrm{d}\varepsilon_{\mathrm{pl}}\right| \tag{3.20}$$

Essential difference between two plastic strain increment terms $\mathrm{d}\boldsymbol{\varepsilon}_{\mathrm{pl}}$ and $\mathrm{d}\varepsilon_{\mathrm{pl,acc}}$ is that they give rise to $\mathrm{d}\varepsilon_{\mathrm{pl}}$ and $|\mathrm{d}\varepsilon_{\mathrm{pl}}|$, respectively. Thus, nonlinearity introduced by the recall term is not the same during the flow under the tensile or the compressive loading. Relation between α and $\varepsilon_{\mathrm{pl}}$ is no unique and the concavity of the stress-strain curve is correctly reproduced [Chaboche, 1986a]. For tension-compression, the absolute value is possible to dispose using multiplier $\psi = \pm 1$ (where $\psi = \pm 1$ depends on direction of the plastic flow):

$$\begin{aligned} \mathrm{d}\alpha &= C\mathrm{d}\varepsilon_{\mathrm{pl}} - \gamma\alpha\left|\mathrm{d}\varepsilon_{\mathrm{pl}}\right| \\ &= C\mathrm{d}\varepsilon_{\mathrm{pl}} - \gamma\alpha\psi\mathrm{d}\varepsilon_{\mathrm{pl}} \\ &= \left(C - \gamma\alpha\psi\right)\mathrm{d}\varepsilon_{\mathrm{pl}} \end{aligned} \tag{3.21}$$

Separating the variables and assuming initial values $\varepsilon_{\mathrm{pl,0}}$ and α_0 for the plastic strain and the back stress, respectively; where initial values correspond to $\varepsilon_{\mathrm{pl}}$ and α at the beginning of a considered loading branch, finally gives:

$$\int_{\alpha_0}^{\alpha} \frac{\mathrm{d}\alpha}{C - \gamma\alpha\psi} = \int_{\varepsilon_{\mathrm{pl,0}}}^{\varepsilon} \mathrm{d}\varepsilon_{\mathrm{pl}} \tag{3.22}$$

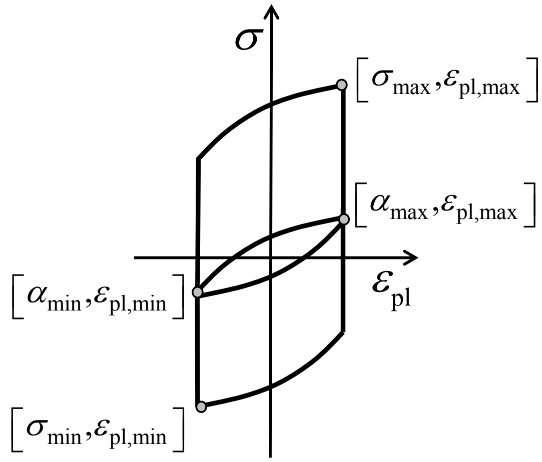

Figure 3.6: Initial conditions for the back stress and the plastic strain

Integration with respect to $\varepsilon_{\mathrm{pl}}$, for uniaxial loading, gives relation for the back stress:

$$\alpha = \psi\frac{C}{\gamma} + \left(\alpha_0 - \psi\frac{C}{\gamma}\right)\exp\left[-\psi\gamma\left(\varepsilon_{\mathrm{pl}} - \varepsilon_{\mathrm{pl,0}}\right)\right] \tag{3.23}$$

As illustrated in Figure 3.5 b), the stress at each moment can be expressed as:

$$\sigma = \psi\sigma_0 + \alpha \tag{3.24}$$

In case of monotonically loading (e.g. in tension $\psi = 1$) and considering zeros initial values of the plastic strain and the back stress, the equation (3.23) becomes:

$$\alpha = \frac{C}{\gamma}\left[1 - \exp\left(-\gamma\varepsilon_{\mathrm{pl}}\right)\right] \tag{3.25}$$

Equation (3.25) is proposed to use for identification of material parameters C and γ using a single stabilized stress-strain loop [Chaboche, 1986a, Chaboche, 2008, Lemaitre, 1990]. Limit values of the parameters (C and γ) show the influence on stress-strain response of the nonlinear kinematic hardening model:

$$\lim_{\varepsilon_{\mathrm{pl}}\to 0} C\exp\left(-\gamma\varepsilon_{\mathrm{pl}}\right) = C \tag{3.26}$$

$$\lim_{\varepsilon_{\mathrm{pl}}\to \infty} \sigma_0 + \frac{C}{\gamma}\left[1-\exp\left(-\gamma\varepsilon_{\mathrm{pl}}\right)\right] = \sigma_0 + \frac{C}{\gamma} \tag{3.27}$$

The back stress, α, saturates to C/γ for sufficiently large ($\varepsilon_{\mathrm{pl}}$ - $\varepsilon_{\mathrm{pl},0}$) [Hu, 1999]. Maximum ($\sigma_{\max}$, $\varepsilon_{\max}$) and minimum ($\sigma_{\min}$, $\varepsilon_{\min}$) values are constant in the stabilized cycle. The plastic strain at end of the loading branch is an initial value of the unloading branch. The maximum back stress, in case of tension (ψ = 1), can be expressed using equation (3.23) as:

$$\alpha_{\max} = \frac{C}{\gamma} + \left(\alpha_{\min} - \frac{C}{\gamma}\right)\exp\left[-\gamma\left(\varepsilon_{\mathrm{pl,max}} - \varepsilon_{\mathrm{pl,min}}\right)\right] \tag{3.28}$$

where $\varepsilon_{\mathrm{pl,max}}$ is the maximum plastic strain and $\varepsilon_{\mathrm{pl,min}}$ is the minimum plastic strain. Similarly, the minimum back stress, for compression (ψ = -1), is expressed as:

$$\alpha_{\min} = -\frac{C}{\gamma} + \left(\alpha_{\max} + \frac{C}{\gamma}\right)\exp\left[\gamma\left(\varepsilon_{\mathrm{pl,min}} - \varepsilon_{\mathrm{pl,max}}\right)\right] \tag{3.29}$$

Specifying the plastic strain range as $\Delta\varepsilon = \varepsilon_{\max} - \varepsilon_{\min}$, the stress range $\Delta\sigma = \sigma_{\max} - \sigma_{\min}$ and using fact that:

$$\sigma_{\max} = \alpha_{\max} + \sigma_{0*} \tag{3.30}$$

$$\sigma_{\min} = \alpha_{\min} - \sigma_{0*} \tag{3.31}$$

Relation between the half stress range and the half strain range under stabilized cycling can be obtained by substituting equation (3.28) to (3.29):

$$\frac{\Delta\sigma}{2} = \sigma_0 + \frac{C}{\gamma}\tanh\left(\gamma\frac{\Delta\varepsilon_{\mathrm{pl}}}{2}\right) \tag{3.32}$$

Stabilization in the nonlinear kinematic model occurs only if the loading is symmetrical (zero mean stress). Quantitatively, the model describes the ratchet effect under nonzero mean stress [Chaboche, 1986a].

3.5.1.3 Nonlinear kinematic hardening – Chaboche's model

The nonlinear kinematic hardening model proposed by Chaboche is obtained by superimposing two or more nonlinear kinematic hardening models proposed by Armstrong & Frederick [Chaboche, 1986a, Chaboche, 1989, Chaboche, 2008, Lemaitre, 1990]:

$$\boldsymbol{\alpha} = \sum_{i}^{m} \boldsymbol{\alpha}_i \qquad 3.33$$

Each of the kinematic variables $\boldsymbol{\alpha}_i$ works independently:

$$\mathrm{d}\boldsymbol{\alpha}_i = \frac{2}{3} C_i \mathrm{d}\boldsymbol{\varepsilon}_{\mathrm{pl}} - \gamma_i \boldsymbol{\alpha}_i \mathrm{d}\varepsilon_{\mathrm{pl,acc}} \qquad 3.34$$

The range of validity is widened using the Chaboche's model. Three kinematic variables (m = 3) are sufficient to cover strain ranges between 0.01% and 4% [Chaboche, 1986a]. Superposition of several Armstrong & Frederick' models are able to describe more accurate three critical segments of a stable hysteresis curve:

1) initial modulus when yielding starts to occur,
2) nonlinear transition of the hysteresis curve after yielding starts until the curve becomes linear again and
3) linear segment of the curve in the range of higher strain.

In the form of Chaboche model, equation (3.32) may be written as [Halama, 2012, Lemaitre, 1990]:

$$\frac{\Delta\sigma}{2} = \sigma_0 + \sum_{i}^{m} \frac{C_i}{\gamma_i} \tanh\left(\gamma_i \frac{\Delta\varepsilon_{\mathrm{pl}}}{2}\right) \qquad 3.35$$

3.5.2 Isotropic hardening material models

The isotropic hardening material models assume symmetrically enlargement of the yield surface under the plastic deformation without changing its centre or shape. Moreover, isotropic hardening models are able to capture cyclic hardening and/or softening behaviour of a material. An amount of the yield surface expansion is taken to be a function of the accumulated plastic strain, i.e. the accumulated plastic strain is assumed to be the hardening parameter ($\varepsilon_{\mathrm{pl,acc}} = \kappa$). Considering the von Mises criterion, the yield function is convenient to write as [Dunne, 2005, Chaboche, 1986a, Chaboche, 2008, Lemaitre, 1990]:

$$f\left(\boldsymbol{\sigma},\kappa\right) = \sqrt{\frac{3}{2}\boldsymbol{\sigma}' : \boldsymbol{\sigma}'} - \sigma_{0*}\left(\varepsilon_{\mathrm{pl,acc}}\right) = 0 \qquad 3.36$$

where $\sigma_{0*}(\varepsilon_{\mathrm{pl,acc}})$ is the actual yield stress and might have a form:

$$\sigma_{0*}\left(\varepsilon_{\mathrm{pl,acc}}\right)=\sigma_0+R\left(\varepsilon_{\mathrm{pl,acc}}\right) \tag{3.37}$$

where $R(\varepsilon_{\mathrm{pl,acc}})$ is the isotropic hardening function. Many isotropic hardening models have been developed until now. In addition some of models are presented and described.

3.5.2.1 Linear isotropic hardening model

The linear isotropic hardening material model assumes that the evolution of the loading surface is governed only by one scalar variable ($\varepsilon_{\mathrm{pl,acc}}$). To simplify the presentation, the rule is developed assuming constant temperature or at least using criteria which are temperature independent [Dunne, 2005, Lemaitre, 1990]:

$$R=R(\varepsilon_{\mathrm{pl,acc}}) \tag{3.38}$$

in which R is the drag stress and describes size of the yield surface. Figure 3.7 schematically shows the isotropic hardening model in terms of the von Mises criterion. In case that applied load in the point B continues to increase in tension until the point M or if in the point B is applied a load in compression until the point M', an amount of the accumulated plastic strain is the same in both cases due to OI+IP=OI+IP'. As can be noticed in Figure 3.7, the isotropic hardening is able to capture uniquely enlargement of yield surface in all direction. Value of the actual yield stress in tension $\sigma_{0*}=\sigma_B$ is equal to the actual yield stress in compression $\sigma_{B'}$. Consequently, the isotropic hardening model neglects completely the Bauschinger effect.

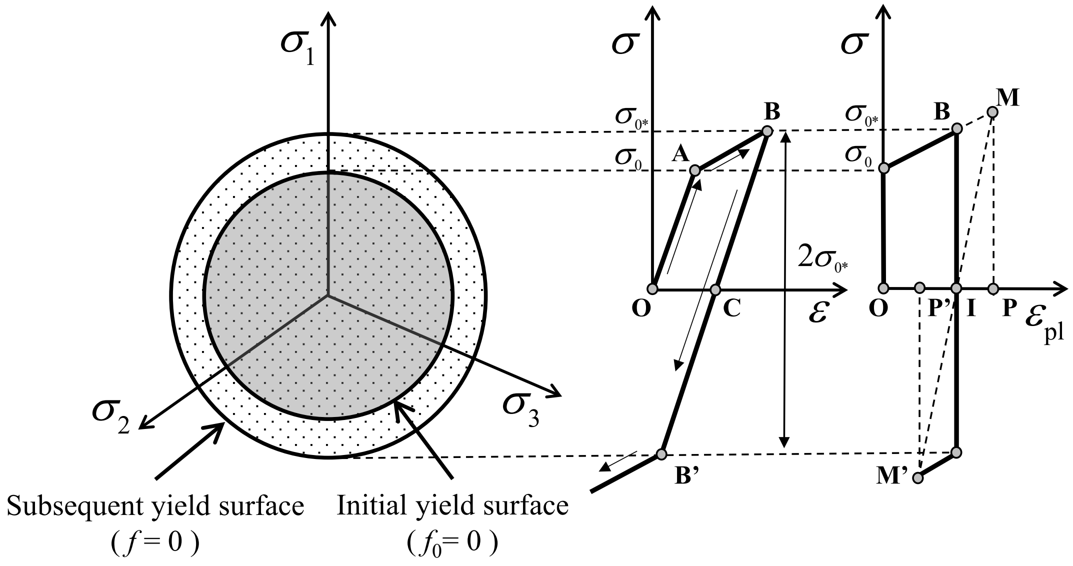

a) Stress space b) Tension-compression

Figure 3.7: Evolution of the linear isotropic hardening model

3.5.2.2 Nonlinear isotropic hardening model

The evolution of the yield surface size may be expressed with the nonlinear isotropic hardening model [Chaboche, 1989, Chaboche, 2008, Lemaitre, 1990]:

$$\mathrm{d}R\left(\varepsilon_{\mathrm{pl,acc}}\right) = b\left(R_{\infty} - R\right)\mathrm{d}\varepsilon_{\mathrm{pl,acc}} \tag{3.39}$$

where b indicates the speed of stabilization and R_{∞} is the saturated stress (maximum increment) of R. Both material parameters are temperature dependent. The achieved peak of the stress is equal to (σ_0+R_{∞}), obtained from equation (3.37). The relation between R and $\varepsilon_{\mathrm{pl,acc}}$ is obtained after integration:

$$R = R_{\infty}\left[1-\exp\left(-b\varepsilon_{\mathrm{pl,acc}}\right)\right] \tag{3.40}$$

R_{∞} can be either positive or negative, giving rise to cyclic hardening or softening, respectively. Moreover, R stabilizes after certain number of cycles to the value of R_{∞}. The saturated stress is in fact difference between the maximum stress of the first cycle ($\sigma_{\mathrm{max,1}}$) and the stabilized one ($\sigma_{\mathrm{max,s}}$). The application of the given criterion to each uniaxial cycle gives:

$$\sigma_{\mathrm{max}} = \sigma_0 + R_{\infty}\left[1-\exp\left(-b\varepsilon_{\mathrm{pl,acc}}\right)\right] \tag{3.41}$$

Assuming $\Delta\varepsilon_{\mathrm{pl}}$ to be approximately constant, the accumulated plastic strain can be written as:

$$\varepsilon_{\mathrm{pl,acc}} = 2\Delta\varepsilon_{\mathrm{pl}}N \tag{3.42}$$

in which N is the number of cycle. Finally is obtained relation which is proposed by [Lemaitre, 1990] to identify the speed of stabilization:

$$\frac{\sigma_{\mathrm{max},i} - \sigma_{\mathrm{max,1}}}{\sigma_{\mathrm{max,s}} - \sigma_{\mathrm{max,1}}} \approx \frac{R}{R_{\infty}} = 1-\exp\left(-b\varepsilon_{\mathrm{pl,acc}}\right) = 1-\exp\left(-2b\Delta\varepsilon_{\mathrm{pl}}N\right) \tag{3.43}$$

where $\sigma_{\mathrm{max,i}}$ is the current maximum stress for the N^{th} cycle.

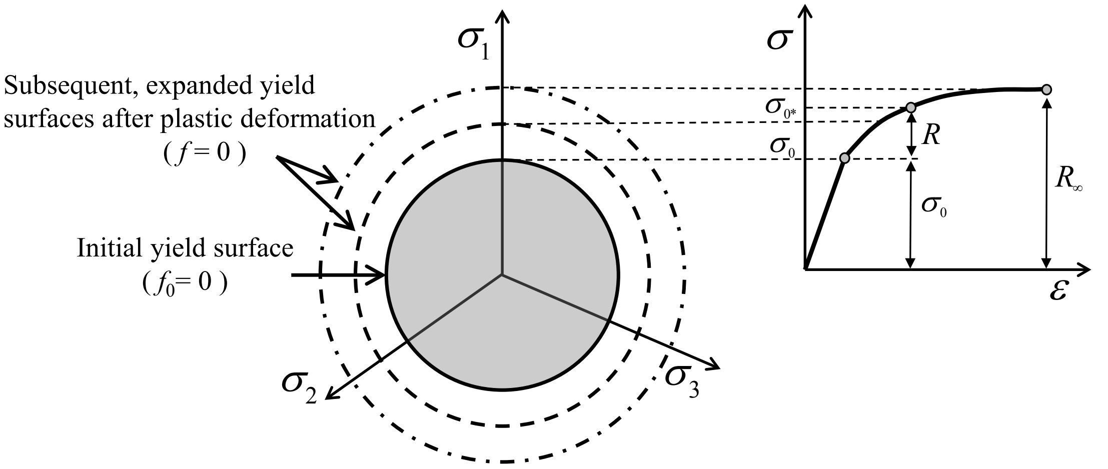

a) Stress space b) Tension-compression

Figure 3.8: Evolution of the nonlinear isotropic hardening model

3.5.3 Combined hardening material model

General, materials subjected to cyclic loading harden both kinematically and isotropically. Combination of the isotropic and the kinematic hardening model provides uniform expansion and translation of the yield surface in the stress space simultaneously [Dunne, 2005, Lemaitre, 1990, Lemaitre, 2005, Silvestre, 2015]. The kinematic hardening model is dominant hardening process for an individual cycle to capture the Bauschinger effect. On the other hand, the isotropic hardening model simulates cyclic hardening or softening phenomenon over cycles. Considering the von Mises criterion, the yield function is convenient to write as:

$$f\left(\boldsymbol{\sigma},\kappa\right)=\sqrt{\frac{3}{2}\left(\boldsymbol{\sigma}'-\boldsymbol{\alpha}'\right):\left(\boldsymbol{\sigma}'-\boldsymbol{\alpha}'\right)}-R-\sigma_0=0 \qquad 3.44$$

Major difference between the kinematic and the isotropic hardening model is that isotropic hardening is described by a scalar variable R, whereas the hardening variable $\boldsymbol{\alpha}$ is a tensor in the kinematic model. It should be noted that neither the kinematic and/or isotropic hardening models are capable to truly representative real material behaviour, which can be quite complex and complicated. Nevertheless, in some cases such as in proportional loading, these models are able to provide satisfactory results. The maximum stress, once the model reaches stabilized condition, is equal to:

$$\sigma_{\max}=\sigma_0+\frac{C}{\gamma}+R_{\infty} \qquad 3.45$$

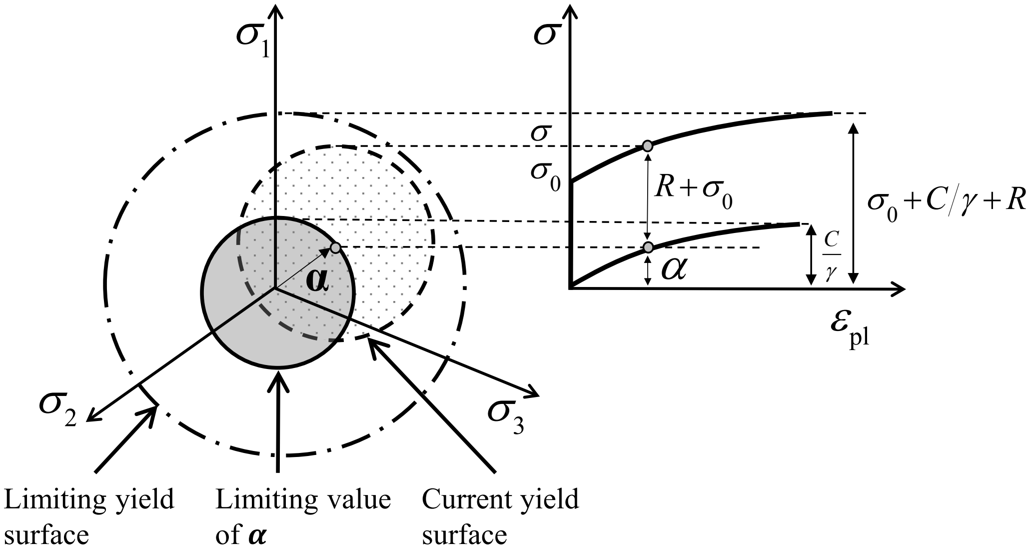

a) Stress space b) Tension-compression

Figure 3.9: Evolution of the combined hardening model

3.5.4 Accelerated material model

The accelerated material model, proposed by [Chaboche, 1986a] is in fact the combined model which takes into consideration the speed of stabilization, *b*. Therefore, the model is able to capture the monotonic hardening associated with the cyclic hardening or softening phenomenon. However, with this model is possible to control the speed of stabilization by increasing or decreasing the coefficient *b*. The number of cycles needed to reach the stabilized condition is smaller by imposing the higher value of the *b* parameter.

3.5.5 Stabilized material model

The stabilized material model, proposed by [Chaboche, 1986a], assumes condition of a material when it reaches the stabilization (i.e. when R reaches R_∞), simultaneously neglecting cyclic hardening or softening phenomenon. In other words, the stabilized model is almost equal to the nonlinear kinematic model. Parameters (C and γ) are identical to those described in paragraphs 3.5.1.2 and 3.5.1.3. However, the main difference between these two models is that the stabilized model neglects the initial state of a material and takes into consideration the Young's modulus (E_s) and the actual yield stress (σ_{0*}) calculated from stabilized experimental stress-strain curves. Instead, the kinematic model takes into consideration initial state of a material, i.e. the initial Young's modulus (E_1) and the initial yield stress (σ_0). Differences between initial values of E_1, σ_0 and stabilized values E_s, σ_{0*} are described more in details in the paragraphs 4.2.1 and 4.2.2.

3.6 Numerical simulations and sensitivity analyses with respect to material models

So far, several material models (the kinematic, the isotropic and the combined) have been theoretically presented. The kinematic and the isotropic material models have been already implemented in commercial FEM codes to provide accurate prediction of material behaviour and different phenomenon such as the Bauschinger effect, cyclic hardening or softening and etc. The aim of this paragraph is to get a link between theoretical part and practical use of material models.

The numerical simulations and the sensitivity analyses are done in order to understand better difference between several material models (the nonlinear kinematic, the nonlinear isotopic and the combined material model). Similar numerical simulations have been done in [Lee, 2009]. Moreover, sensitivity analyses are performed to comprehend clearer which parameters do really affect and how on the material response.

A simple numerical model, shown in Figure 3.10, is created and used to simulate cyclic loading. The numerical model is constrained at the bottom and at the top is imposed fully reversed triangular waveform of displacement ($\Delta l = \pm 1$ mm) as indicated in Figure 3.11. Figure 3.11 shows also the finite element mesh with boundary conditions.

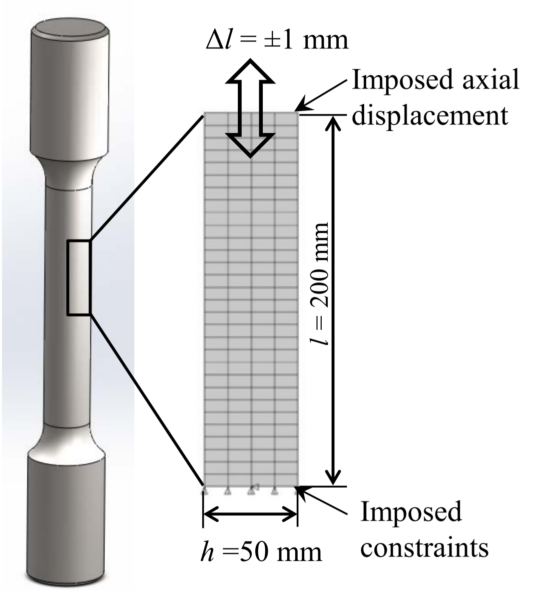

Figure 3.10: Model used in numerical simulation

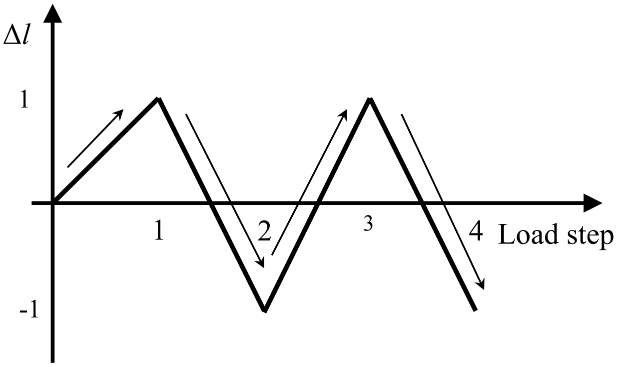

Figure 3.11: Strain imposed on a model

In this way, proportional strain controlled loading is simulated with the strain amplitude equal to:

$$\varepsilon_{\mathrm{a}} = \frac{\Delta l}{l} = 0,5\% \tag{3.46}$$

where l is the length of the model. Two dimensional 8 node elements are used to create the finite element model (PLANE183 in ANSYS®). Each simulation demonstrates 20 cycles or 40 load steps. The material parameters used in simulations are taken from [You, 2008] and presented in Table 3.1. Data for stress-strain curves are taken in a node at the top in the centre of the model, far from constraints.

Table 3.1: Material parameters

			Nonlinear kinematic model		Nonlinear isotropic model	
E (GPa)	σ_0 (MPa)	v	C (MPa)	γ	R_∞ (MPa)	b
125	100	0.36	64257	888	76	8

3.6.1 Nonlinear kinematic hardening – Armstrong & Frederick's model

The numerical simulation is performed using the numerical model described in Figure 3.10 and adopting the Armstrong and Frederick's model.

The Chaboche model has been already implemented in the Ansys® code as a given option inside structural – nonlinear – inelastic – rate independent section. The Ansys® has a possibility to superimpose up to five the Armstrong and Frederick's models simultaneously taking into consideration temperature dependence or independence of material parameters. In this case, the Armstrong and Frederick's model is defined by imposing only the one pair of C, γ and assuming temperature independence of material parameters.

Resulting stress-strain loops obtained from the numerical simulation are illustrated in Figure 3.12. As can be seen in Figure 3.12, the model starts to plastically deform once it passes the yield stress (σ_0=100 MPa). Firthermore, the model stabilizes after first cycle confirming the statement of [Chaboche, 1986] in which it states that the stabilization occurs very fast in case of symmetrical loading with zero mean stress. According to equation 3.32, the maximum stress when model reaches the stabilization is equal to:

$$\sigma_{\max} = \sigma_0 + \frac{C}{\gamma} = 172 \text{ MPa} \qquad 3.47$$

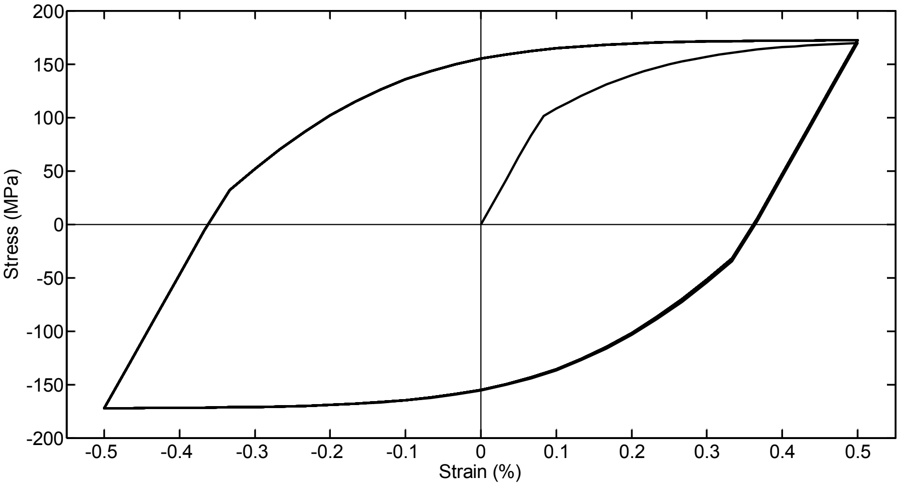

Figure 3.12: Armstrong & Frederick's material model - stress-strain curves

As can be seen in Figure 3.13, the Armstrong and Frederick's model is able to capture the Bauschinger effect and monotonic hardening. However, the model is unable to simulate cyclic hardening/softening, according to theory presented in paragraph 3.5.1.2.

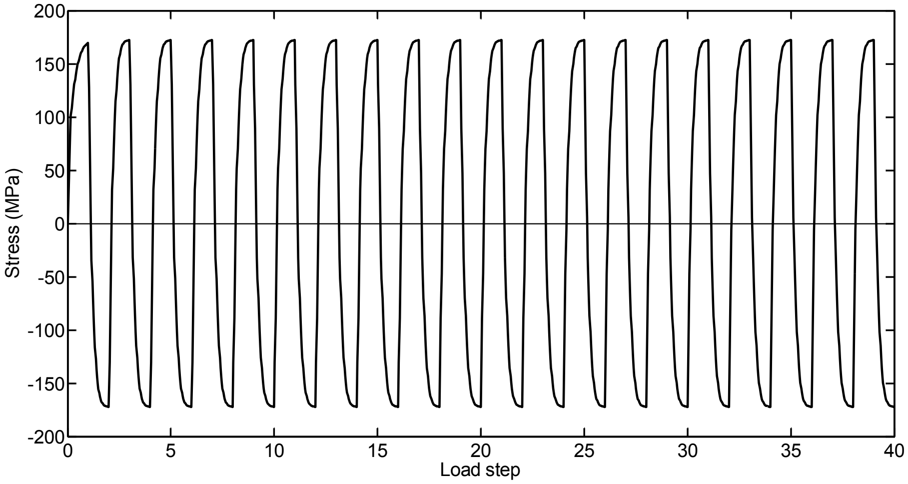

Figure 3.13: Armstrong & Frederick's material model – stress vs. load steps

Sensitivity analysis of nonlinear kinematic hardening material parameters - C, γ

The aim of sensitivity analysis is to investigate how C and γ define shape of stress-strain loops. Firstly, the value of initial hardening modulus (C) varies while the nonlinear recovery parameter (γ) is constant for the monotonic case of loading.

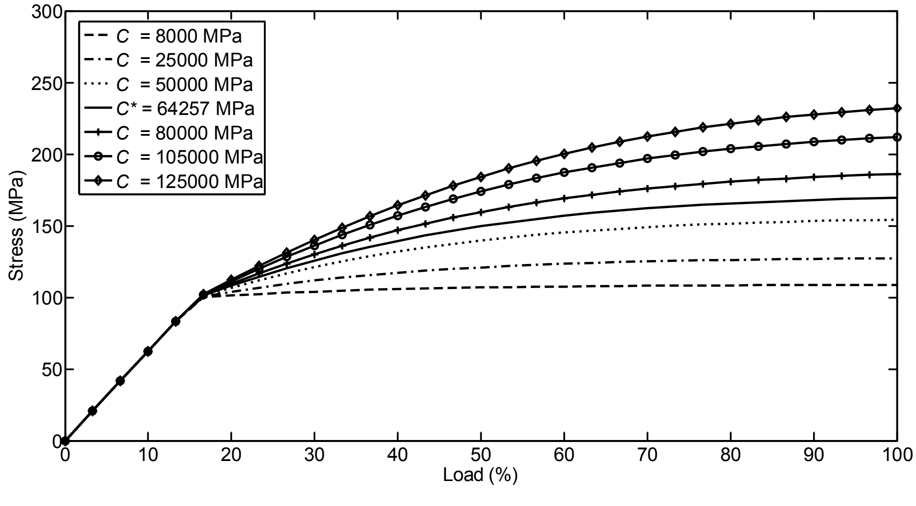

Figure 3.14: Sensitivity analysis regarding C for monotonic case of loading

As can be seen in Figure 3.14, the model hardens more with higher value of C and contrary. As a consequence, the plastic strain is reduced for the same stress level. Moreover, the maximum stress also depends on the value of C due to $\sigma_{\max} = \sigma_0 + C/\gamma$. In the next phase, the value of nonlinear recovery parameter (γ) changes while the value of initial hardening modulus (C) is constant. The nonlinear recall parameter defines a rate at which C starts to decrease with increasing the plastic strain. The initial hardening modulus decreases more significantly with the higher value of γ. The nonlinear kinematic hardening model becomes the linear kinematic hardening model developed by Prager for $\gamma = 0$.

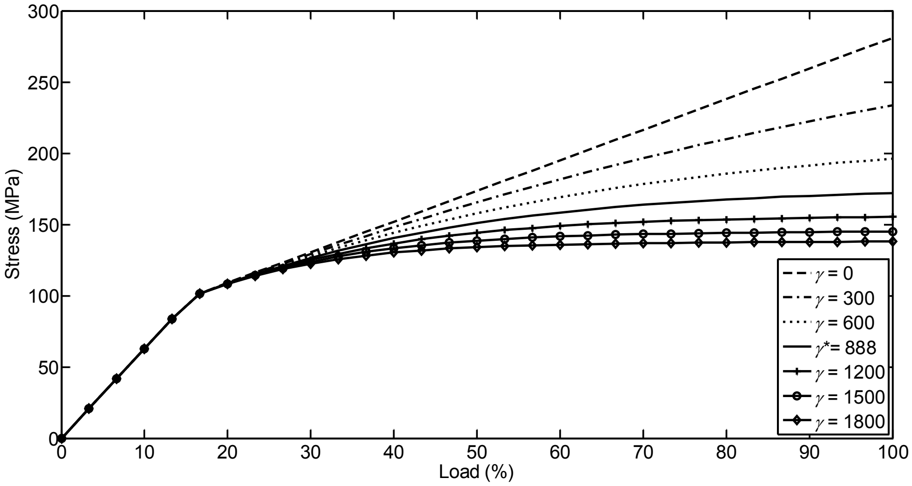

Figure 3.15: Sensitivity analysis regarding γ for monotonic case of loading

3.6.2 Nonlinear isotropic hardening material model

The following numerical simulation is performed considering the nonlinear isotropic hardening material model and adopting the numerical model described in Figure 3.10.

The isotropic material models have been already implemented in the Ansys® code as given options inside structural – nonlinear – inelastic – rate independent section. The Ansys® has the option to choose between three different material models (i.e. bilinear - BISO, multilinear – MISO and nonlinear model - NLISO). The nonlinear isotropic model (NLISO), adopted for the performed simulation, requires definition of the following parameters σ_0, R_∞ and b, which may be temperature dependent or independent. The material parameters used in the simulation are temperature independent and summarized in Table 3.1.

As can be seen in Figure 3.16, the model starts to elasto-plastically deform once the yield stress is achieved. In case of monotonic loading, the form of stress-strain curve is very similar to the one obtained with the elasto-perfectly plastic material model. The monotonic hardening phenomenon is negligible due to small amount of the accumulated plastic strain which occurs within monotonic loading and which affects on enlargement of the yield surface, equation 3.40. However, the nonlinear isotropic hardening model is able to simulate cyclic hardening or softening behaviour of materials, see Figure 3.17. Continuously symmetrical enlargement of the yield surface is observed from cycle to cycle until certain number of cycle when the model reaches the stabilization. Enlargement of the yield surface is simultaneously accompanied with increased value of the accumulated plastic strain from cycle to cycle. According to equation 3.41, the maximum stress when model reaches the stabilized condition is equal to:

$$\sigma_{\max} = \sigma_0 + R_\infty = 176 \text{ MPa} \quad 3.48$$

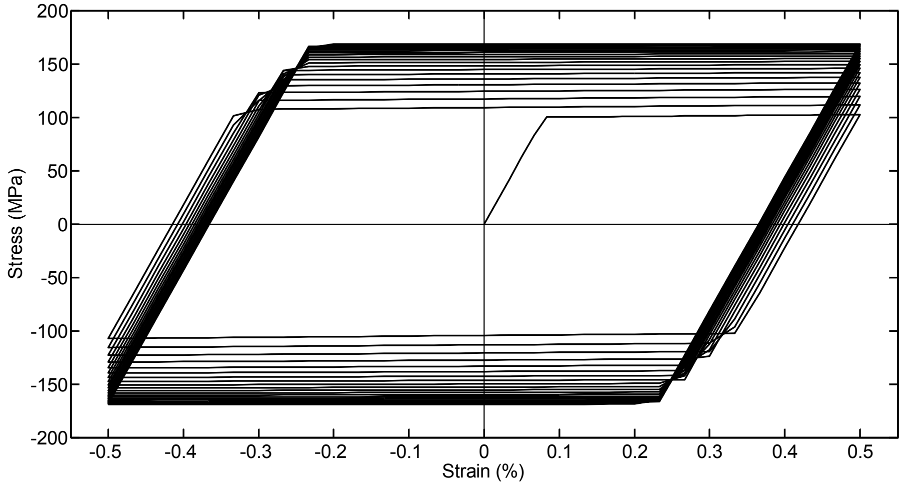

Figure 3.16: Nonlinear isotropic hardening model - stress-strain curves

The model needs approximately 15 cycles to reach stabilized condition for imposed material parameters and for ε_a=0.5%, see Figure 3.17.

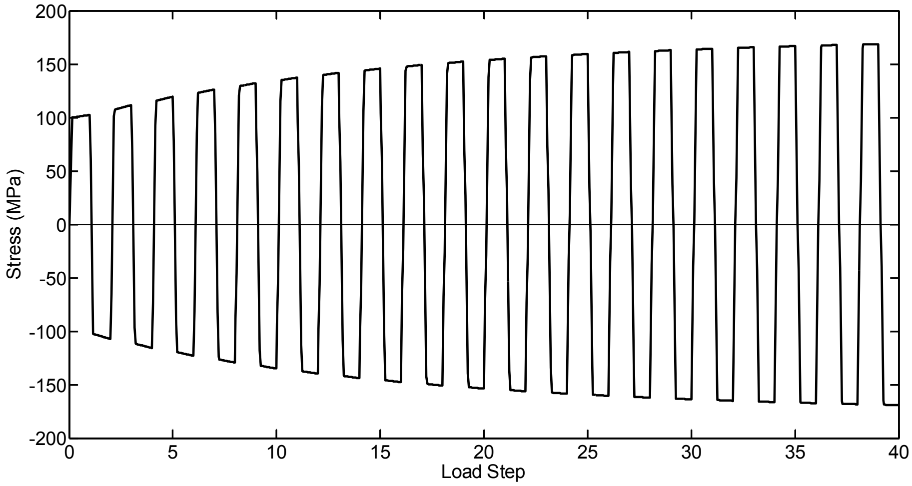

Figure 3.17: Nonlinear isotropic hardening model – Stress over load steps

Sensitivity analysis of nonlinear isotropic hardening material parameters – R_∞, b

Purpose of the sensitivity analysis is to understand better how the saturated stress (R_∞) and the speed of stabilization (b) define shape of stress-strain loops. Firstly, the saturated stress varies while the speed of stabilization is constant for the monotonic and cyclic case of loading.

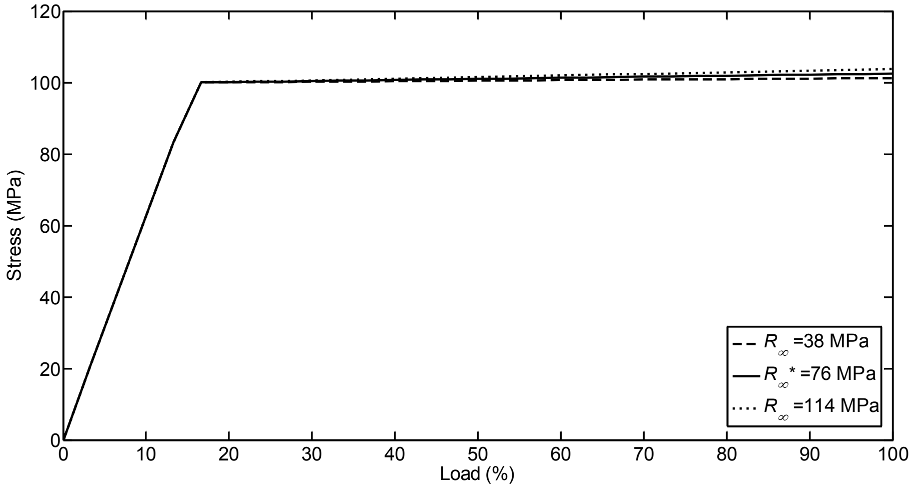

Figure 3.18: Sensitivity analysis regarding R_∞ for monotonic case of loading

The saturated stress defines the amount of cyclic hardening. For monotonic case of loading (Figure 3.18), difference between curves in the plastic region is very small due to small amount of the accumulated plastic strain which is governing parameter in equation 3.40. As can be seen in Figure 3.19, the accumulated plastic strain increases from cycle to cycle, in case of cyclic loading, simultaneously affecting on a major difference between curves. The cyclic hardening phenomenon is observed in all three cases due to positive values of R_∞ (38, 76 and 114 MPa).

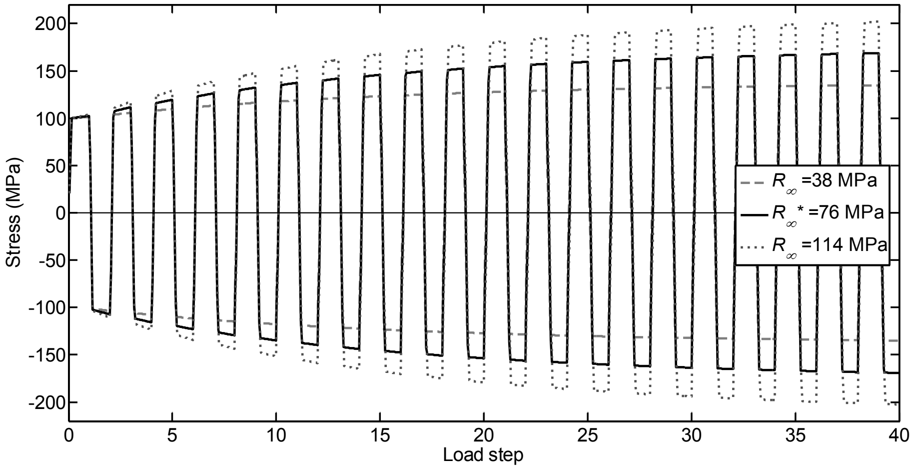

Figure 3.19: Sensitivity analysis regarding R_∞ for cyclic case of loading

In the next phase, the parameter R_∞ is constant while three different values (4, 8, 12) of *b* parameter are taken into consideration.

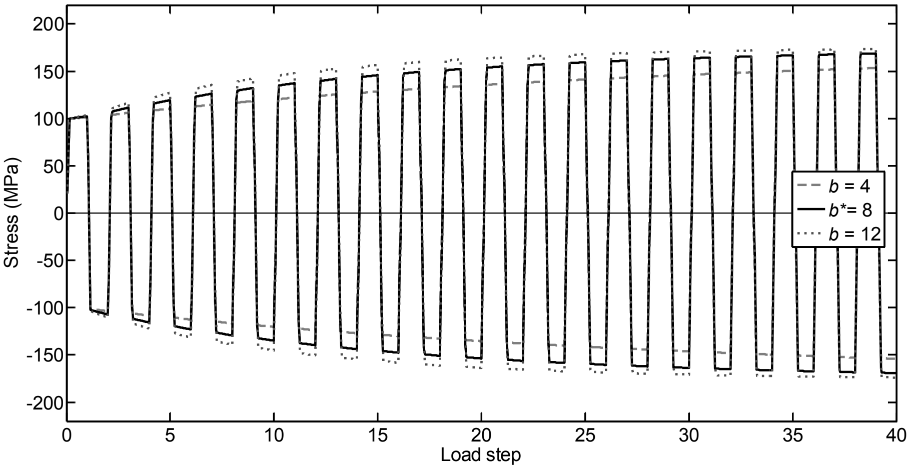

Figure 3.20: Sensitivity analysis considering *b* for cyclic case of loading

The model with the highest imposed value (*b*=12) reached the stabilized condition earlier with respect to other two model since *b* parameter defines the speed of stabilization and accordingly to equation 3.40, see Figure 3.20.

3.6.3 Combined material model - Armstrong and Frederick's model and nonlinear isotropic hardening model

As a final step, the numerical simulation is performed considering the combined material model (Armstrong and Frederick's model + nonlinear isotropic hardening model). The combined model is able to capture simultaneously monotonic hardening and cyclic hardening or softening phenomenon, according to the theory explained in the paragraph 3.5.3.

The combined material model is defined in the numerical simulation as a combination of Chaboche model (defining only the one pair of C, γ) and the nonlinear isotropic model. As in previous cases, all material parameters can be temperature dependent or independent. The material parameters used in analysis are summarized in Table 3.1. Moreover, temperature independence of material parameters is assumed.

As can be seen in Figure 3.21, changes in the yield surface occur after initial plastic strains, which in this case affect on translation and on expansion of the yield surface. The monotonic hardening is achieved with the Armstrong and Frederick's model which stabilizes in the first cycle. While, the cyclic hardening is captured with the nonlinear isotropic model which need approximately 15 cycles up to stabilization, see Figure 3.22.

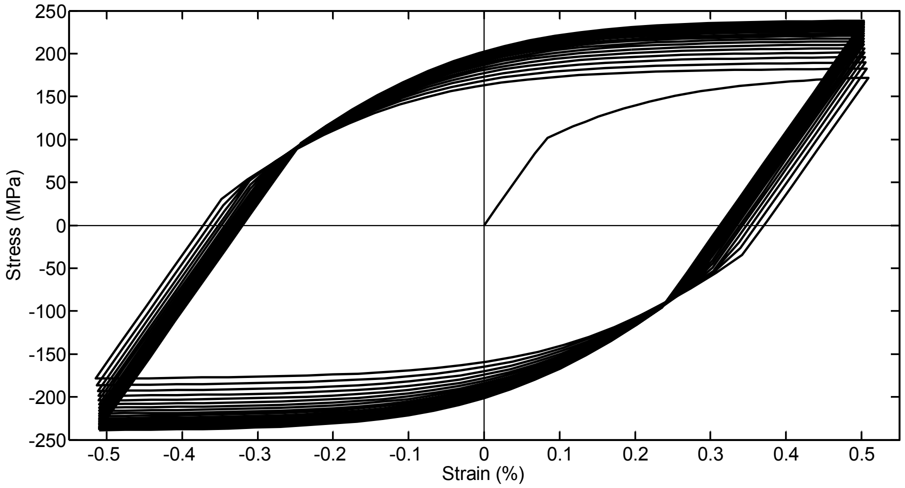

Figure 3.21: Combined material model – stress-strain curves

Size of the yield surface in case of the combined material model is equal to superposition of equation 3.47 and equation 3.48 which correspond to nonlinear kinematic and nonlinear isotropic model, respectively. When the model reaches stabilized condition, the maximum stress is equal to:

$$\sigma_{\max} = \sigma_0 + \frac{C}{\gamma} + R_{\infty} = 248 \text{ MPa} \tag{3.49}$$

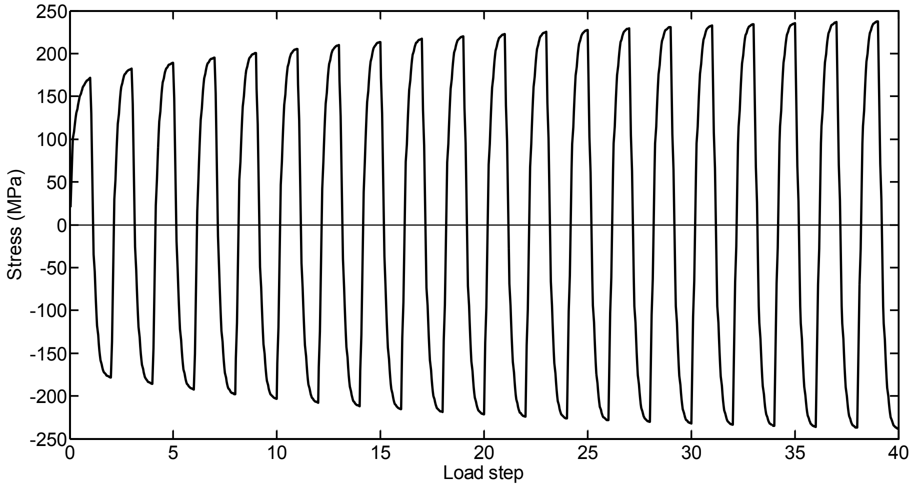

Figure 3.22: Combined material model – stress vs. load steps

Chapter 3 gives theoretical overview of three main concepts which can be found in the theory of plasticity: the yield criterion, the flow rule and the hardening models. With particular attention several material model (kinematic, isotropic and combined) have been theoretically presented and described. The numerical simulations and the sensitivity analyses have been performed to obtain clearer overview with respect to material models. The main goal of the second part is to find out influence of individual model on the material response. The identification procedure of material parameters can be performed once the theoretical part of the material models is known. Chapter 4 describes methodological approach to estimate the material parameter for the nonlinear kinematic and the nonlinear isotropic model, as well as the Young's modulus and the yield stress.

Chapter 4

Experimental testing and estimation of material parameters for CuAg alloy

---

Material models, presented in the previous Chapter, are defined with several parameters which is needed to calibrated from experimental data. Quite often, number of material parameters increases with increasing the model complexity. Complex numerical algorithms, various methods and optimisation routines are often used and recommended to identify multiple parameters simultaneously [Broggiato, 2008, Franulović, 2009, Franulović, 2014, Koo, 2011, Pajand, 2009, Tong, 2003, Zaletelj, 2011, Zhao, 2001]. Material characterisation has been missing at the beginning of this work. Therefore, preliminary material characterization considering isothermal LCF tests seemed to be reasonable to obtained preliminary results. All material parameters are estimated from isothermal LCF tests.

Chapter 4 is focused on methodology of material characterization. The first section describes the LCF (low cycle fatigue) tests that were performed on a CuAg alloy at three temperature levels. Moreover, briefly description of test machines as well as equipment used during the experimental testing is given.

The identification procedure of the yield stress and the Young's modulus from a first and a stabilized cycle is explained in the second part of this Chapter. Both parameters should be estimated precisely since they define the elastic region. Having determined the yield stress and the Young's modulus, estimation of the material parameters can be performed for the nonlinear kinematic and the nonlinear isotropic model. Once all parameters are determined, comparisons between experimental and simulated stress-strain loops are done in order to evaluate goodness of estimated parameters with respect to used approaches. Obtained results show satisfactory agreement as could be seen at the end of this Chapter.

4.1 Experimental testing

Isothermal low cycle fatigue (LCF) tests were performed to characterize the cyclic stress-strain behaviour and fatigue life of CuAg alloy at three temperature levels (20 ^{o}C, 250 ^{o}C and 300 ^{o}C). Experimental testing was performed in the Fatigue Analysis Laboratory at Montanuniversity in Leoben, where several specimens were tested at different strain ranges at each temperature level. All isothermal LCF tests were carried out in strain controlled mode with a triangular loading waveform and with a fully reversed strain ratio:

$$R_{\varepsilon} = \frac{\varepsilon_{\min}}{\varepsilon_{\max}} = -1 \qquad 4.1$$

The examined strain rate was $0.01 s^{-1}$. Generally, the range of loading frequency for LCF tests is between 0.1 and 1 Hz. The sampling frequency of data shall be at least 200 data points per loop to ensure adequate definition of stress-strain loop, especially in the region of strain reversal. Tests were interrupted before specimen failure when the maximal stress decreased by 80%.

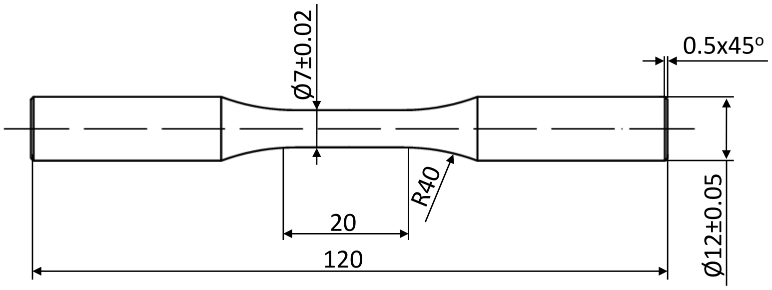

Figure 4.1: Shape and dimension of a specimen

Low cycle fatigue tests at 20 ^{o}C were performed on the servo-hydraulic Instron-Schenck test rig with a nominal force ±250 kN (Figure 4.2), while the Instron extensometer with a gauge length of 12.5 mm and a range of ±5 mm was used to measure elongation during testing, as can be seen in Figure 4.3. Specimens were clamped by mechanical clamping grips.

Figure 4.2: Servo-hydraulic Schenck 250 kN test rig

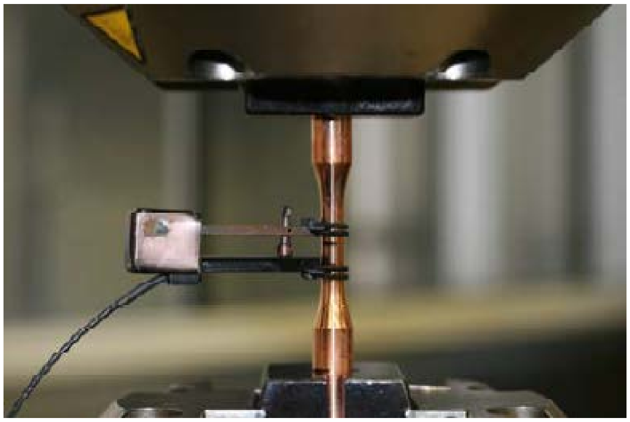

Figure 4.3: Mechanical clamping jaws with extensometer for room temperature

Isothermal LCF testing at 250 °C and 300 °C were performed on the Instron test rig with a nominal force of ±100 kN. The temperature was applied by the induction heating system with a 10 kW medium frequency generator, Hüttinger TIG 10/300. The temperature was measured within the gauge length with a pre-stressed type K loop thermocouple. To measure an elongation at high temperatures the MTS extensometer, model 632.53F-14 with a gauge length of 12.6 mm and a range of ±1.8 mm was used. Test specimens were clamped by water cooled hydraulic clamping grips. Hydraulic grips are water cooled in order to allow quick cyclic stabilization of the longitudinal temperature distribution within the gauge length and to provide stable thermal condition during the experimental testing. According to ISO 12111 from 2011 year, a temperature of tested specimens near hydraulic grips should be within 15 °C up to 40 °C, depending on a tested temperature. During the performed experimental testing, most of specimens failed in the middle part where the maximum tested temperatures had appeared.

Figure 4.4: Servo-hydraulic Instron 100 kN test rig

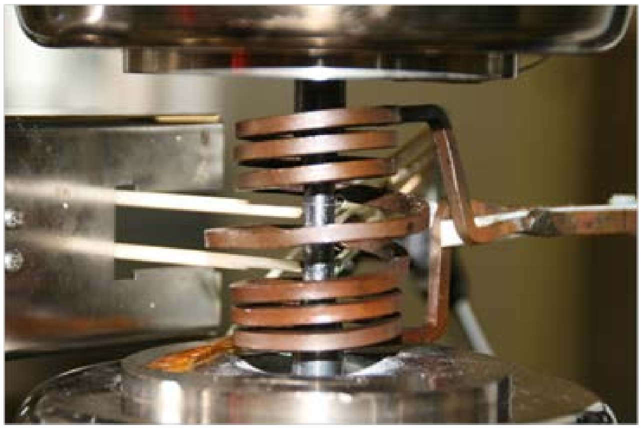

Figure 4.5: Hydraulic clamping jaws, HT extensometer and heating apparatus

4.2 Identification of material parameters

Firstly, identification of the yield stress and the Young's modulus is needed to perform from LCF experimental data of CuAg alloy at three temperature levels (20 ^{o}C, 250 ^{o}C and 300 ^{o}C). Accurate estimation of Young's modulus and the yield stress is essential for precise representation of a material response; since they define the elastic strain range. Afterwards, estimation procedures of the material parameters for the nonlinear kinematic and the nonlinear isotropic models can be performed.

4.2.1 Identification of the initial and actual yield stress

Materials, such as aluminium and copper (FCC metals), show a gradual transition from the elastic to the plastic region. Therefore, there is not an exact stress point at which plastic deformation begins to occur. Various criteria for determining the initial yield stress from the tensile test have been proposed in literature [ASM, 2000; ASTM]. An exact amount of total, elastic and plastic strain is unknown in case of a tensile test data. While, this is not valid in case of having LCF data where at each point of loading an amount of total, elastic and plastic strain is known. Figure 4.6 is obtained by plotting the stress versus the plastic strain considering a tensile portion of the first hysteresis loop. As can be seen in Figure 4.6, the initial yield stress (σ_0) is identified as the point on tensile portion of the first hysteresis loop where the plastic strain starts to occur. The ''negative'' plastic strain is recorded in a region beyond the initial yield stress. Theoretically, the initial portion of the stress-strain curve should to be a vertical straight line due to ε_{pl}=0. However, an initial curve is observed sometimes as either concave or convex. This is probably influenced by some problems which can occur in a test set-up (specimen is not correctly fixed; testing speed is not well controlled or straightening of an initially bent specimen) [ASM, 2000].

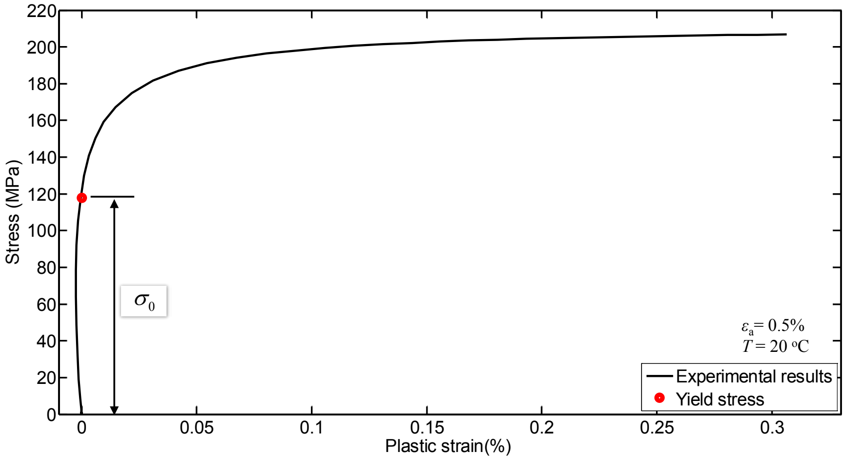

Figure 4.6: Identification of σ_0 from tensile portion of the first hysteresis loop

The actual yield stress (σ_{0*}) is identified considering the stabilized loop and using the offset method proposed in [ASM, 2000; ASTM]. However, the offset method has been a little bit modified, since the original method is proposed for a tensile test data, see Figure 4.7. The offset method is applied in this case to the stabilized stress-plastic strain loop, see Figure 4.8.

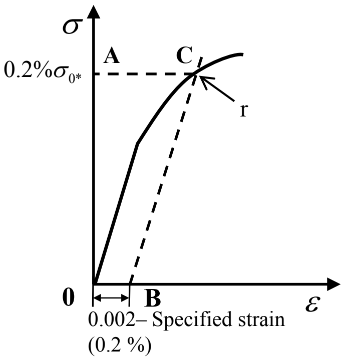

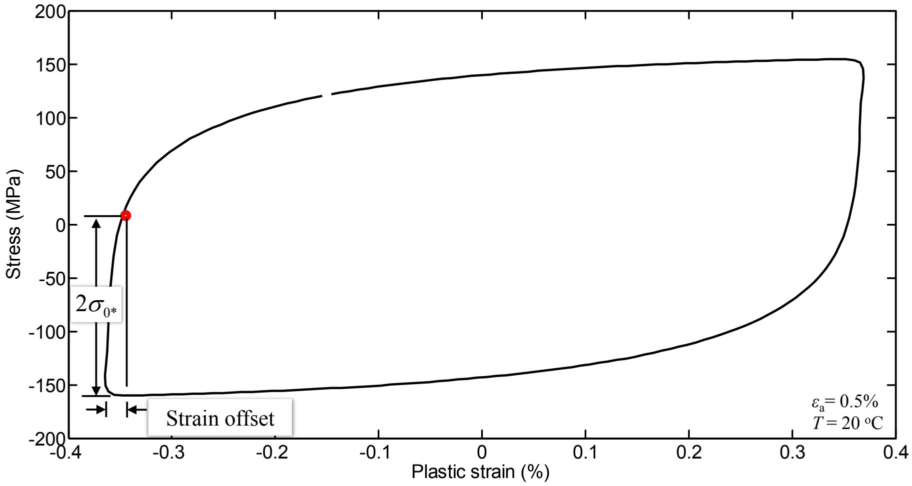

Figure 4.7: Offset Method

Figure 4.8: Identification of σ_{0*} from the stabilized hysteresis loop

As can be seen in Figure 4.8, plotting the stress versus the plastic strain for a stabilized cycle, there is not an exact stress point at which plastic deformation begins to occur. Therefore, the plastic strain offset (for instance ε_{pl}=0.02%) is necessary to define and imposed it at the tip of the loop. The intersection of the stress-plastic strain curve with the vertical straight line (shifted for ε_{pl}=0.02% from tip of the loop) finally gives the $2\sigma_{0*}$ (red dot in Figure 4.8). Concluding, the actual yield stress is identified from the stabilized loop by plotting the stress versus the plastic strain (Figure 4.8) and using the modified offset method. The evolution of the yield stress with increasing number of cycles enables to determine the hardening or the softening characteristics of materials [Hales, 2002]. All estimated values of the initial and the actual yield stress are listed in Table 4.1-Table 4.3 with respect to testing temperature.

Table 4.1: Estimated values of the initial yield stress and the actual yield stress for T = 20 °C

Yield stress	Strain amplitude (%)										Average value
	0.15	0.175	0.2	0.3	0.4	0.5	0.6	0.7	1	1.25	
σ_0 (MPa)	51.3	90.3	95.7	121.6	138.7	118	135.4	155	221.1	174.7	130
σ_{0*} (MPa)		60.5	71.6	87.9	91.4	84.3	88.9	114			86

Table 4.2: Estimated values of the initial yield stress and the actual yield stress for $T = 250\ ^{o}\mathrm{C}$

Yield stress	Strain amplitude (%)						Average value
	0.2	0.3	0.35	0.4	0.5	0.7	
σ_0 (MPa)		121	111.3	103.4	140.3	80.7	111
σ_{0*} (MPa)	43.1		51.7	50.9	51	53	50

Table 4.3: Estimated values of the initial yield stress and the actual yield stress for $T = 300^{o}\mathrm{C}$

Yield stress	Strain amplitude (%)							Average value
	0.175	0.2	0.25	0.3	0.4	0.5	0.7	
σ_0 (MPa)				124	103.3	116.4	122.5	110
σ_{0*} (MPa)	48.3	40.6	48.5	44.7	48.2	40.5	43.5	45

It can be noticed that in all cases $\sigma_{0*} < \sigma_0$, confirming softening behaviour of the CuAg alloy at all three temperature levels (20 ^{o}C, 250 ^{o}C and 300 ^{o}C) and for all strain amplitudes. In addition, the initial yield stress is temperature dependent parameter, i.e. decreases with increasing the temperature $\sigma_{0,300} < \sigma_{0,250} < \sigma_{0,20}$ as well as the actual yield stress $\sigma_{0*,300} < \sigma_{0*,250} < \sigma_{0*,20}$. The initial yield stress and actual yield stress cannot be estimated for some strain amplitudes due to noise which appeared during the experimental testing.

4.2.2 Identification of the Young's modulus

The Young's modulus, as well as the yield stress, is estimated using both the tensile portion of the first hysteresis loop (E_1) and the stabilized stress-strain loop (E_s). The Young's modulus may vary during testing [Hales, 2002]. Estimation is performed using the linear least square method implemented in Curve Fitting Toolbox-MATLAB technical computing environment, see Figure 4.9 right. The E_1 is determined using the region beyond the initial yield stress as can be seen in Figure 4.9.

Here the statistical measure R^2 is used to judge the adequacy of a regression model. Definition of R^2 is given in Chapter 6.

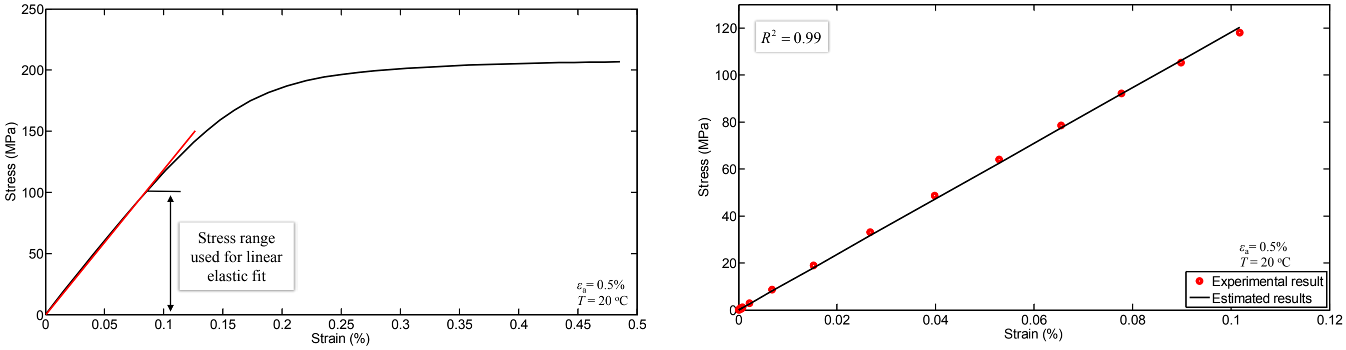

Figure 4.9: Identification of E_1 from the first quarter of hysteresis loop

Identification of the Young's modulus (E_s) from the stabilized loop is done using the method proposed by [Hales, 2002] which suggests fitting of the linear least square method over the defined stress range. The proposed method is simply to implement, however, the estimated value of E_s is very sensitive to the defined stress range and to the imposed strain offset. The stress range, used during the estimation process, is defined with two limits: the upper limit is equal to $2\sigma_{0*}$ (because the actual yield stress defines the elastic strain range), while for the lower limit is taken the stress which corresponds to strain offset (ε=0.01%) imposed at the tip of the loop. Figure 4.10 schematically describes estimation procedure of the Young's modulus (E_s) from the stabilized loop. Sufficient numbers of stress-strain points is needed to be recorded within the elastic region in order to estimate Young's modulus accurately.

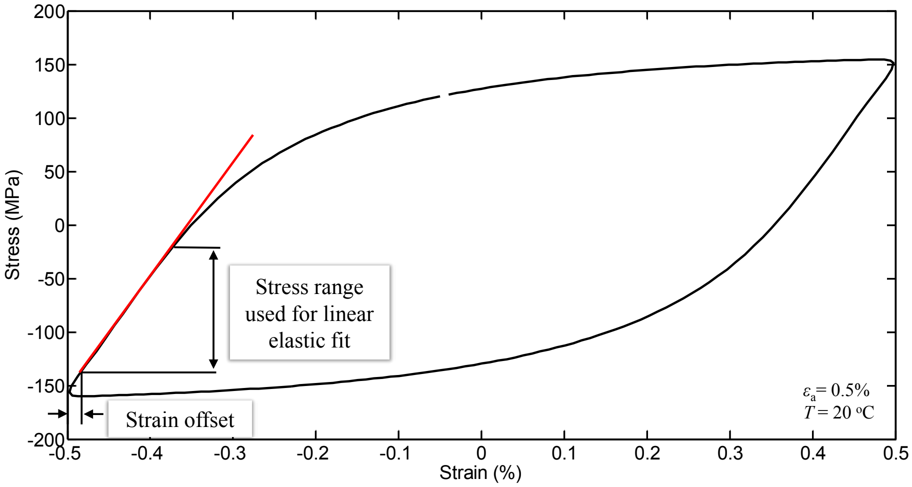

Figure 4.10: Identification procedure of E_s from the stabilized hysteresis loop

Estimated values of E_1 and E_s considering several strain amplitudes and three temperature levels are summarized in Table 4.4 -Table 4.6, respectively. Both Young's modulus are the function of temperature $E_{1,300} < E_{1,250} < E_{1,20}$ and $E_{s,300} \leq E_{s,250} < E_{s,20}$. In addition, they seem to depend on the applied strain amplitude (ε_a). Furthermore, the Young's modulus is slightly decreasing with increasing number of cycles,

$E_{s,20} < E_{1,20}$, $E_{s,250} < E_{1,250}$ and $E_{s,300} < E_{1,300}$. For some strain amplitudes, the Young's modulus cannot be estimated due to due to noise which has been recorded during the testing.

Table 4.4: Estimated Young's modulus for $T = 20\ ^{o}C$

Young's modulus	Strain amplitude (%)										Average value
	0.15	0.175	0.2	0.3	0.4	0.5	0.6	0.7	1	1.25	
E_1 (GPa)	122.4	122	121.5	119.7	119.9	118.2	117.4	118.8	114.7	116.2	119.08
E_s (GPa)		114.5	115.9	116.9	115.9	113.5	110.1	114.9			110.9

Table 4.5: Estimated Young's modulus for $T = 250\ ^{o}C$

Young's modulus	Strain amplitude (%)						Average value
	0.2	0.3	0.35	0.4	0.5	0.7	
E_1 (GPa)		108.5	108.6	93.6	105.4	103.9	104
E_s (GPa)	99.9		98.5	98.8	90.1	85.1.	94.7

Table 4.6: Estimated Young's modulus for $T = 300\ ^{o}C$

Young's modulus	Strain amplitude (%)							Average value
	0.175	0.2	0.25	0.3	0.4	0.5	0.7	
E_1 (GPa)				105.6	104.3	101.9	103.4	103.8
E_s (GPa)	94	96.9	92.3	97.9	98.8	95.8	103.4	94.8

Calibration of the nonlinear kinematic material parameters (C_i, γ_i) can be performed once the yield stress and the Young's modulus have been estimated.

4.2.3 *Identification of material parameters for nonlinear kinematic hardening model*

Estimation procedure of the nonlinear kinematic and the nonlinear isotropic parameters could be performed separately. As for fully-reversed symmetrical stress cycles the kinematic model stabilized after a single cycle, while a contribution of the isotropic model is actually small and could be neglected in the first cycle [Lemaitre, 1990]. The contribution of the isotropic model can be neglected because the amount of the accumulated plastic strain (expressed with equation 3.39), which mainly controls the evolution of the isotropic model, is negligible small in the first cycle and increases with number of cycles. Moreover, the kinematic model is the one which defines the shape of the hysteresis loop. Obviously, way by which the material parameters are determined depends significantly on availability of experimental data. Three different identification methods are adopted and presented in addition:

1) using a single tension curve,
2) using a single stabilized stress-strain hysteresis loop and
3) using several stabilized stress-strain hysteresis loops.

4.2.3.1 Identification from single tension curve

Approximate parameters of C_i and γ_i can be estimated using a single tension curve, see Figure 4.11. However, this approach is not recommended since there are no cyclic data with which to correlate the parameters [Imaoka, 2008]. Having only a tensile test data, an amount of the total strain is known, while an amount of the elastic and plastic strain is unknown. The identification procedure of C_i and γ_i should be performed based on the stress versus the plastic strain data, but this cannot be done since an amount of the plastic strain is unknown. However, subtracting the initial yield stress from the overall stress (red dot on the Figure 4.11) gives the stress-strain distribution (red line on the Figure 4.11) which should be converted to the back stress by shifting the obtained stress-strain to the origin of the coordinate system.

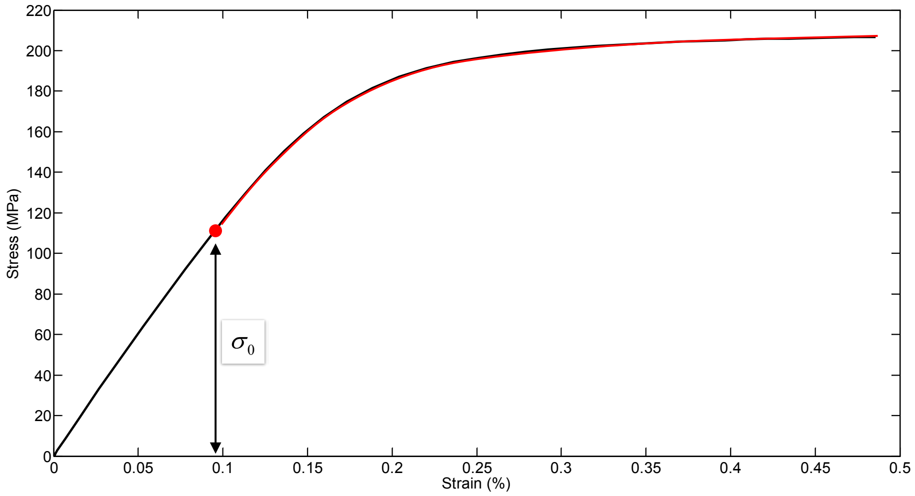

Figure 4.11: Identification of C_i and γ_i from a single tension curve

Material parameters are possible to identify with respect to obtained stress-strain data and using equation (3.25). This approach may be suitable for situations when is needed to simulate only a few cycles [Imaoka, 2008], however, in any case obtained results should be taken with additional reserve of caution.

4.2.3.2 Identification from a single stabilized cycle

Identification of material parameters (C_i, γ_i) can be performed using a single stabilized stress-strain hysteresis loop. Estimated parameters are appropriate to use for particular strain amplitude that has been used during the identification procedure. Firstly, the elastic and the plastic part are necessary to identify using the stabilized stress-strain loop as a starting point. The actual yield stress that defines the elastic region for stabilized cycle is used to separate the elastic and the plastic part. Additionally, the plastic strain range and the stress range are needed to measure. The plastic part (the back stress) is obtained by subtracting the actual yield stress from the upper branch (i.e. $\alpha=\Delta\sigma/2 - \sigma_{0*}$). Moreover, the plastic part should be shifted to the origin of the coordinate system. Shifting is done due to facilitate implementation of the nonlinear least square method. Calculation steps described until now are presented in Figure 4.12.

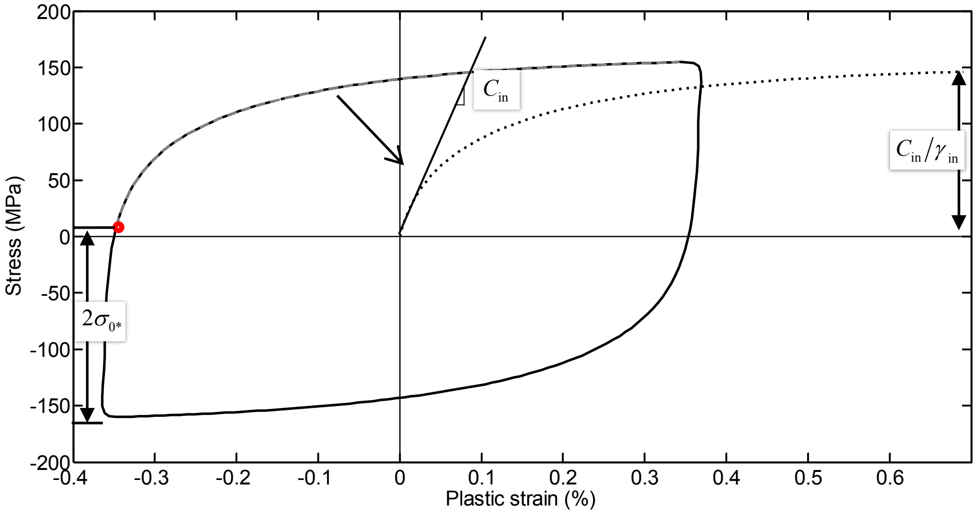

Figure 4.12: Stress vs. plastic strain for a single stabilized cycle

Equation (3.25) is appropriate to use in order to identify parameters (C_i, γ_i) from a single stabilized cycle. Elaboration of the data is performed with the Curve Fitting Toolbox. The Curve Fitting Toolbox has possibility of writing custom equation that becomes base for the nonlinear least square method. Moreover, the Toolbox has option to define the initial starting points as well as the upper and the lower bounds. The initial values of C_{in} and γ_{in} are imposed as the initial starting points. The slope after the yield stress is assumed to be C_{in} while γ_{in} is obtained through the relation $C_{\text{in}}/\gamma_{\text{in}}$, see Figure 4.12.

Figure 4.13 shows fitting between the experimental data and superposition of three determined back stresses. The first pair (C_1, γ_1 - dashed line) achieves stabilization very fast due to very high γ_1. The initial hardening modulus (C_1) decreases more with higher value of γ_1, since the nonlinear recall parameter (γ) defines a rate at which C starts to decrease with increasing the plastic strain. The second pair (C_2, γ_2 – dash dot line) has smaller γ_2 and archives the maximum stress (i.e. stabilization) after the first pair. The third pair (C_3, γ_3 – dotted line) has the highest maximum stress ($\sigma_{\max}=C_3/\gamma_3$) that has been reached after the second and the third pair due to $\gamma_1 > \gamma_2 > \gamma_3$. The second pair has the greater slope and stabilizes earlier than the third pair. The material parameters used during the estimation procedure are summarized in the Table 4.7. Sum of all three back stresses gives the final curve (solid line) which shows goodness of fitting regarding experimental data.

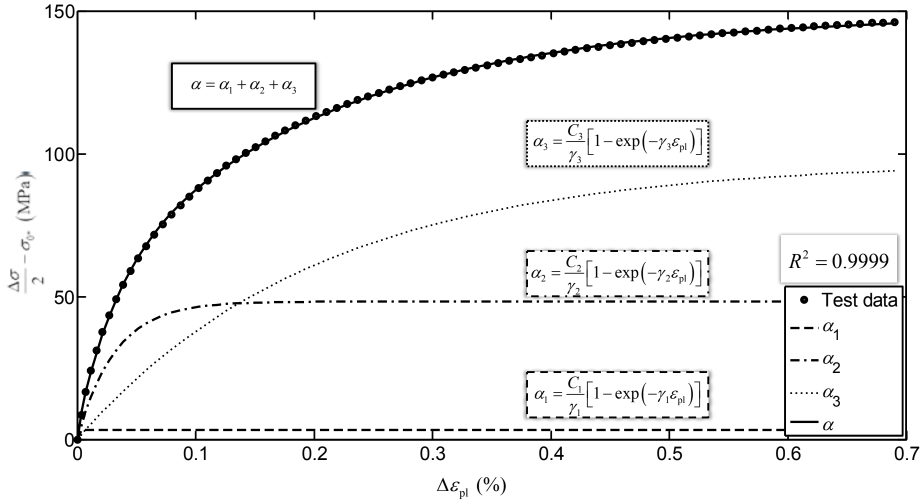

Figure 4.13: Superposition of three nonlinear kinematic hardening models – $T = 20$ °C

Superposition of two nonlinear kinematic hardening models gives the good agreement regarding the experimental, as can be seen in Figure 4.14. The first pair has a greater slope and stabilizes faster than the second pair because $C_1 > C_2$ and $\gamma_1 > \gamma_2$, see Table 4.7. The statistical measure, R^2=0.9998, shows precisely fitting between the experimental data and the calculated back stress.

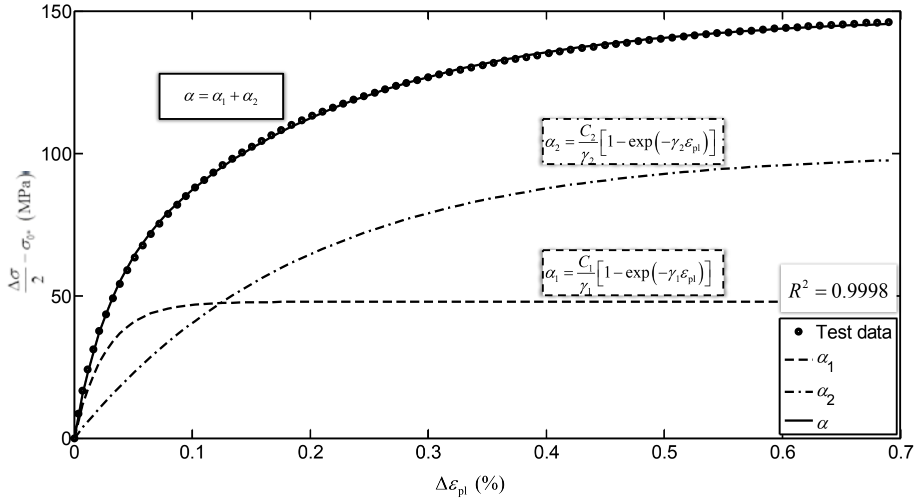

Figure 4.14: Superposition of two nonlinear kinematic hardening models – $T = 20$ °C

Figure 4.15 shows the correlation between the experimental data and the back stress obtained with just one pair of material parameters. In this case, the fitting is not so precisely, R^2=0.9787, as in the previous two cases with two and three pairs of material parameters.

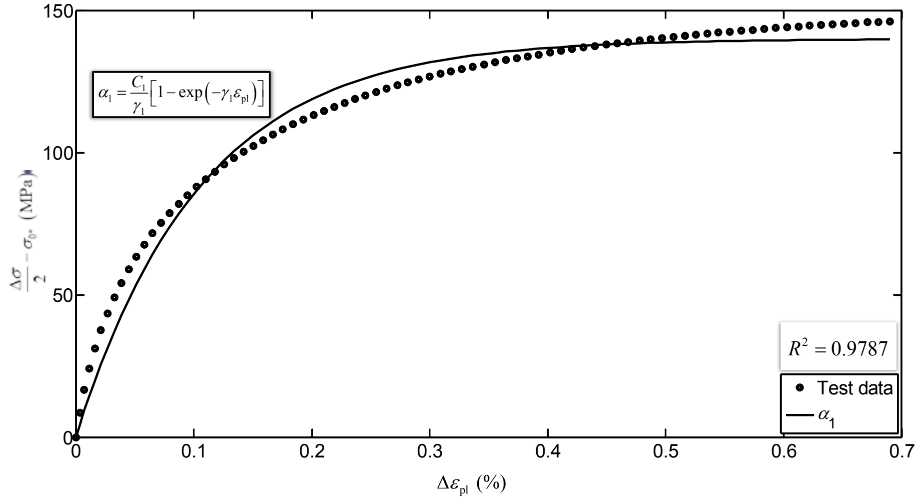

Figure 4.15: Nonlinear kinematic hardening model with one pair of material parameters – $T = 20$ °C

Parameters determined with the second method and considering the experimental data ε_a=0.5% at 20 °C are summarized in Table 4.7.

Table 4.7: Nonlinear kinematic hardening parameters (C_i, γ_i) - $T = 20$ °C

	Stain amplitude – 0.5%					
	C_1 (MPa)	γ_1	C_2 (MPa)	γ_2	C_3 (MPa)	γ_3
Three pairs	1089000	661700	76370	3163	23970	492.8
Two pairs	90420	3779	25830	514.2		
One pair	66000	943				

In addition, the material parameters (C_i, γ_i) are estimated using the second already explained identification method and considering the LCF data with ε_a=0.5% at 250 °C.

Figure 4.16 -Figure 4.18 show correlation between the LCF data and the back stresses obtained with 3, 2 and 1 pair of material parameters, respectively. Figure 4.16 present fitting between the experimental data and the superposition of three nonlinear kinematic models. The first pair has the highest slope and achieves the stabilization faster than two other curves due to $C_1 > C_2 > C_3$ and $\gamma_1 > \gamma_2 > \gamma_3$, see Table 4.8.

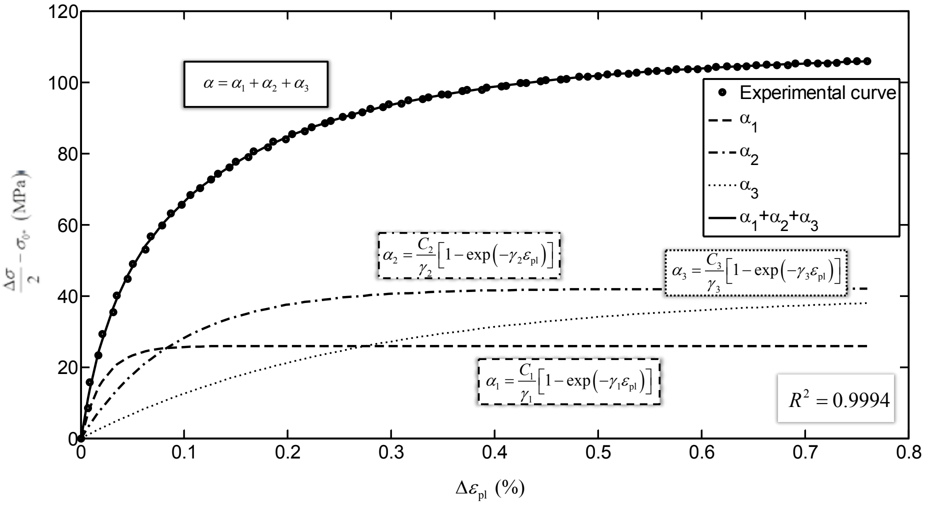

Figure 4.16: Superposition of three nonlinear kinematic hardening models – T=250 °C

The good agreement is also achieved with the superposition of two nonlinear kinematic hardening models. As can be seen in Table 4.8, the curve calculated with first pair has a greater slope and stabilizes faster than the second pair due to $C_1 > C_2$ and $\gamma_1 > \gamma_2$.

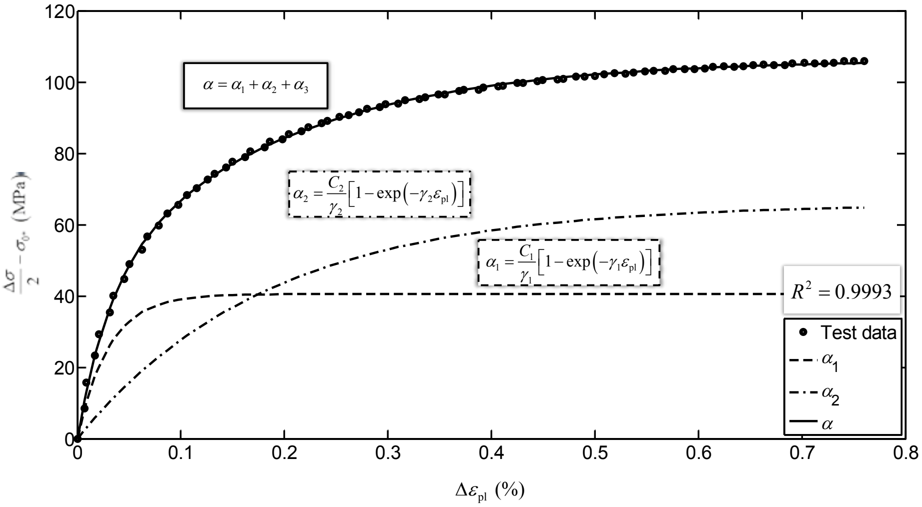

Figure 4.17: Superposition of two nonlinear kinematic hardening models – T = 250 °C

Fitting between the experimental data and the back stress obtained with only one pair gives satisfactory agreement. The R^2 is the lowest regarding two previous cases. The best correlation between experimental and calculated back stress is obtained with 3 pairs as in case of LCF experimental data at 20 °C.

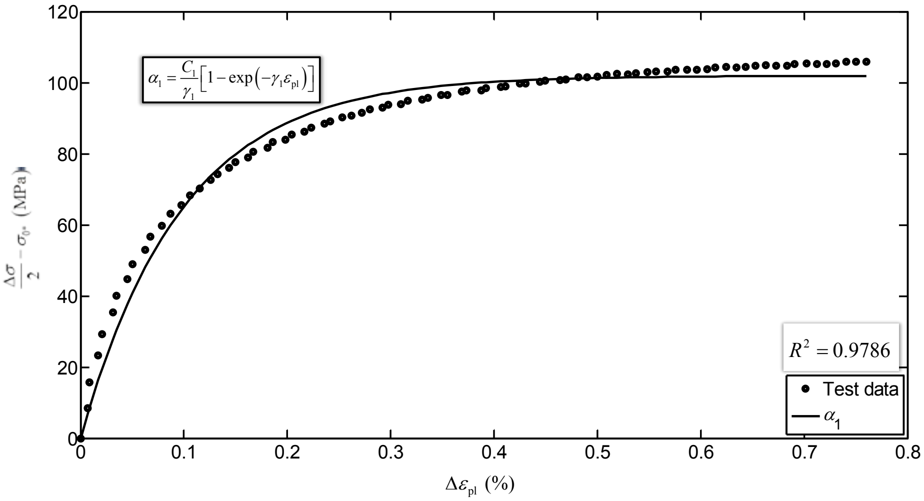

Figure 4.18: Nonlinear kinematic hardening model with one pair of material parameters – $T = 250$ °C

Table 4.8 summarized the material parameters identified from the LCF data with respect to ε_a=0.5% at 250°C.

Table 4.8: Nonlinear kinematic hardening parameters (C_i, γ_i) - $T = 250$ °C

	Stain amplitude – 0.5%					
	C_1 (MPa)	γ_1	C_2 (MPa)	γ_2	C_3 (MPa)	γ_3
Three pairs	59780	4647	23480	1132	7758	379.4
Two pairs	67230	3315	17970	554.9		
One pair	52000	1020				

In addition, material parameters are estimated from LCF data with ε_a=0.5% at 300 °C by applying the identification procedure explained in case $T = 20$ °C

Figure 4.19 -Figure 4.21 present fitting between the experimental and estimated back stresses with 3, 2 and 1 pair of material parameters, respectively. Also in this case, the best correlation is obtained with 3 pairs, while with only 1 pair of parameters is obtained not so precise fitting between experimental and calculated back stress.

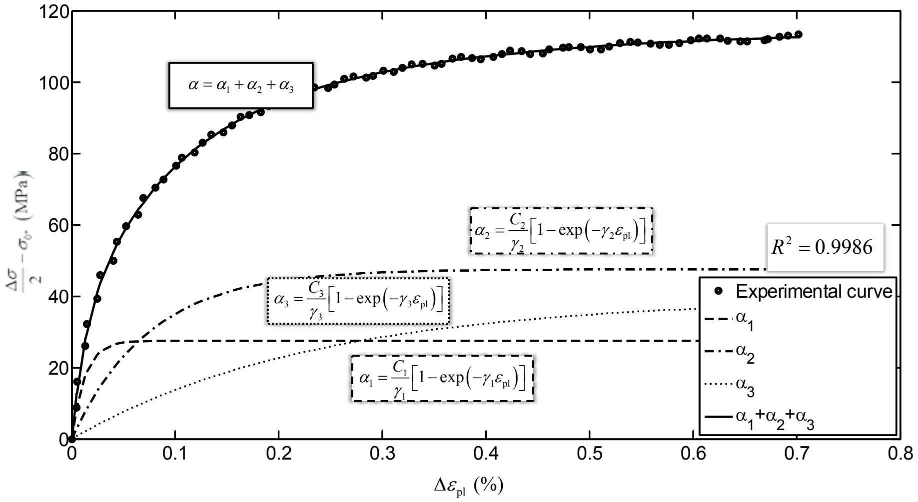

Figure 4.19: Superposition of three nonlinear kinematic hardening models – *T*=300 ^{o}C

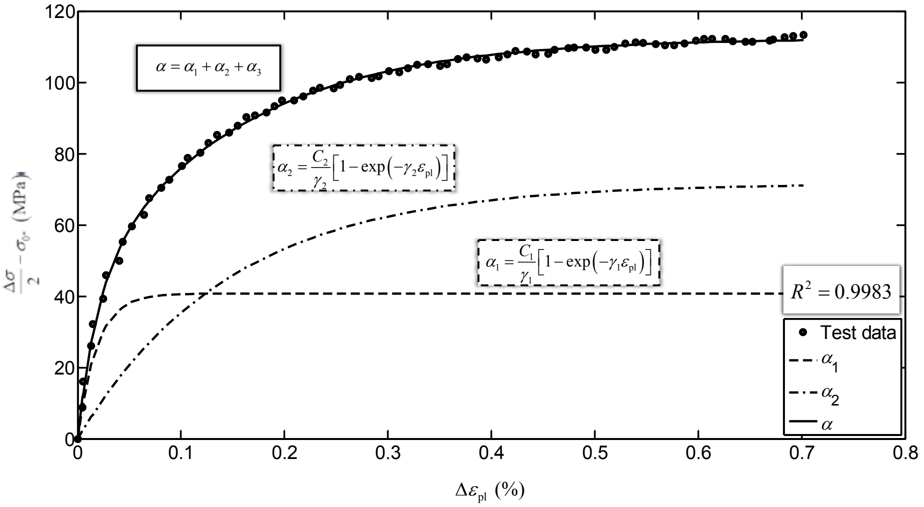

Figure 4.20: Superposition of two nonlinear kinematic hardening models – *T* = 300 ^{o}C

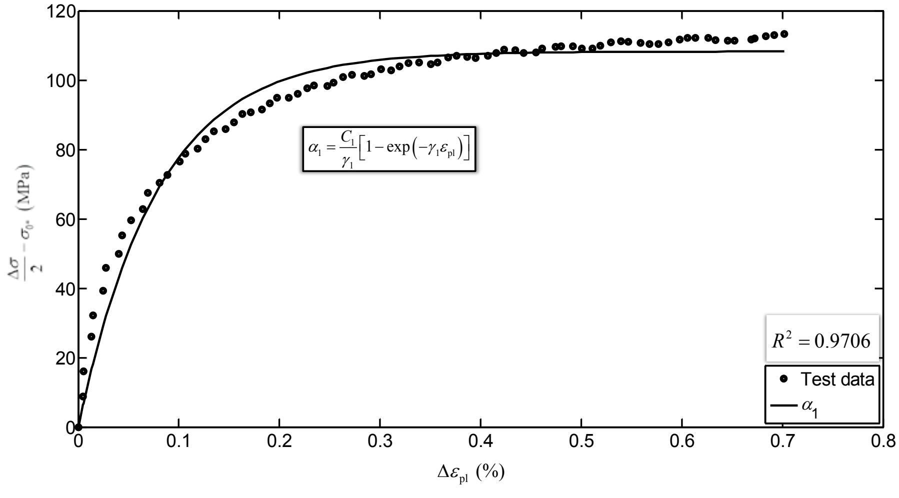

Figure 4.21: Nonlinear kinematic hardening model with one pair of material parameters – *T* = 300 ^{o}C

Material parameters determined from LCF data with ε_a=0.5% measured at 300 °C are summarized in Table 4.9

Table 4.9: Nonlinear kinematic hardening parameters (C_i, γ_i) - T = 300 °C

	Stain amplitude – 0.5%					
	C_1 (MPa)	γ_1	C_2 (MPa)	γ_2	C_3 (MPa)	γ_3
Three pairs	108800	7906	31760	1337	8437	427.3
Two pairs	110000	5396	24390	681		
One pair	68420	1264				

Comparison between experimental stabilized stress-strain loops and simulated loops is performed to assess quality of estimated material parameters. Numerical simulations are performed adopting the example described in paragraph 3.6. Values of the Young's modulus (E_s) and the actual yield stress (σ_{0*}) used in simulation correspond to values estimated from LCF data with ε_a=0.5% at 20 °C.

Figure 4.22 shows comparison between the experimental and simulated stress-strain loops with 1, 2 and 3 pairs of parameters with respect to data at 20 °C, see Table 4.7. A better agreement, in the middle part of stress-strain loop, is obtained using two and three pairs of material parameters while results obtained with just one pair do not show such good agreement. Furthermore, simulated stress-strain loops obtained with two and three pairs overlap each other. All three simulated hysteresis approximately coincide (±1 MPa) to experimental loop in case that peaks of loops are observed.

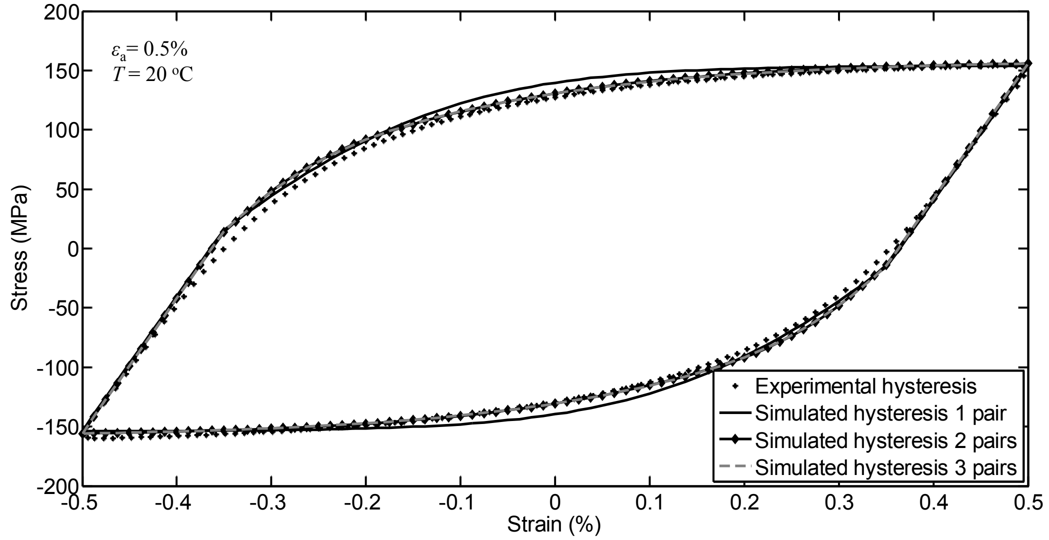

Figure 4.22: Comparison between experimental and simulated stress-strain loops – T = 20 °C

In addition, Figure 4.23 shows fitting between the experimental and simulated stress-strain loops with 1, 2 and 3 pairs of parameters with respect to data at 250 °C, see Table 4.8. The better fitting, considering the middle part of the loop, is obtained with loops that correspond to 2 and 3 pairs of parameters. However, all three simulated loops coincide to experimental loop ±1 MPa in the peaks.

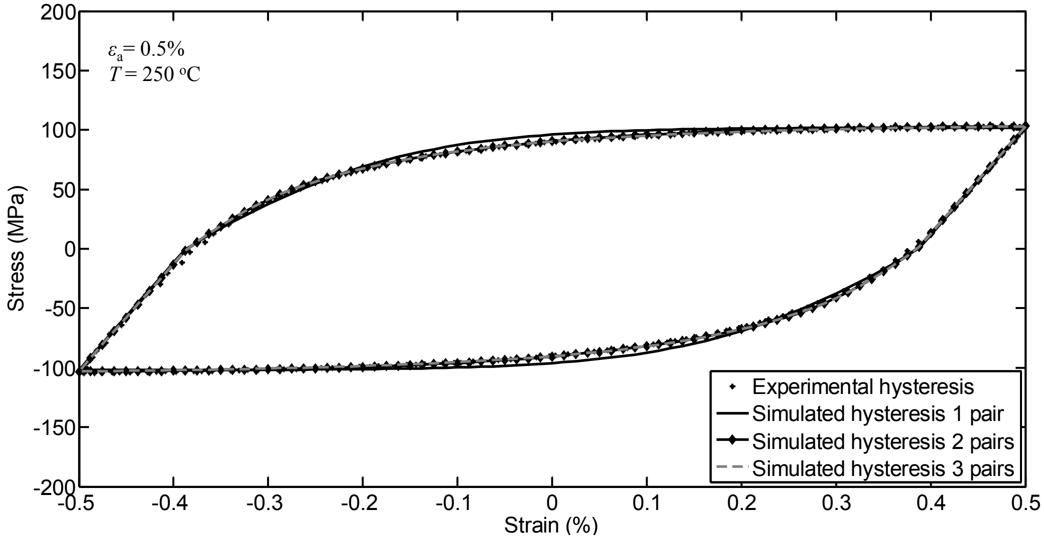

Figure 4.23: Comparison between experimental and simulated hysteresis – T = 250 °C

The last comparison takes into consideration the experimental data and material parameter with respect to T=300 °C, see Table 4.9. Fitting between the experimental stabilized loop and simulated stress-strain loops obtained with 2 and 3 pair, considering the middle part, is better than with the loop gained with one pair. Also in this case, all three simulated loops coincide to experimental loop ±1 MPa in peaks.

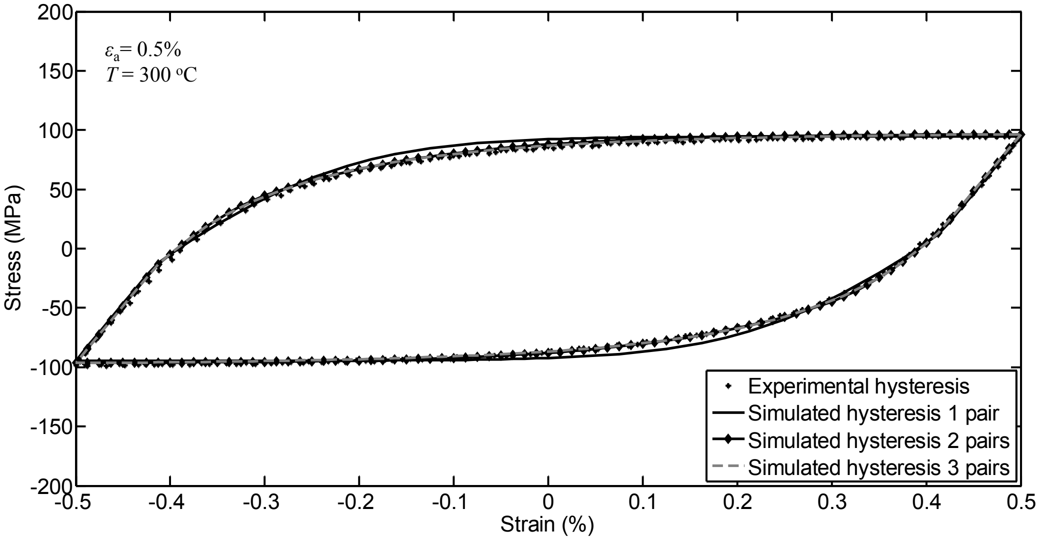

Figure 4.24: Comparison between experimental and simulated hysteresis – T = 300 °C

4.2.3.3 Identification from several stabilized cycles

The method proposed by [Lemaitre, 1990] suggests using several stabilized hysteresis loops that correspond to different strain amplitudes. Material parameters determined with this method are suitable to be used for different strain amplitudes. Identically with a previous method (see paragraph 4.2.3.2), the plastic strain range ($\Delta\varepsilon_{pl}$) and the stress range ($\Delta\sigma$) are necessary to calculate for each stabilized stress-strain loop.

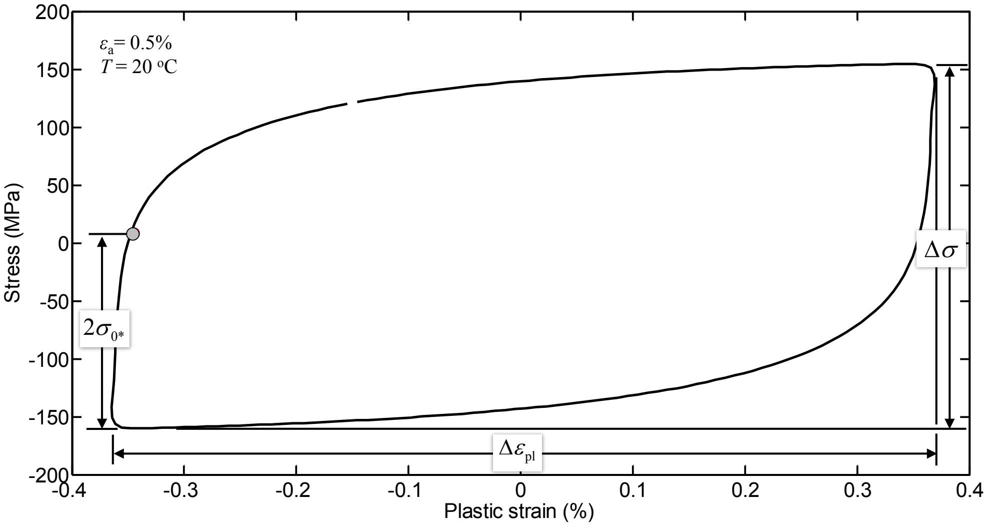

Figure 4.25: Stress vs. plastic strain

The elastic domain ($2\sigma_{0*}$) is roughly 160 MPa considering Figure 4.25 which shows the stabilized stress-strain loop for ε_a=0.5% at 20 °C. Furthermore, the stress range is equal to 306 MPa and the plastic strain range is 0.69%. Subtracting the actual yield stress (σ_{0*}) from the stress amplitude gives the point presented in Table 4.10. Repeating the same procedure for each strain amplitude, finally gives the points listed in Table 4.10 and plotted in Figure 4.26. The fitting procedure, using equation (3.35), is performed for one and two pairs of material parameters. The initial values C_{in} and γ_{in} are calculated from Figure 4.26 as an asymptotic value $C/\gamma \approx 77$ MPa. Subsequently, the initial hardening modulus (C_{in}) is calculated to be approximately 166500 MPa while γ_{in}=2162 is obtained through relation C/γ. As with the second method, the fitting procedure is done using the Curve Fitting Toolbox in MATLAB.

Table 4.10: Points measured from LCF data at $T = 20$ °C

	Strain amplitude (%)					
	0.2	0.3	0.4	0.5	0.6	0.7
σ_a-σ_{0*} (MPa)	46	54.5	63.5	73	75	77
ε_a (%)	0.1	0.16	0.25	0.345	0.44	0.53

Figure 4.26 shows the fitting procedure between calculated points listed in Table 4.10 and curves obtained with 1 and 2 pairs of parameters. As can been noticed, a better correlation between experimental points and fitted curves is obtained with only one pair (C_1, γ_1).

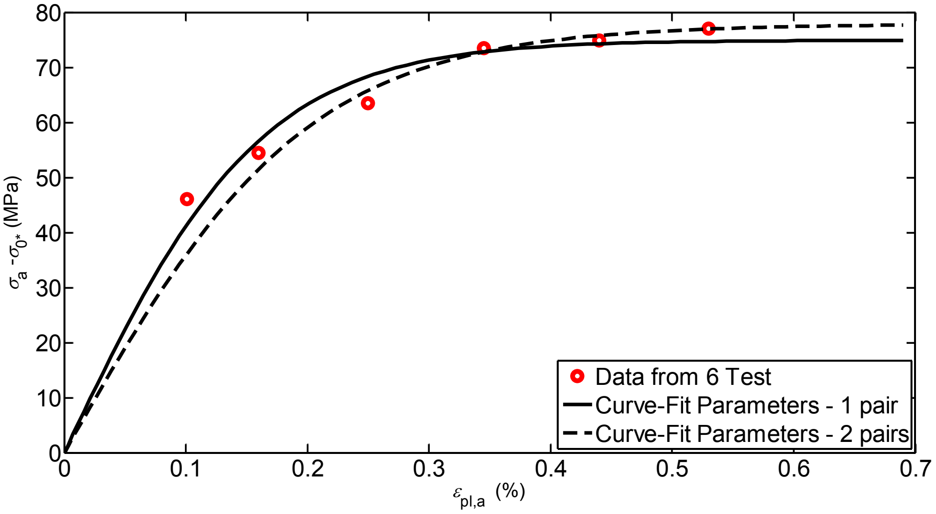

Figure 4.26: Curve fitting with the method of least squares, using data of 6 hysteresis loops - $T = 20$ °C

One and two pairs of material parameters are estimated considering 5 different strain amplitudes at 250 °C and using the same methodological approach explained earlier. Measured points base on which is performed the nonlinear least square fitting procedure are summarized in Table 4.11.

Table 4.11: Points measured from LCF data at $T = 250$ °C

	Strain amplitude (%)				
	0.2	0.3	0.4	0.5	0.7
σ_a-σ_{0*} (MPa)	44.6	45.5	55	57.1	56.4
ε_a (%)	0.12	0.21	0.3	0.39	0.59

Figure 4.27 shows fitting procedure with 1 and 2 pairs of parameters regarding the experimental data measured at 250 °C. As can be seen in Figure 4.27, a better agreement is obtained with only one pair of material parameters.

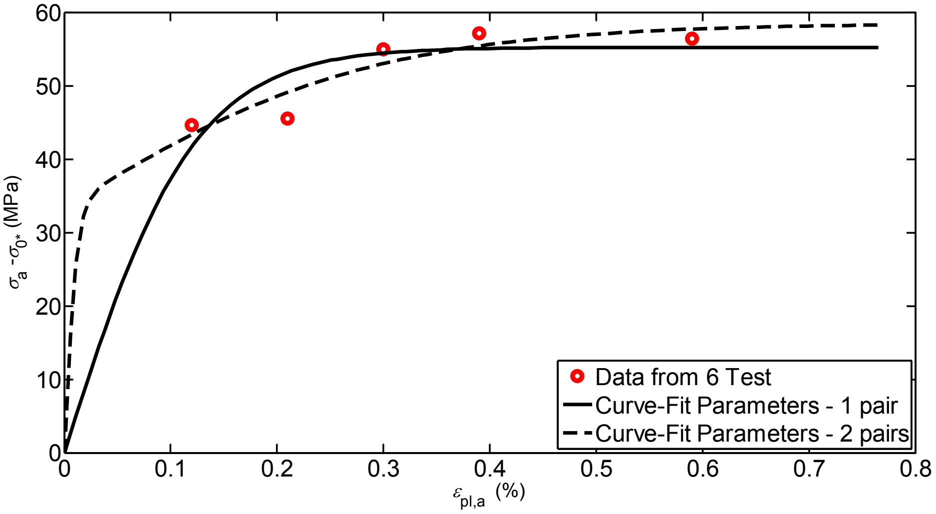

Figure 4.27: Curve fitting with the method of least squares, using data of 5 hysteresis loops - $T = 250$ °C

As in previous two cases, one and two pairs of material parameters are estimated from LCF data at 300°C considering five different strain amplitudes and using the same methodological approach. Measured points base on which is then performed the nonlinear least square fitting procedure are summarized in Table 4.12. As can be seen in Figure 4.28, curves fitted with 1 and 2 pairs of material parameters overlap each other.

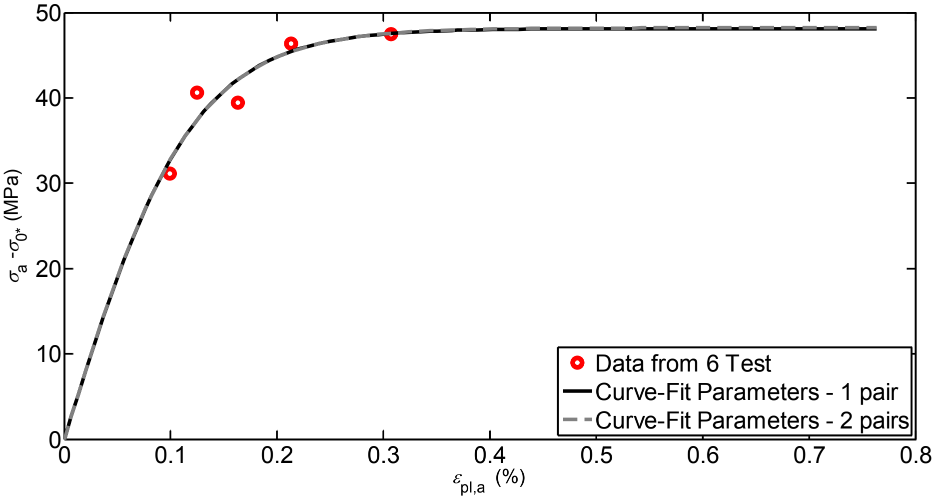

Figure 4.28: Curve fitting with the method of least squares, using data of 5 hysteresis loops - $T = 300$ °C

Table 4.12: Points measured from LCF data at $T = 300$ °C

	Strain amplitude (%)				
	0.175	0.2	0.25	0.3	0.5
σ_a-σ_{0*} (MPa)	31.2	40.6	39.5	46.4	37.4
ε_a (%)	0.1	0.125	0.163	0.21	0.31

One and two pairs of material parameters estimated from LCF experimental data for three temperature levels (20 °C, 250 °C, 300 °C) are summarized in Table 4.13

Table 4.13: Material parameter estimated using the third method

Temp.	One pair		Two pairs			
	C_1 (MPa)	γ_1	C_1 (MPa)	γ_1	C_2 (MPa)	γ_2
20 °C	46250	617.2	38160	505.7	679.5	274
250 °C	45340	820.9	290600	8699	8772	349.5
300 °C	40080	832.8	27530	894.9	12760	731.1

Figure 4.29 - Figure 4.30 show comparison between experimental stabilized loops and stress-strain loops calculated with the numerical simulations. The numerical simulations are performed adopting the example described in paragraph 3.6 and using the average values of the Young's modulus and the actual yield stress. The simulations are done considering one and two pairs of material parameters estimated at 20 °C, 250 °C and 300°C, respectively.

As can be seen in Figure 4.29, better agreement between the experimental and simulated stress-strain loops is obtained with only one pair at 20 °C, 250 °C; while at 300°C one and two pairs give quite the same shape of stress-stain loops.

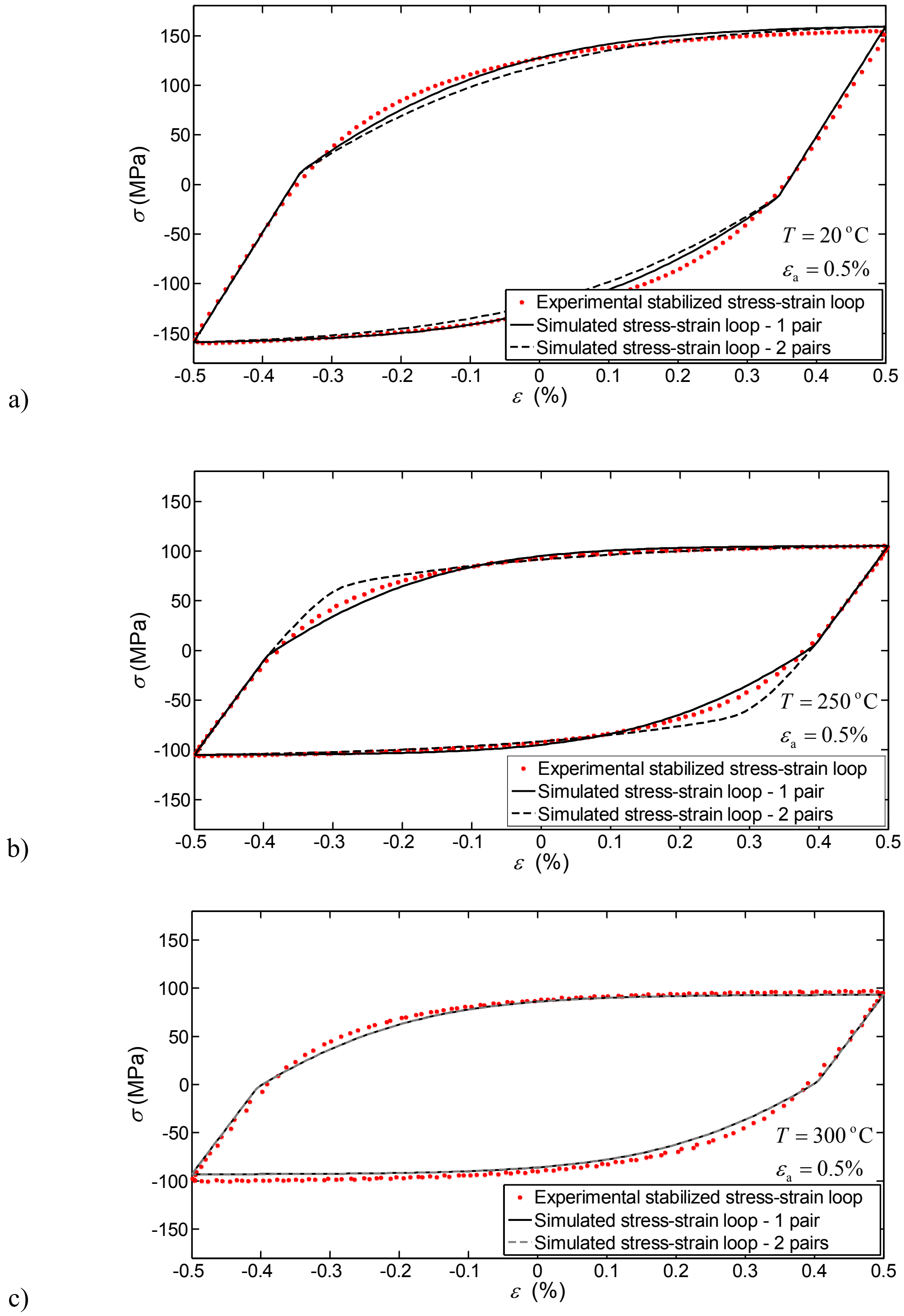

Figure 4.29: Comparison between experimental and simulated stress-strain loops at different temperatures, ε_a=0.5%

Figure 4.30 shows comparison between experimental and simulated stress-strain loops considering different strain amplitudes (ε_a). The comparison is performed in order to confirm that the estimated material parameters are suitable to be used over wider interval of strain ranges. As can be seen in Figure

4.30, a quite good matching with the experimental data characterizes all three cases. Based on the obtained results, it is possible to conclude that nonlinear kinematic model with one pair of the material parameters (e.g. the Armstrong and Frederick's model) gives the best agreement regarding experimental data. Therefore, the Armstrong and Frederick's model is going to be used in following simulations.

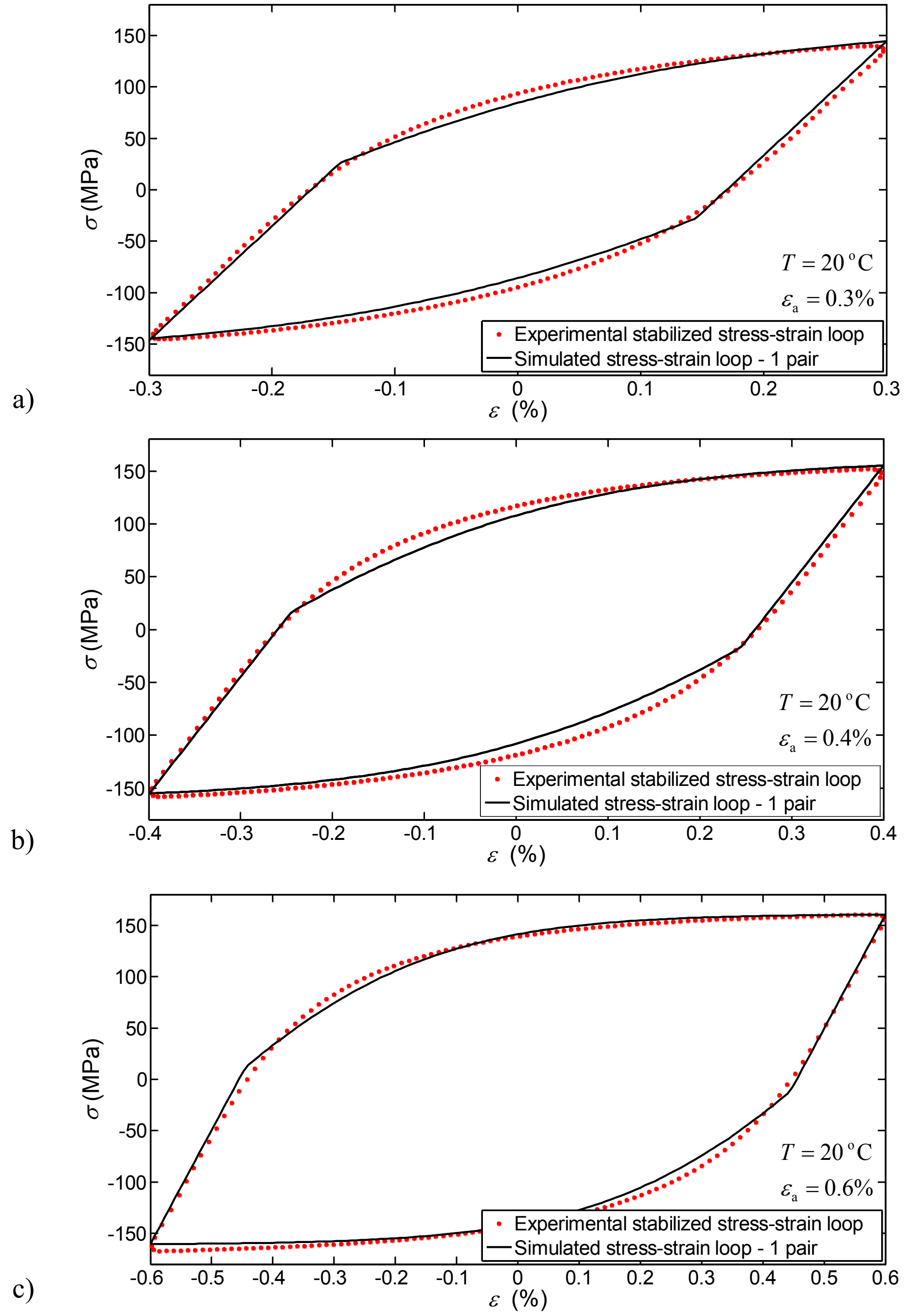

Figure 4.30: Comparison between experimental and simulated stress-strain loops at different strain amplitudes, *T*=20 °C

Figure 4.26, Figure 4.27 and Figure 4.28 show that fitting between experimental data and estimated parameters are not so precisely, however, when the estimated material parameters are used to gain simulated stress-strain loops the fitting between experimental stabilized loop and simulated loops become satisfactory in all cases, see Figure 4.29 and Figure 4.30. It is important to note that on the overall result (fitting between experimental and simulated loops) significantly affect not just accuracy of evaluated material parameters but also accuracy of estimated the Young's modulus and the yield stress.

Table 4.14 shows goodness of fitting considering the material parameters estimated with the second (single stabilized cycle) and the third (several stabilized cycles) method. Evaluation is performed using statistical measures (R^2 and *SSE*). Firstly, the parameters estimated for ε_a=0.2% with the second method are compared regarding ε_a=0.2%, ε_a=0.5% and ε_a=0.7%, respectively. Then, the parameters obtained for ε_a=0.5% and ε_a=0.7% using the second method are compared with ε_a=0.2%, ε_a=0.5% and ε_a=0.7%, respectively. At the end, material parameters estimated with the third method are compared regarding ε_a=0.2%, ε_a=0.5% and ε_a=0.7%.

Statistical measures R^2 and *SSE* are explained in Chapter 6. R^2 can take on any value between 0 and 1, with a value closer to 1 indicating that a greater proportion of variance is accounted for by the model. While *SSE* measures the total deviation of the response values from the fit to the response values. A value closer to 0 indicates that the model has a smaller error component, and that the fit will be more useful for prediction.

Table 4.14: Comparison between second and third method

Strain amplitude (%)		Second Method			Third Method
		$\varepsilon_a = 0.2$	$\varepsilon_a = 0.5$	$\varepsilon_a = 0.7$	$\varepsilon_a = 0.2 \div 0.7$
$\varepsilon_a = 0.2$	*SSE*	208.3	7914.3	13261	3687.6
	R^2	0.9952	0.8180	0.6951	0.9152
$\varepsilon_a = 0.5$	*SSE*	86961.4	2380.2	5837.4	8313.3
	R^2	0.2203	0.9787	0.9476	0.9255
$\varepsilon_a = 0.7$	*SSE*	157960	7560.6	3356.4	10707
	R^2	0.4483	0.9307	0.9692	0.9018

For an example, considering the second method (single stabilized cycle) and ε_a=0.2% (Table 4.14), it can be noticed that fitting is quite precisely for ε_a=0.2% (*SSE*=208.3 and R^2=0.9952); which has been used to estimate material parameters. However, using these parameters for ε_a=0.5% and ε_a=0.7% give a poor fitting in both cases (i.e., $SSE_{0.2\%}$=208.3 < $SSE_{0.5\%}$=86961.4 < $SSE_{0.7\%}$=157960 and $R^2_{0.2\%}$=0.9952 > $R^2_{0.7\%}$=0.4483 > $R^2_{0.5\%}$=0.2203). On the other hand, material parameters estimated using the third method (several stabilized cycles) fit quite precisely for all 3 strain amplitudes, i.e. in all 3 cases the R^2>0.99. Based on obtained results, it is possible to conclude that using the third method to estimate just one pair of material parameters gives satisfactory correlation between experimental and simulated stress strain loops. It is important to note that parameters obtained with several stabilized cycles method cover wider strain range. However, the disadvantage of third method is that it requires a sufficient number of experimental data to obtain representative parameters.

4.2.4 Identification of material parameters for nonlinear isotropic hardening model

The nonlinear isotropic hardening model has two material parameters saturation stress (R_∞) and speed of stabilization (b) to be estimated from LCF data. The saturation stress indicates an amount of hardening or softening and it is determined as the difference in the maximum stress of the first cycle ($\sigma_{\max,1}$) and the stabilized one ($\sigma_{\max,s}$). As can be noticed in Figure 4.31, Figure 4.33 and Figure 4.35, the saturation stress depends on the applied strain amplitude, contrary to the assumption of the nonlinear isotropic model in Equation (3.40). CuAg alloy shows a softening behaviour.

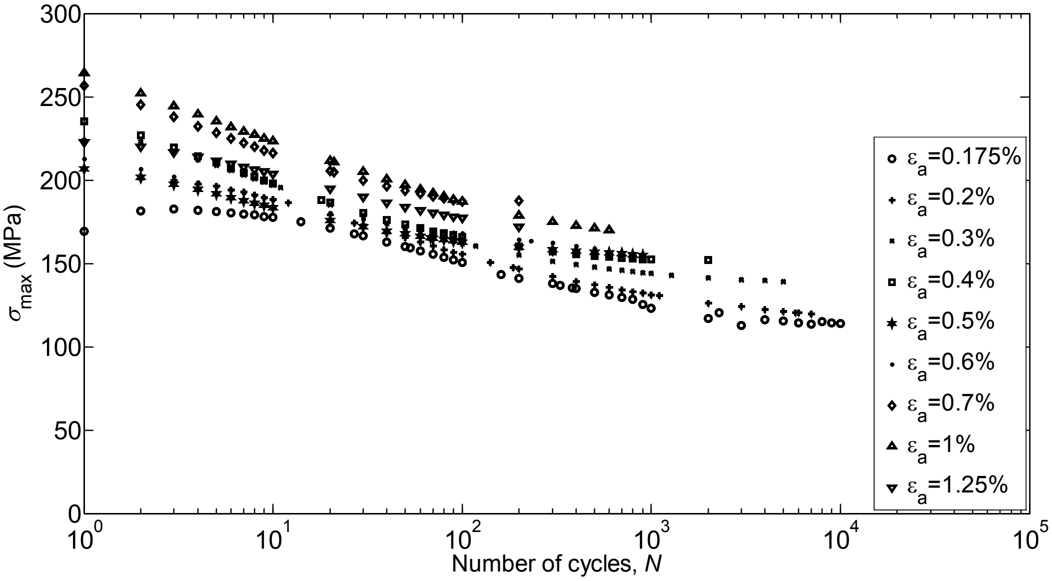

Figure 4.31: Maximum stress as the function of number of cycles - T = 20 °C

The speed of stabilization is estimated using the relation (3.43) proposed by [Chaboche, 2008, Lemaitre, 1990, Lemaitre, 2005]:

$$\frac{\sigma_{\max,i} - \sigma_{\max,1}}{\sigma_{\max,s} - \sigma_{\max,1}} \approx \frac{R}{R_\infty} = 1 - \exp\left(-b\varepsilon_{\mathrm{pl,acc}}\right) = 1 - \exp\left(-2b\Delta\varepsilon_{\mathrm{pl}}N\right)$$

If $\Delta\varepsilon_{\mathrm{pl}}$ is the plastic strain range over a cycle, the accumulated plastic strain for N cycles is $\varepsilon_{\mathrm{pl,acc}} \approx 2\Delta\varepsilon_{\mathrm{pl}}N$. As can be seen in Figure 4.32, Figure 4.34, Figure 4.36, a reasonable correlation is obtained, although a modification of the evolution rule of R seems necessary for CuAg alloy; since the relation (3.43) was originally used for steel 316 in [Lemaitre, 1990]. This kind of behaviour was also observed in [Zhao, 2001] for a nickel based superalloy. One of the future plans could be to create a new relation which is able to give a better fitting. However, a new relation is necessary to implement in the finite element numerical software what requires addition work. Obtained values of R_∞ and b for each strain amplitude are summarized in Table 4.15.

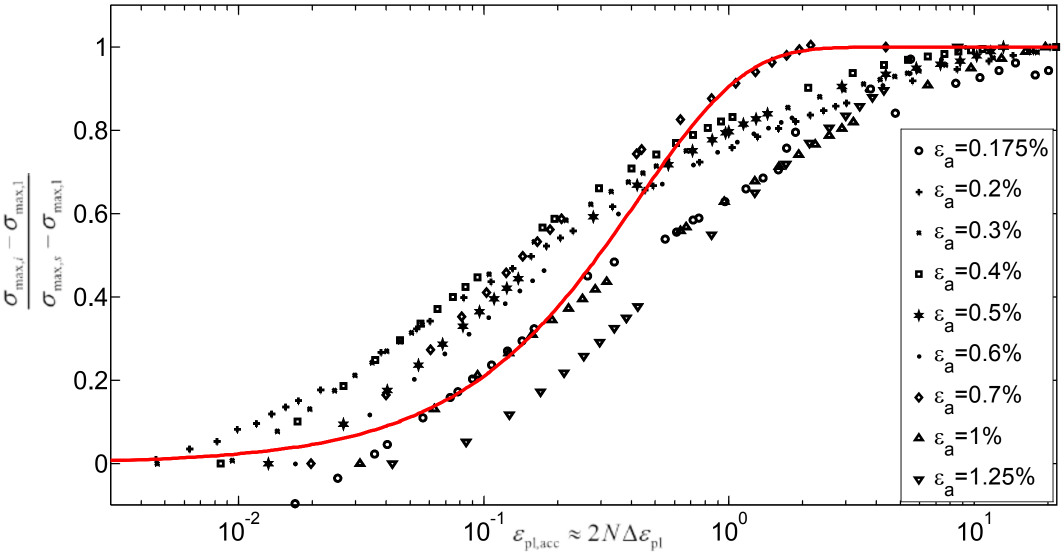

Figure 4.32: The identification of the isotropic parameter b - $T = 20$ °C

Table 4.15: Estimated isotropic parameters for $T = 20$ °C

Parameter	Strain amplitude (%)									Average value
	0.175	0.2	0.3	0.4	0.5	0.6	0.7	1	1.25	
R_∞ (MPa)	-58.1	-80.9	-84.4	-83.2	-52.1	-54.1	-69	-96.1	-103.9	-75.7
b	1.197	3.724	3.620	4.488	2.871	2.580	4.208	1.192	0.840	2.352

The material parameters (R_∞, b) are estimated from experimental data for temperature levels 250 °C and 300 °C using the methodological approach explained earlier. Plotting the maximum stress versus number of cycles is possible to determine the amount of the saturated stress (R_∞), as can be seen in Figure 4.33. The CuAg alloy shows the cyclic softening behaviour also on T=250 °C. Figure 4.34 represents fitting procedure of b parameter. Both parameters (R_∞, b) are estimated considering 5 different strain amplitudes measured at 250 °C. As it has been explained earlier, modification of the evolution rule of R seems necessary for CuAg.

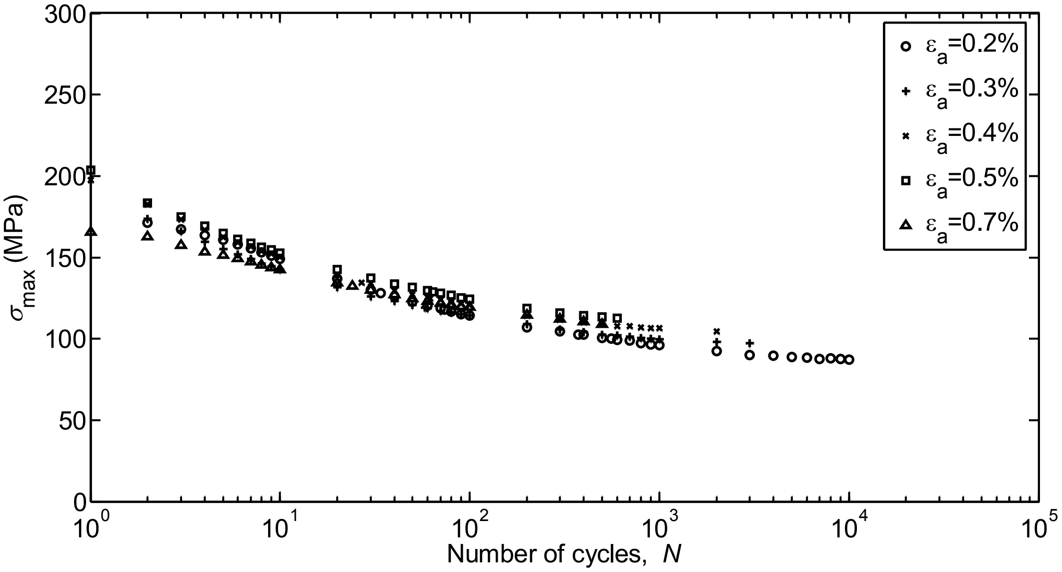

Figure 4.33: Maximum stress as the function of number of cycles - T = 250 °C

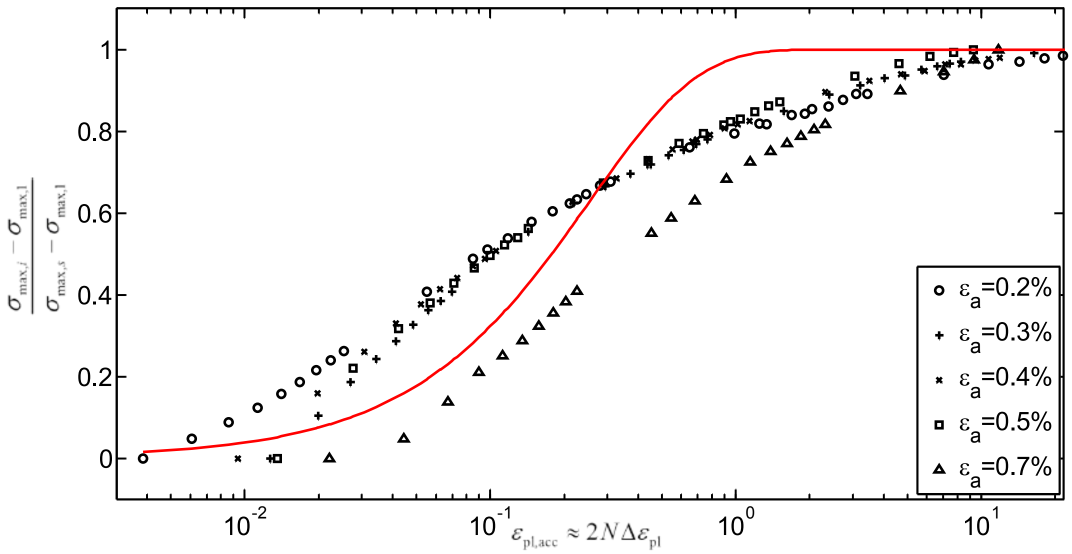

Figure 4.34: The identification of the isotropic parameter b - T = 250 °C

Estimated values of R_∞ and *b* from LCF data at 250 °C are summarized in Table 4.16.

Table 4.16: Estimated isotropic parameters for $T = 250$ °C

Parameter	Strain amplitude (%)					Average value
	0.2	0.3	0.4	0.5	0.7	
R_∞ (MPa)	-84	-76.5	-93	-90.9	56.4	-80.2
b	5.395	3.898	5.099	5.780	1.484.	3.894

Identification procedure of isotropic parameters (R_∞, *b*) is demonstrated in Figure 4.35 and Figure 4.36, respectively, considering 5 different strain amplitudes measured at 300 °C. As can be seen in Figure 4.35, CuAg alloy shows the cyclic softening behaviour also on T=300 °C. Figure 4.36 represents fitting procedure of *b* parameter; also in this case, additional modification of the evolution rule of *R* seems necessary. Material parameters (R_∞, *b*) determined from LCF data at 300 °C are listed in Table 4.17.

Table 4.17: Estimated isotropic parameters for $T = 300$ °C

Parameter	Strain amplitude (%)					Average value
	0.2	0.3	0.4	0.5	0.7	
R_∞ (MPa)	-79.5	-82	-76.2	-64.4	-80.7	-76.6
b	5.617	7.393	6.123	4.917	4.150	5.293

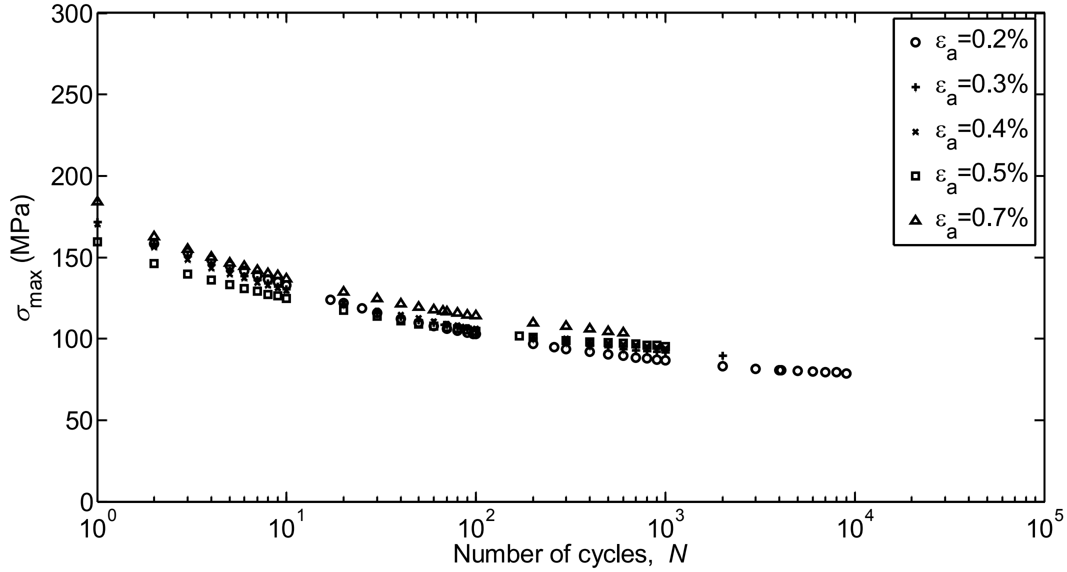

Figure 4.35: Maximum stress as the function of number of cycles - $T = 300$ °C

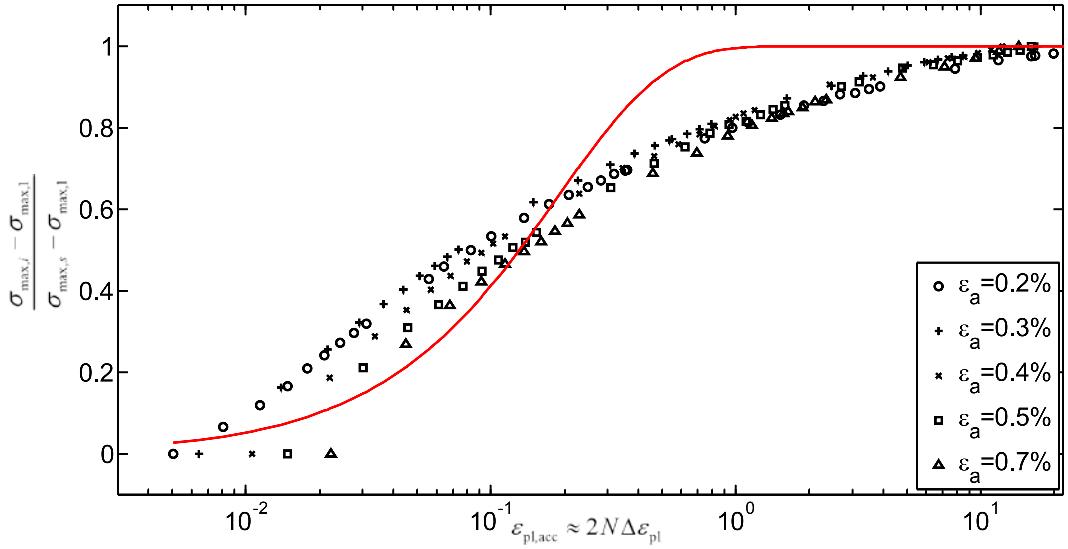

Figure 4.36: The identification of the isotropic parameter b - T = 300 °C

The numerical simulation with the combined material model is performed once all material parameters for the nonlinear kinematic and the nonlinear isotropic model are estimated. The simulation is performed considering the average values of the Young's modulus and the yield stress (E_1 and σ_0) presented in Table 4.4 and Table 4.1, respectively. While, material parameters used for simulation are presented in the Table 4.13 for the Armstrong and Frederick's model and in the Table 4.15 for the nonlinear isotropic model. The simulation assumes only 50 cycles. Figure 4.37 shows obtained stress-strain loops. Due to small value of b, the material model needs more than 50 cycles to reach the stabilized condition. Moreover , as can be seen in Figure 4.37, simulated stress-strain loops fits reasonable well regarding to experimental data (1st and stabilized cycle). Every 5th simulated stress-strain loop is plotted for a better overview.

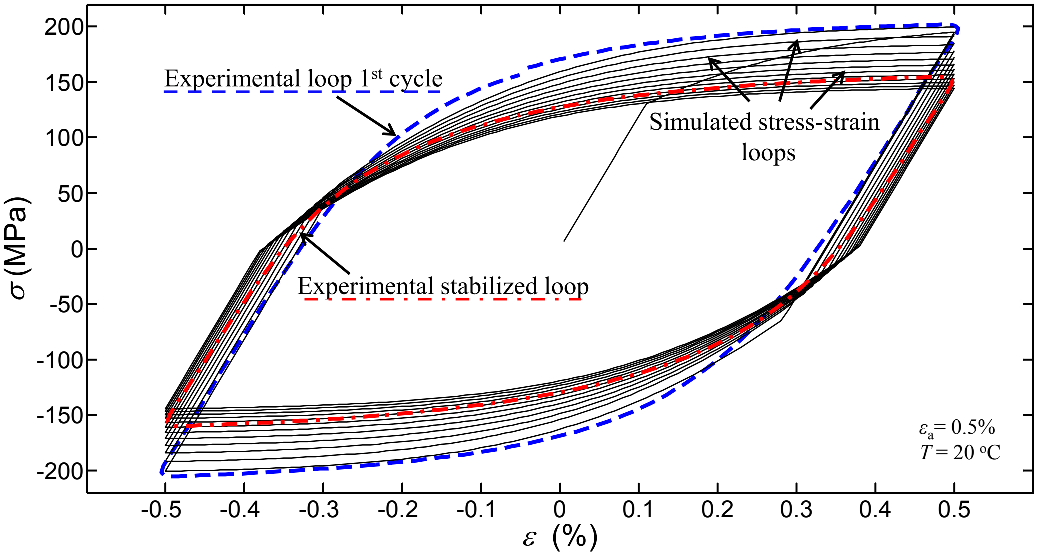

Figure 4.37: Comparison between experimental and simulated stress strain loops for combined model

The material parametrs estimated in Chapter 4 are going to be used as a input data to performe the thermo-mechanical analysis. Following Chapter 5 describes and presents results obtained form the thermo-mechanical analysis where as a study case is goint to be considered a copper mould for continuous casting.

Chapter 5

Thermo-mechanical analysis of the copper mould

In general, mechanical components in steel-making plants are often exposed to cyclic thermo-mechanical loadings and then exhibit cyclic elasto-plastic behaviour and fatigue damage. In continuous casting lines, a typical example is a copper mould where the molten steel is cooled and first shaped. Several publications [Ansoldi, 2012, Ansoldi, 2013, Mahapatra, 1991a, Mahapatra, 1991b, Park, 2002a, Park, 2002b] have been published so far with the focus on a mould behaviour and problems which occur during the working process. Thermal cracks occur at the inner surface of the component due to difficult operative conditions [Ansoldi, 2012, Ansoldi, 2013, Park, 2002a, Park, 2002b]. Since a mould without cracks and with close dimensional tolerance contributes to safety in the working process and quality of the final product, it is preferable to perform a thermo-mechanical finite element (FE) analysis to identified the most damage parts of the mould and then for those places check a stress-strain distribution.

A thermo-mechanical finite element analysis requires beside well defined numerical model also suitable material models to properly simulate the cyclic elasto-plastic material response of a component under thermo-mechanical loading. The first criterion for model selection should be the capability of a material model to correctly represent material behaviour observed in experiments. However, it may be sometimes difficult, especially for non-experienced engineers, to understand which model is most suitable for their application, or which parameters do really affect the material response.

Several material models, previously described in Chapter 3, have been adopted for the mechanical analysis. For each material model, obtained stress-strain distributions are compared and discussed. At the end of Chapter, the sensitivity analysis is performed in order to emphasis importance of the choosing appropriate material parameter and its influence on the obtained results.

5.1 Description of the component

Continuous casting is a process in which molten steel is solidified into a semi-finished billet, bloom or slab depending on the final application.

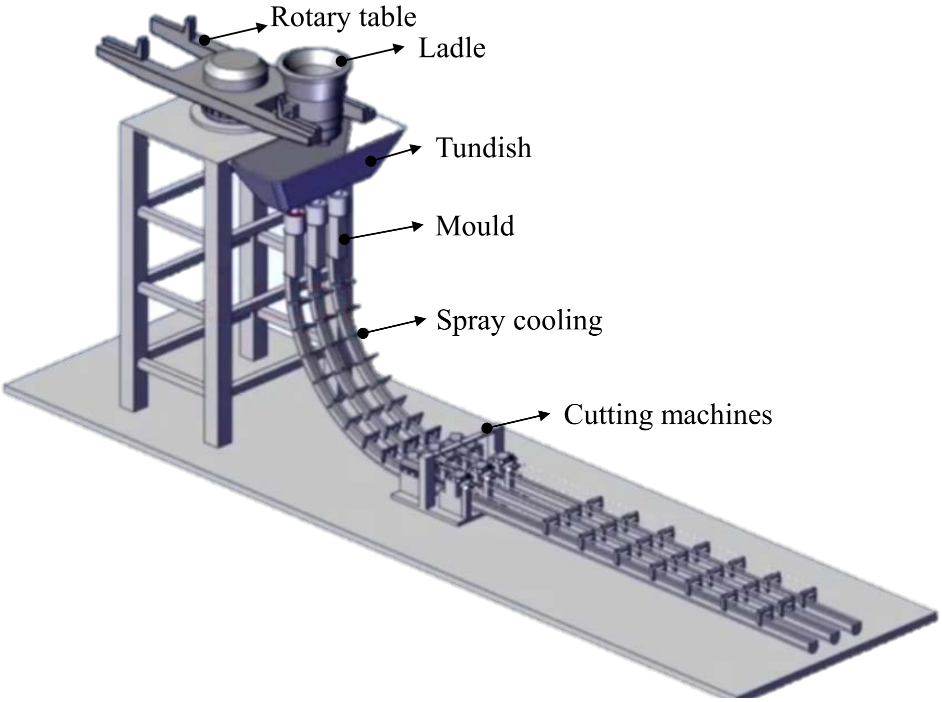

Figure 5.1: Continuous casting process of steel [www.steeluniversity.org]

Figure 5.1 shows the main parts of the continuous casting process. A ladle is filled out with molten steel which was previously melted in the special furnaces. A rotary table holds and moves the ladle from the charging to a pouring position. Once the ladle is placed to a pouring position, the molten steel passed from the ladle to a tundish. The tundish is a container that is placed above the mould and holds the molten steel for the casting. The casting process uses the gravity force to fill the mould and to move the strand along the process. The main function of the tundish is to keep the mould filled to the right level throughout the manufacturing operation since the metal casting is constantly moving through the mould. The molten steel passes through a water cooled mould (crystallizer). The mould is water cooled to speed up the solidification of the metal casting. The main function of the mould is to establish a sufficient strong solid shell to contain a liquid core during the secondary spray cooling zone. Once the metal strand comes out from the mould, it is supported by rollers. The rollers help guide the metal strand and assist in the smooth flow of the strand out of the mould. Cutting machines are placed at the end of the continuous casting process. Typically cutting machines are a torch or a saw. [Ansoldi, 2012, Elfsberg, 2003, Barella, 2014, Park, 2002a, Thomas, 2002]

A mould is the most critical component of the process, which controls initial solidification and determines surface quality [Park, 2002a, Park, 2002b, Thomas, 2002]. The observed mould is a long cylinder with a hollow square cross section. The molten steel flows from the upper part of the mould to the bottom part where the steel exits with a thin solidified shell. The upper part of the mould is hung to a surrounding steel frame with no additional imposed mechanical constrained. A mould is usually made of copper alloys because of their high conductivity that helps the solidification of the steel. The mould considered in this study is made of CuAg alloy. During the solidification of the steel, a huge thermal flux (q) passes from the molten steel to the inner surface of the mould, which is then subjected to high temperatures. As a result, considerable stresses and plastic strains are induced in the mould, which leads to deformations and thermal cracks at the inner surface.

The thermal flux varies between two conditions: when the plant is switched on the thermal flux increases until reaching the maximum value $q_{\max}$, while thermal flux is absent once the plant is switched off, see Figure 5.2.

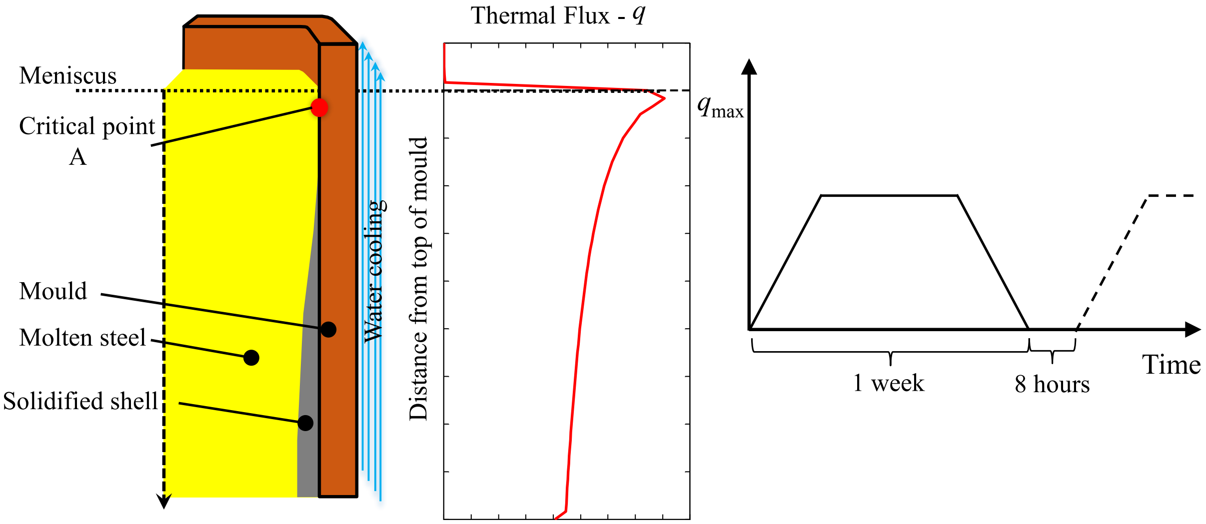

Figure 5.2: Schematic description of mould working conditions

Approximately one week lasts a period from switching on to switching off the plant due maintaining. The plant is switched on again once the maintaining is finished (after ≈ 8 hours). This cyclic process repeats until a quality of the final product decrease due to damage observed at the inner surface of the mould. When the quality of the final product decreases the used old mould must be replaced with a new one. The mould without cracks and with close dimensional tolerance contributes to the safety in working process and quality of the final product [Park, 2002a]. Sometimes, cracks were observed after only 2 or 3 casting sequences, furthermore, most of the cracks formed just below the meniscus [Park, 2002b].

5.2 Numerical simulation

A three dimensional (3D) finite element model is used as it allows one to represent a non-uniform distribution of the thermal flux through the length, while thermal flux is assumed to be constant compared to a cross-section of the mould. Since the model has two planes of symmetry only ¼ of the complete model has been modelled. During the development process of 3D numerical model, one of the most important steps is generating and optimizing a mesh to reduce the computational time and at the same time obtain an accurate solution. As can be seen in Figure 5.3 a), the numerical model has been divided in 18 areas (6 through the length and 3 in a cross-section) in order to refine the mesh near meniscus, i.e. region where plastically deformations occur. While bottom part of model, which is elastically deformed-less stressed, has elements large enough to reduce computational time (see Figure 5.3 b). The model has a total of 57024 elements and 63973 nodes. Once the mesh is optimized and generated, the nonlinear thermo-mechanical analysis requires ≈ 15 min to compute 1 cycle.

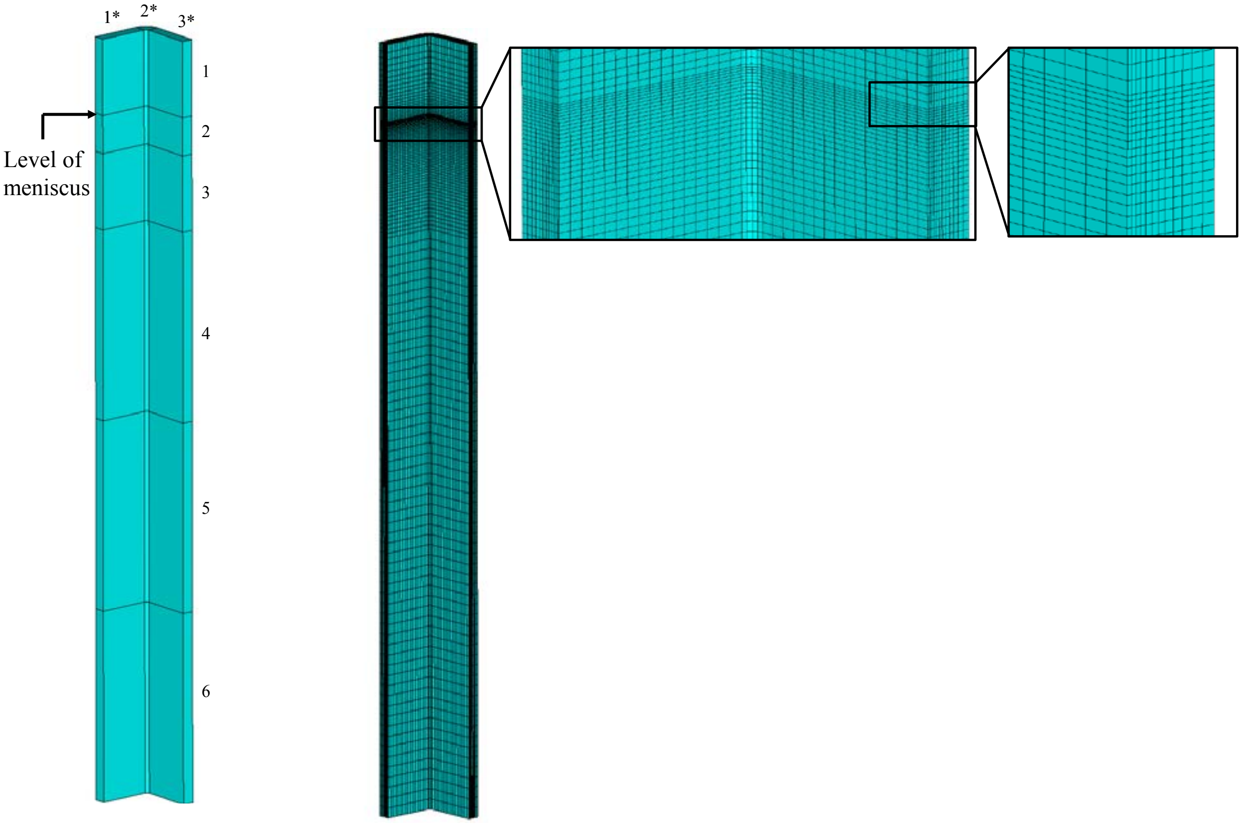

a) Divided areas

b) Generated mesh

Figure 5.3: Numerical model

The thermo-mechanical numerical analysis is performed. In the thermal analysis, 8-node brick thermal elements are used (SOLID70 in ANSYS®). Thermal flux is imposed on the inner surface of the model, while a convective boundary condition is imposed on the outer surface to simulate water cooling. Temperature of the cooling water is 40 ^{o}C and the convection coefficient is 48000 W/m^{2}K. Static thermal analysis could be a satisfactory approximation, since a load cycle occurs in a quite long period of time (1 week) required to achieve the steady state condition, see Figure 5.2. A nonlinear thermal analysis is needed in order to take into account temperature dependence of the thermal conductivity as well as specific heat. The nodal temperature distribution obtained from the thermal analysis is the input data for the mechanical simulation. In the mechanical simulation 8-node brick mechanical elements are used (SOLID185 in ANSYS®). The model is free to expand since no mechanical constraints are imposed; therefore, stress-strain distribution depends only on the temperature distribution in the model. Pressure of the molten steel, which acts on the inner mould surface, is very small and then it was not considered in simulation. Temperature dependence of the Young's modulus, the yield stress and material parameters for adopted material models are taken into consideration. The combined material model (Armstrong and Frederick's model + nonlinear isotropic model), adopted for this simulation, has been implemented similar as in paragraph 3.6.3. However in this case, the temperature dependence of material parameters has been taken into consideration.

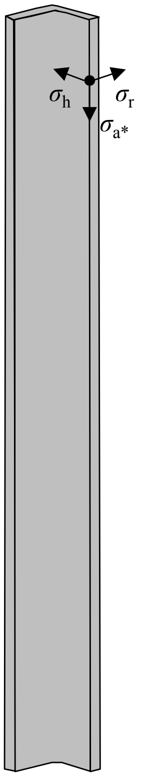

Figure 5.4: Scheme of stress components

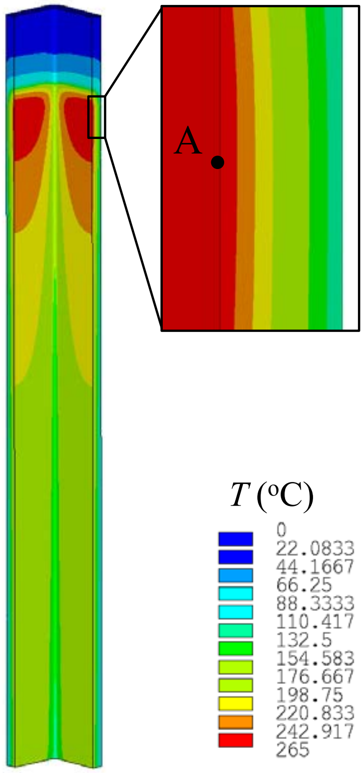

Figure 5.5: Temperature distribution at q_{max}

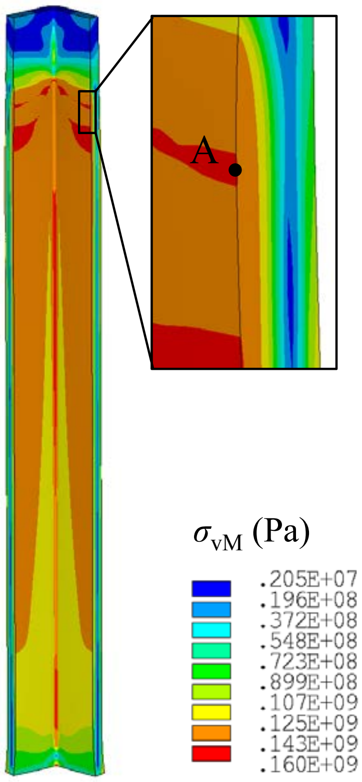

Figure 5.6: Von Mises stress distribution

The temperature distribution obtained at the maximum thermal flux ($q_{\max}$) is shown in Figure 5.5. The maximum temperature appears near the meniscus area (in the point A), where also the highest thermal gradient across the thickness occurs and causing high thermal stresses. Figure 5.6 shows von Mises stress distribution at the $q_{\max}$ for 20th cycle (red dot on Figure 5.7) calculated by the combined model. The most critical point A in the model is located 30 mm below the meniscus level. The critical point A corresponds with the located area investigated in [Park, 2002b].

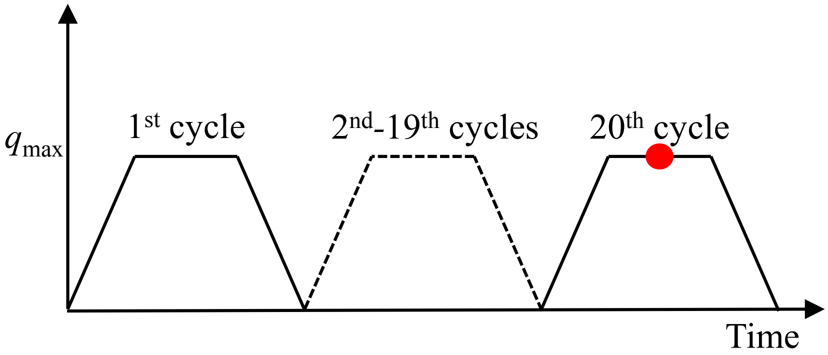

Figure 5.7: Scheme of cycles

It is decided to simulate only 20 cycles in order to obtain representative stress-strain evolution in some reasonable time. Approximately 5 hours (1 cycle ≈ 15 min) is needed to simulate 20 cycles. Figure 5.8 shows ″hoop″ - σ_h, ″axial″ - σ_{a*} and ″radial″ - σ_r stresses and strains measured at the critical point A adopting the combined material model. The ″hoop″ component is parallel to the mould inner surface. ″Axial″ represents stresses and strains in axial direction, while ″radial″ is perpendicular to the inner mould surface, see . In the first cycle temperature of the component increases, consequently compressive stresses appear because the lateral thermal expansion is constrained. It can be noticed that the ″axial″ and the ″hoop¨ stresses show similar compressive values which decreases linearly maintaining quite comparable values, see Figure 5.8 a. On the other hand, the ″radial″ stress is negligibly small as can be seen in Figure 5.8 a-d. The plastic strains occur because developed compressive stresses exceed the yield stress. Therefore, it can be concluded that the hottest part, in which is detected the critical point A, undergoes a plane hydrostatic state of stress.

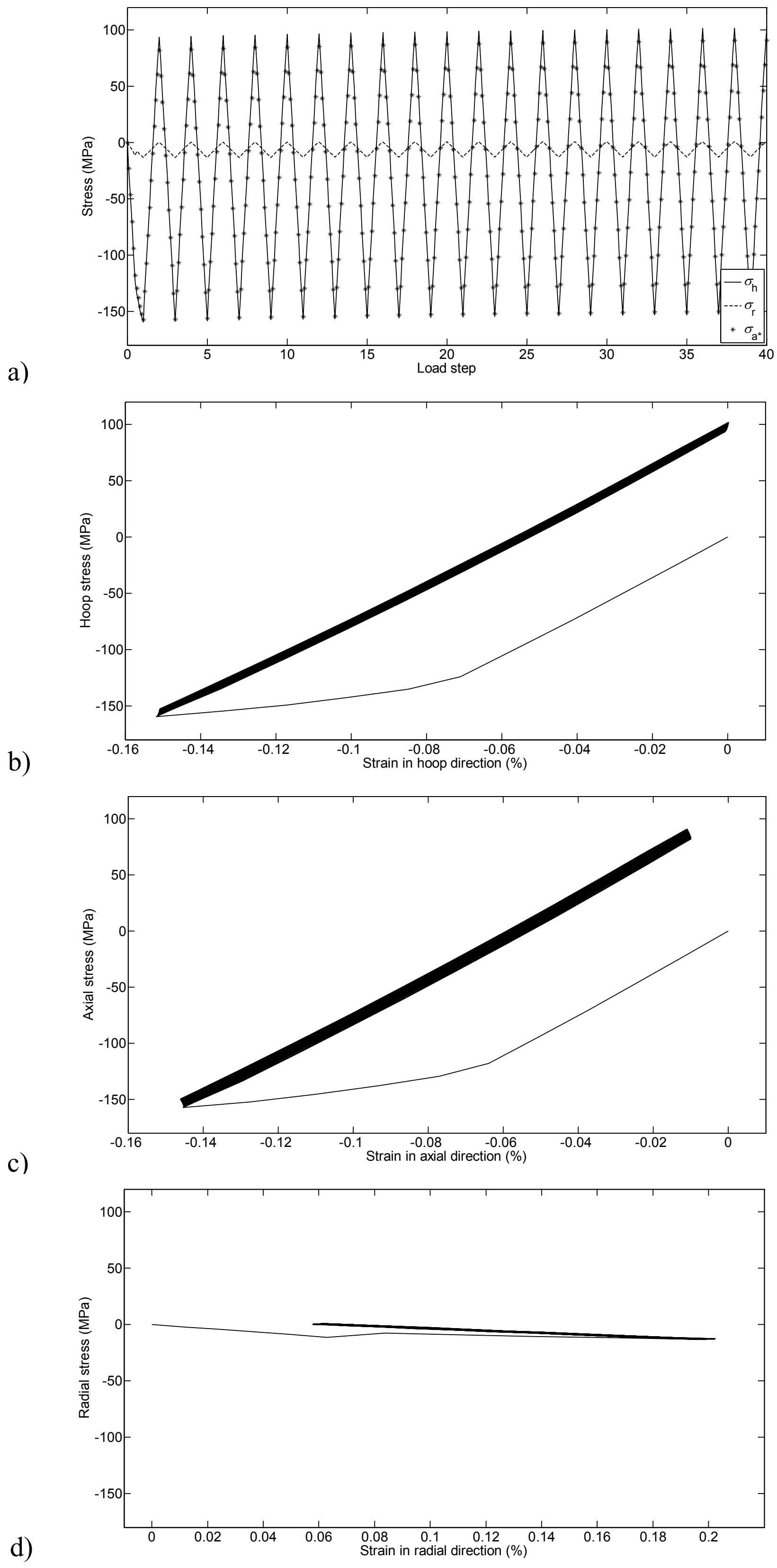

Figure 5.8: Cyclic stress-strain evolution in the critical point A – Combined model

5.2.1 Comparison of different material models

Four different material models are considered and compared in this section:

Model 1	**Model 2**	**Model 3**	**Model 4**
Linear kinematic model	*Combined model* (Armstrong & Frederick's + nonlinear isotropic)	*Stabilized model*	*Accelerated model*

Table 5.1 shows parameters for the linear kinematic – Prager's model where C_{lin} is the initial hardening modulus calculated from tensile tests of CuAg alloy at three temperature levels.

Table 5.1: Linear kinematic material parameters used in the numerical simulation

Temp.	C_{lin} (MPa)
20 °C	37439
250 °C	18039
300 °C	18466

Approximate number of cycles needed to reach the stabilized condition can be calculated using the relation $2bN\Delta\varepsilon_{\mathrm{pl}} \approx 5$ proposed in [Chaboche, 1986b]. The relation states that a value near 5 is a good saturation criterion. Simulating around 60 567 cycles would be necessary to reach a stabilized stress-strain cycle considering the critical point A and adopting the combined material model, for $\Delta\varepsilon_{\mathrm{pl}}=1.06\mathrm{x}10^{-5}$ calculated by FEM and b=3.894. Simulation of such huge number of cycles requires unfeasible computational effort and time (≈ 630 days). For this reason some alternative models as the accelerated model described in paragraph 3.5.4 and the stabilized model described in paragraph 3.5.5 will be used for simulations of the copper mould. The accelerated material model takes the rapidity of stabilization into consideration. By increasing the coefficient b, the stabilized stress-stain cycle is possible to reach with smaller number of cycles. As can be seen in Figure 5.9, the stabilization is reached within 20 cycles with b=100.

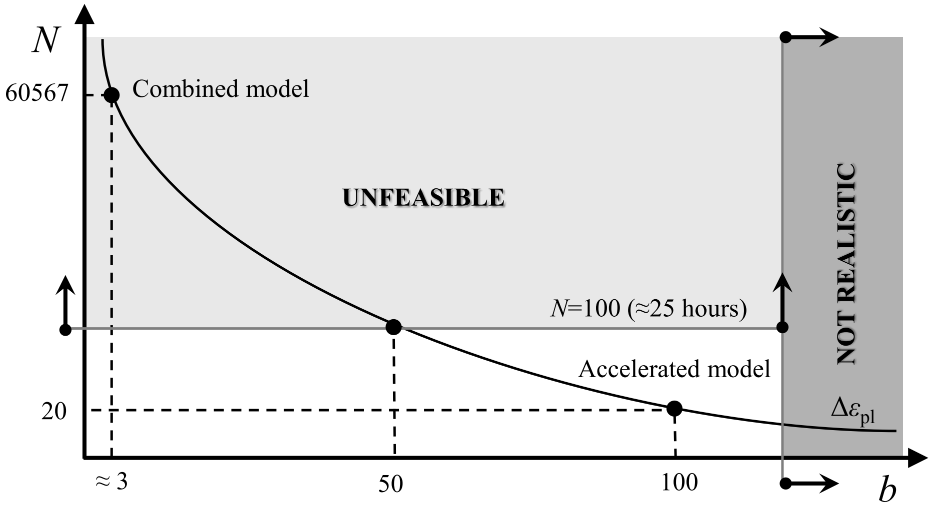

Figure 5.9: Number of cycles to stabilization versus speed of stabilization

Instead, the stabilized material model is considered to be when R reaches R_∞. Material parameters C and γ used in stabilized model are the same as for the Armstrong & Frederick's model. However in this case, the parameters E_1 and σ_0 are replaced with E_s and σ_{0*}, which correspond to the stabilized cycle.

The linear kinematic model is not able to simulate cyclic softening; however, it can give roughly overview of component behaviour under thermo-mechanical loading. Moreover, estimation procedure of parameters for the linear kinematic model is simply and does not require a lot of time to obtained necessary parameter E_t. Figure 5.10 shows only ″hoop″ stress-strain evolution considering different material models, since similar trend can be obtained considering ″axial″ stresses and strains.

Compressive stresses appear as the temperature of the component increases in the first cycle because the lateral thermal expansion is constrained. The component starts to plastically deform once developed compressive stresses exceed the yield stress. Using the stabilized material model, yielding occurs at lower stress in the first cycle, consequently, model overestimates the plasticization phenomena already in the first cycle. Tensile stresses appear during the cooling phase. Depending on the type of the material model, elastic or elasto-plastic behaviour is observed in successive cycles. For example, the combined material model shows a predominant elastic behaviour. Consequently, the nonlinear isotropic softening material model, which is dependent on plastic strain, has slight influence on behaviour of the combined model. Therefore, a huge number of cycles have to be simulated to reach the stabilized stress-strain state. The stabilized model instead shows an elasto-plastic behaviour. The accelerated model with imposed b=100 has reached the stabilized stress-strain cycle within 20 cycles, proofing that it is suitable to use for design purposes.

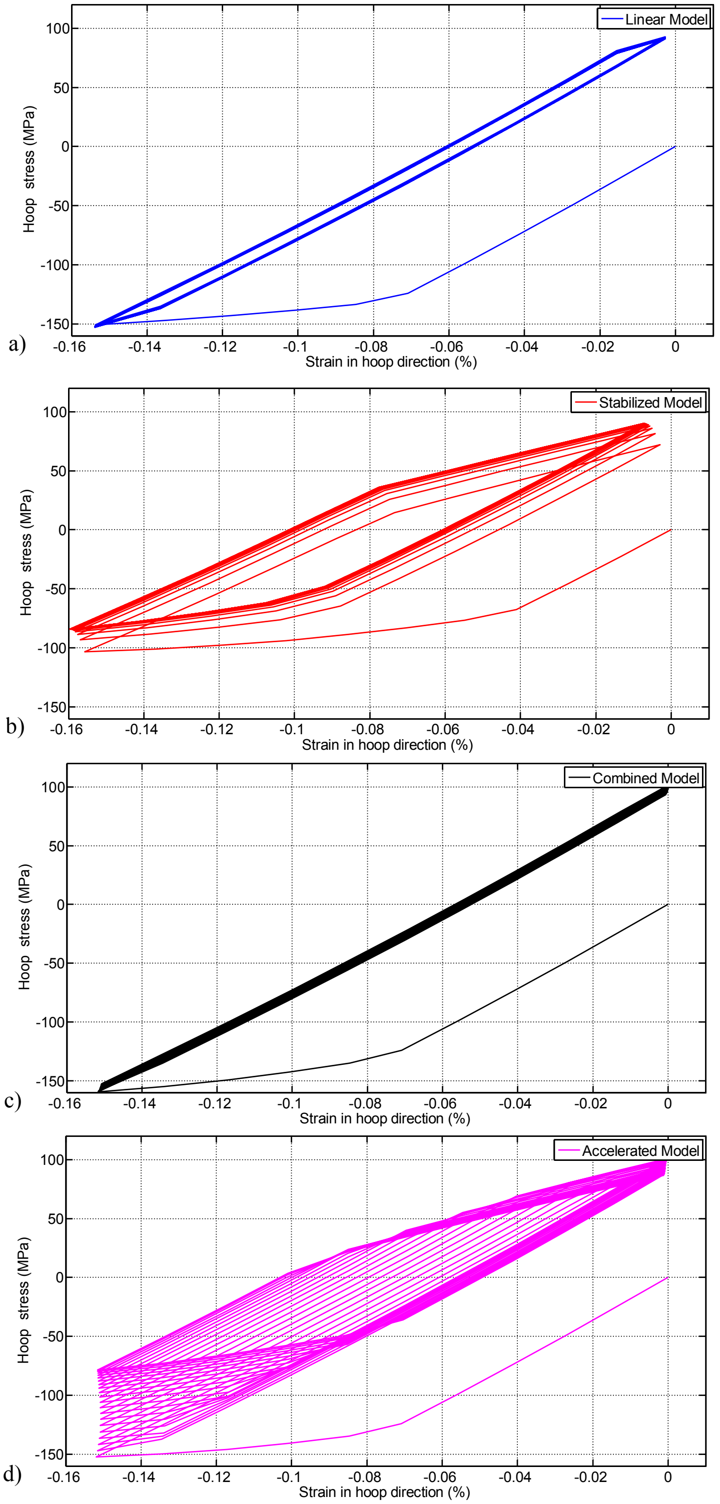

Figure 5.10: Cyclic “hoop” stress-strain evolution considering different material models

5.2.2 Accelerated material model - influence of b parameter

In the previous paragraph, it has been shown that the combined material model requires around 60 567 cycles (≈ 630 days of computation) to reach the stabilized condition. However, simulating such huge number of cycles requires unfeasible computational effort and time. Therefore, as an alternative model has been proposed to use the accelerated model by [Chaboche, 1986b]. Since the accelerated model takes into consideration the speed of stabilization, the stabilized cycle is possible to reach simulating less number of cycles by increasing *b* parameter.

The sensitivity analyses are performed considering the *b* parameter. The goal of the sensitivity analyses is to investigate response of the model considering various values of *b*. The mechanical analyses are performed with the same material parameters as for the combined material model except *b* for which 6 different values are considered 400, 350, 300, 200, 100, 50, respectively. “Hoop” stress-strain evolution for the critical point A (explained at the beginning of section 5.2) and for 20 cycles are plotted in Figure 5.11. Number of 20 cycles is chosen to perform complete analysis within reasonable time (≈5 hours).

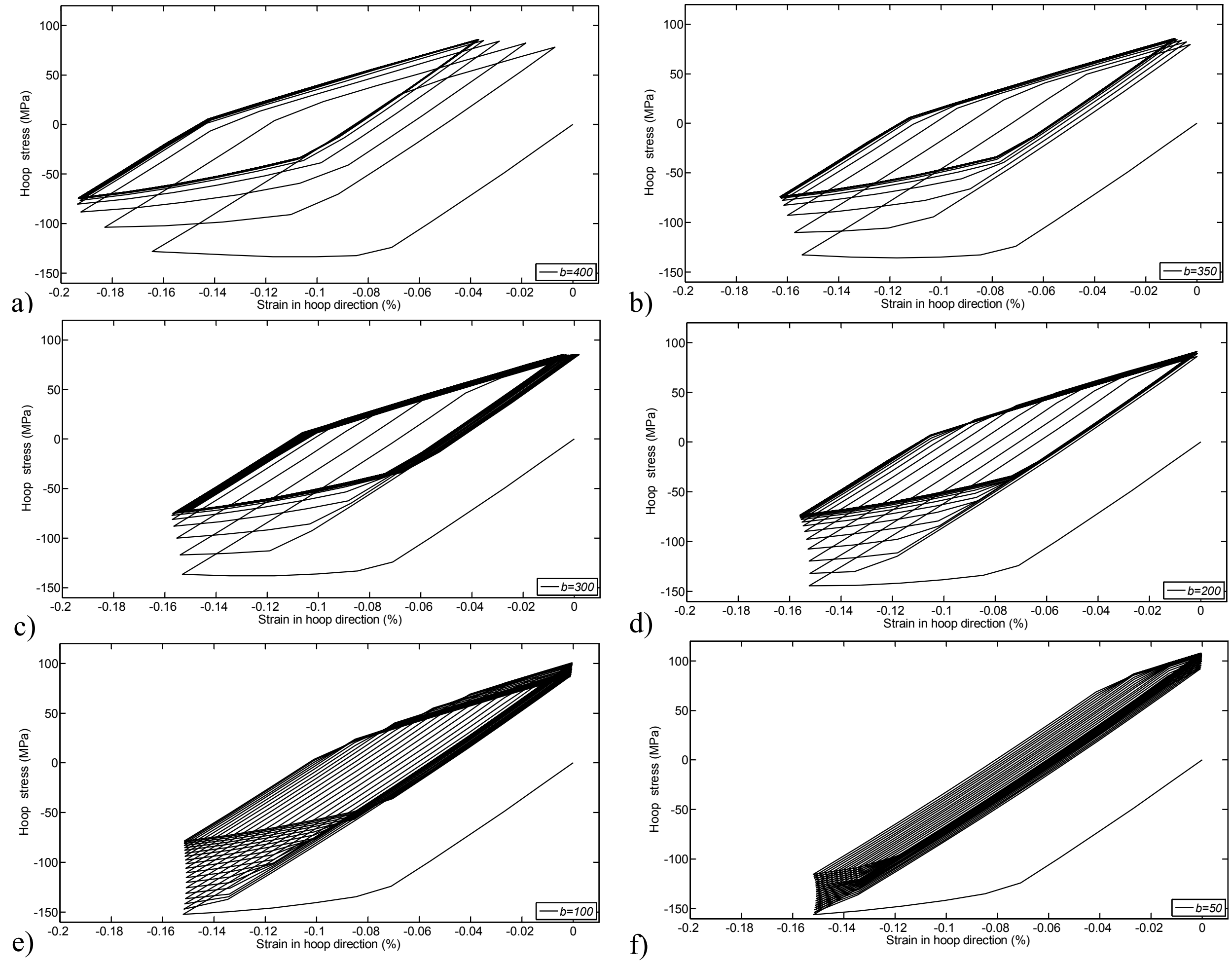

Figure 5.11: Cyclic “hoop” stress-strain evolution considering the accelerated model with different values of *b*

5.3 Metallurgical analysis of the copper mould

In the continuous casting process, the molten steel flows from the upper to the bottom part of the mould where the cast strand exits with thin solidified shell, see Figure 5.2. The inner surface of the mould is often plated with chromium or nickel to provide a harder working surface [Barella, 2014]. During the solidification of steel, the huge thermal flux, q, passes from the molten steel to the inner surface of the mould, which is then subjected to high temperatures. As consequences the high thermal gradient takes place across plates and cause creating of thermal cracks at the inner surface in the area near meniscus [Park, 2002b].

Figure 5.12: Copper mould under investigation

The metallurgical analysis has been carried out to determine failure and damages which had been occurred on the copper mould. So far, similar studies have been performed by [Barella, 2014, Park, 2002b]. Metallographic and SEM (scanning electron microscope) analyses have been performed to characterize the mould microstructure. Figure 5.12: shows the mould under investigation. Firstly, the mould was examined visually and cut in half over the length. The inner surface of the mould after severs sequences of production is presented in Figure 5.13. A closer examination of the mould inner surface shows that cracks are formed in the region near the meniscus. The most damaged area is approximately 130 mm from the mould top, i.e. in the level where the maximum temperature occurs

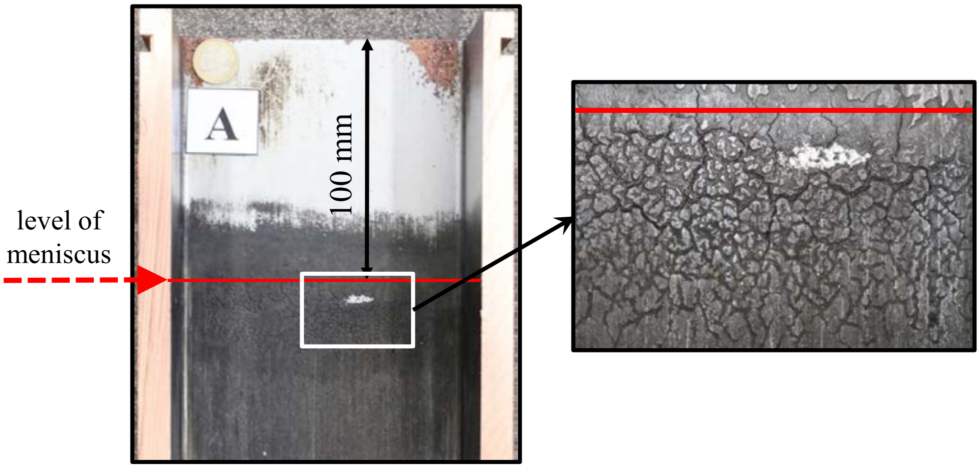

Figure 5.13: Closed view of the mould inner surface near the level of meniscus

Moreover, the mould was cut into several samples to carry out SEM examination of the damaged and undamaged areas. As can be seen in Figure 5.14, overall 14 samples were cut at different positions of interest. Samples were named as A01, A02, A03, A04 (samples taken from corners in the level of meniscus), A1, A1_1, A1_2, A2, A3, A4 (samples taken from walls in the level of meniscus), B1, C1, D1 and E1. All samples were grinded and polished, while etching was performed with solution H_2O : NH_3: H_2O_2 = 1:1:1.

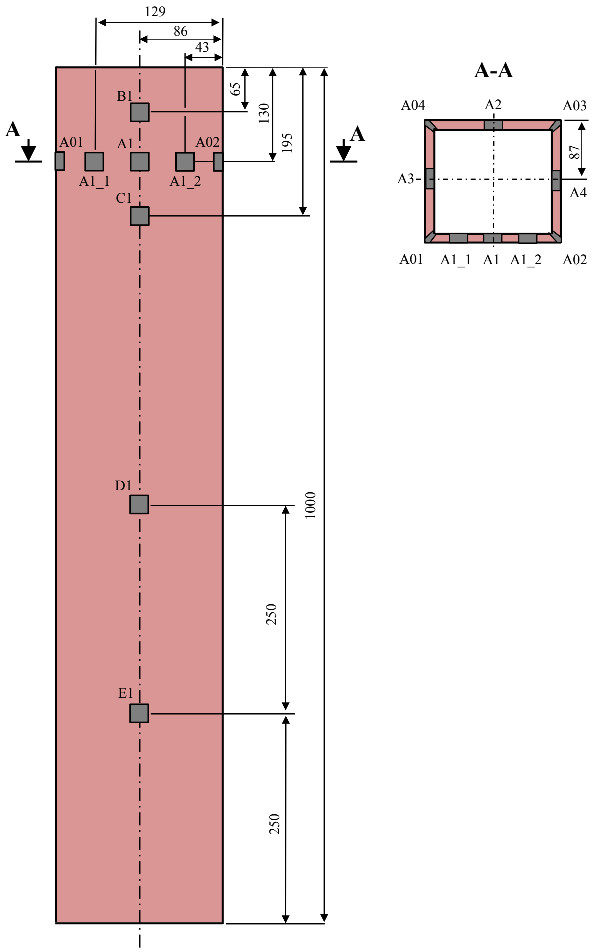

Figure 5.14: Schematic positions of 14 specimens

The mould microstructure has been analysed after application of etching, both on the undamaged and damaged zones. As can be seen in Figure 5.15, many cracks were observed on the following samples A1, A1_1, A1_2, A3, and A4 cut from walls in the level of meniscus where also the maximum temperature occurs. The analysis showed that cracks initiate at the surface and then propagate into thickness. Furthermore, cracks are transgranular confirming that they occurred under effect of thermal fatigue. The microstructure, in some regions near cracks, seemed to have undergone a recrystallization process because of the small grain size (e.g. A1_2, A3). It is observed that cracks appeared near the surface of the mould on the places where Cr-layer is absent. The Cr-layer was delaminated by the differential thermal expansion between the coating and the underneath Ni layer. The grain size of the Cu is coarse and in the range of ~70±30 µm. These dimensions are in the range of the microstructural requirements for this kind of application (i.e. mould used for continuous casting of steel). In particular the requirements are related to creep resistance of material that, in some areas, is working in the range of diffusional creep.

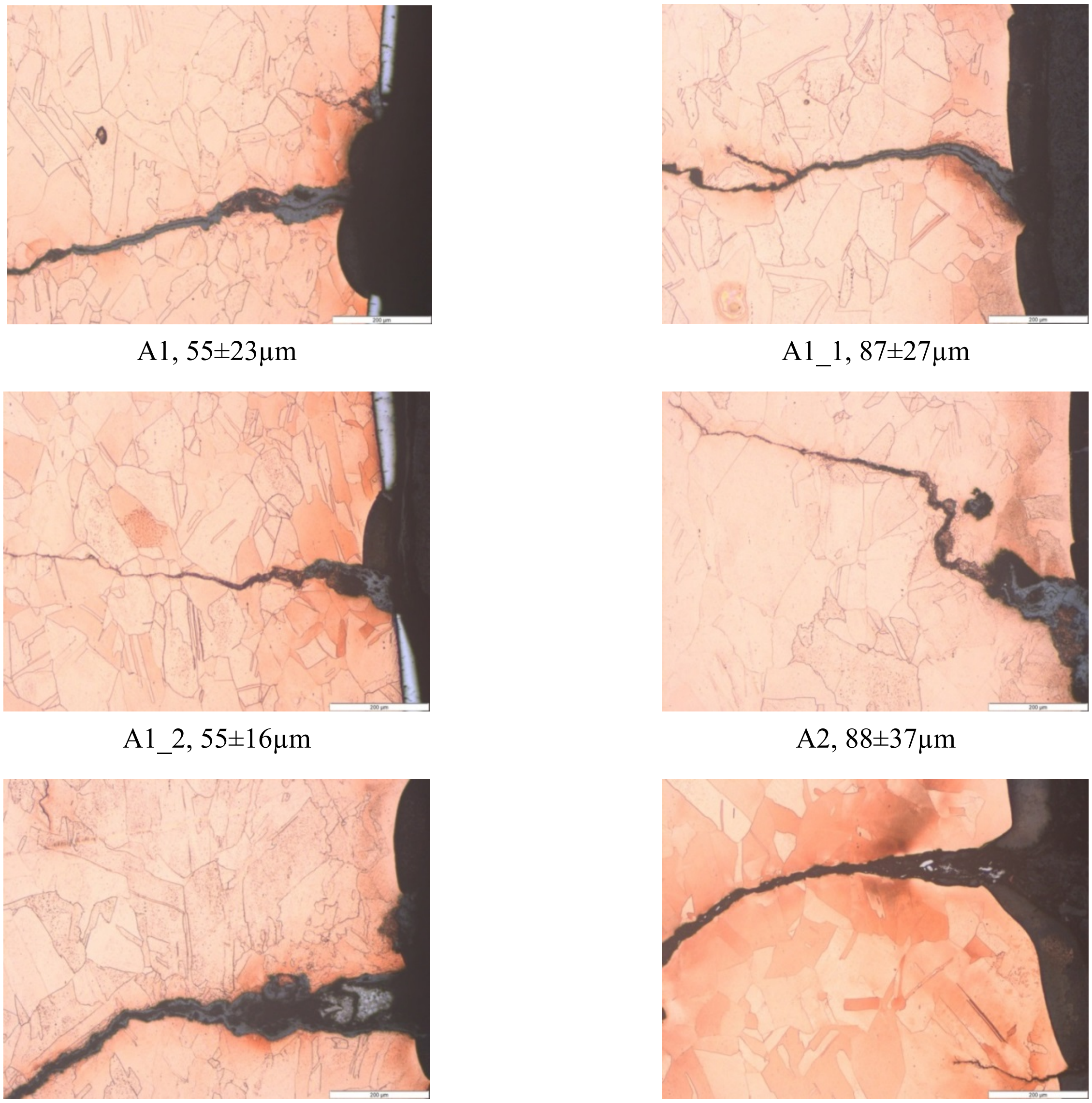

A1, 55±23µm

A1_1, 87±27µm

A1_2, 55±16µm

A2, 88±37µm

A3, 76±24µm

A4, 82±23µm

Figure 5.15: Microstructure of samples taken from walls in the level of meniscus

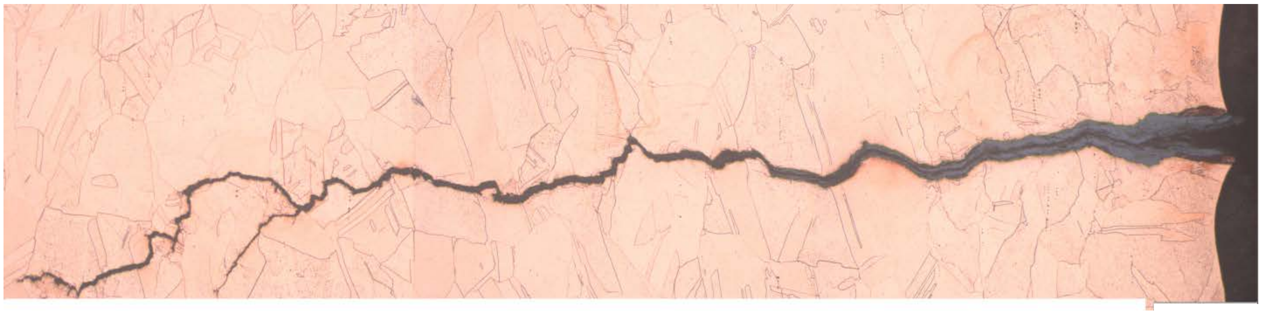
Specimen: A3

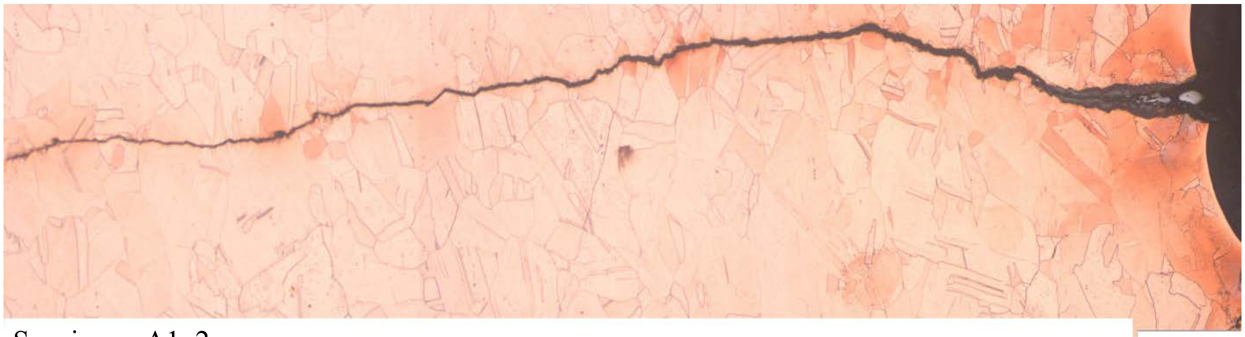
Specimen: A1_2

Figure 5.16: Optical micrograph of the cross section of mould cracks

No visible cracks were found during examination of samples A01 and A02, while samples A03 and A04 have few small cracks, see Figure 5.17.


A01, 50±20µm A02, 87±


A03, 75±25µm A04, 56±24µm

Figure 5.17: Microstructure of samples taken from corners in the meniscus level

The following samples B1, C1, D1 and E1 do not have visible cracks. The chromium coating layer is present on B1, C1, D1 and E1 specimens with thickness of approximately 100 µm.

B1, 94±23µm

C1, 78±26µm

D1, 94±33µm

E1, 91±29µm

Figure 5.18: Microstructure of samples B1, C1, D1 and E1

Inside the cracks were present some deposits that could not be identified by the light microscope analyses. Therefore, the SEM investigation has been performed in order to understand the origin of these deposits. The SEM analysis has been performed on the A1 specimen.

Figure 5.20 and Figure 5.21 show that except zinc many other residual impurities were detected in the crack due to liquid steel infiltration Pb, Zn, S, Mn etc, see Table 5.2. Moreover, Table 5.2 shows chemical composition observed in the undamaged zone (Figure 5.19) where small pits correspond to the region rich of Ag precipitates.

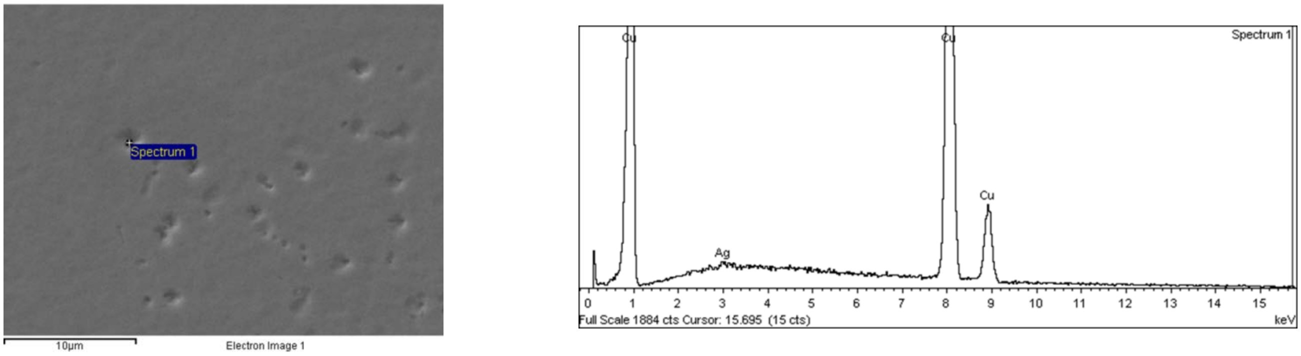

Figure 5.19: X-ray spectrum of the undamaged zone – Spectrum 1

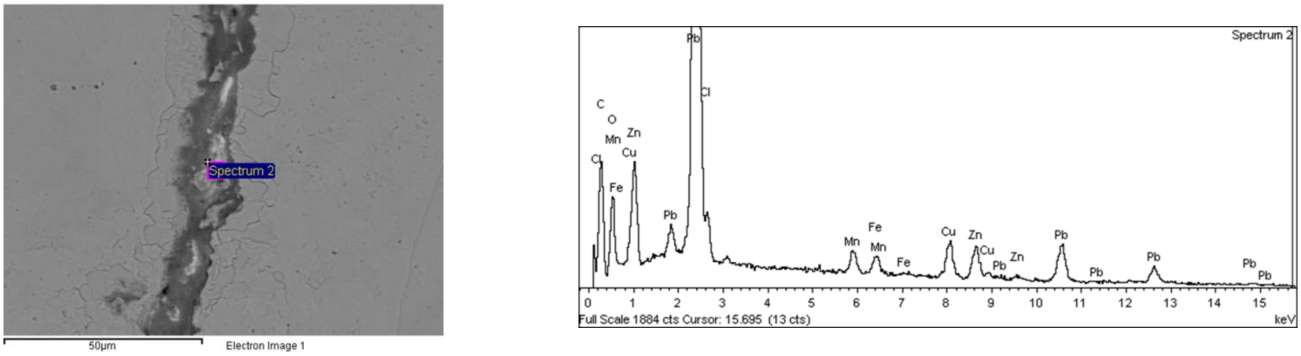

Figure 5.20: X-ray spectrum of the damaged zone (crack) - Spectrum 2

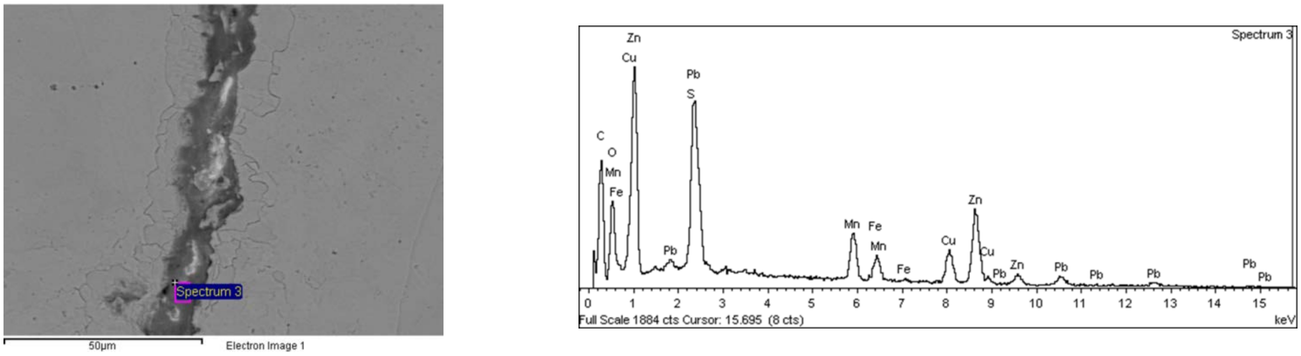

Figure 5.21: X-ray spectrum of the damaged zone (crack) – Spectrum 3

Table 5.2: SEM characterization with respect to Figure 5.19, Figure 5.20 and Figure 5.21

Spectrum	C	O	Ag	S	Cl	Mn	Fe	Cu	Zn	Pb	Total
Spectrum 1			0.55					99.45			100.0
Spectrum 2	24.61	13.84			1.34	1.99	1.67	6.10	7.25	43.21	100.0
Spectrum 3	34.49	15.59		1.97		5.15	2.33	7.08	20.13	13.26	100.0

In particular, it could be seen that the Cu substrate, when it is exposed to the molten steel, is reacting with Zn and producing an alloyed layer that corresponds with a brittle γ phase, see Figure 5.22. This brittle phase is enhancing the production of cracks that are propagating in the underneath Cu substrate. The propagation is enhanced by the permeation of the low melting point of elements (Sn, Pb, Zn etc.) that are embrittling the crack root. In this case the energy required for the crack propagation is lower than the required for the crack propagation in bare Cu.

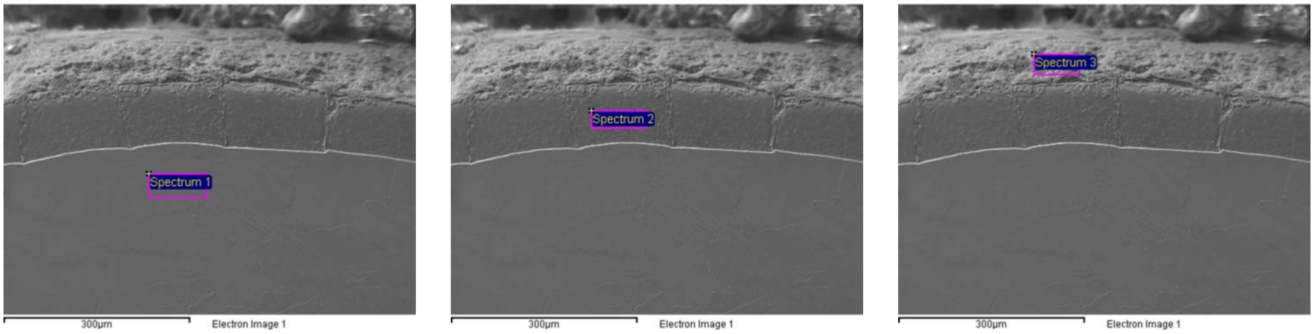

Figure 5.22: SEM investigation of the undamaged zone

Table 5.3: SEM characterization with respect to Figure 5.22

Spectrum	C	O	Si	S	Ca	Mn	Fe	Cu	Zn	Pb	Total
Spectrum 1	3.42	1.01						95.57			100.00
Spectrum 2	14.37	18.01						35.93	31.69		100.00
Spectrum 3	27.97	18.06	0.42	2.14	0.34	5.16	3.74	3.17	29.25	9.76	100.00

Chapter 5 has presented results obtained with the thermo-mechanical analysis where as a study case a copper mould was taken into consideration. The thermo-mechanical analysis have been performed with respect to several material models (the combined model, the linear kinematic, the stabilized and the accelerated model) to investigate influence of a material model on cyclic stress-strain response in a component. Results, i.e. stress-strain responses, obtained with different models will be used as a base to calculate the service life of analysed component in Chapter 6.

Chapter 6

Fatigue life assessment

Fatigue damages which occur due to thermo-mechanical cyclic loads distinguishes from damages occur due to temperature variation [Halford, 1986, Halford, 1987]. Prediction of a thermo-mechanical fatigue life based on thermal fatigue data is not simple. The most accurate way to assess a fatigue life is to establish its behaviour by actual experiment. However, in most cases conducting an extensive experimental test, especially at beginning of research, cannot be performed. Several models have been developed and proposed in [Manson, 1966, Manson, 1967, Manson, 2006], to preliminary assess a fatigue life without involving prior knowledge of fatigue behaviour. Some of these methods are based on monotonic uniaxial test properties of material under investigation. More discussion is given in Chapter 6 regarding these models.

Generally, fatigue in terms of number of cycles is divided into two specified parts; low and high cycle fatigue. Low cycle fatigue (LCF) occurs when during the cyclic loading the plastic deformation is dominant; the strain-life approach is suggested to be used in this situation. High cycle fatigue (HCF) occurs when the stresses are low enough that the strains are elastic. Stress-based approach is suggested to be used in the case of HCF. Strain or stress based approaches allow engineering designer to assess the fatigue life of a component. The strain-based fatigue approaches are considered in Chapter 6.

First few paragraphs of Chapter 6 are focused on strain-based fatigue models (Manson-Coffin-Basquin). Moreover, the particular attention is given to alternative models whose parameters can be estimated using simple tensile test data (Universal Slopes equation, Modified Universal Slopes equation). Identification procedure of the Manson-Coffin-Basquin as well as of alternative models (Universal Slopes equation, Modified Universal Slopes equation) is described afterwards. The experimental data are invariably scattered, since test specimens and testing conditions are never identical. Therefore, statistical methods have been used to analysis the fatigue test data. The last part of Chapter 6 is focused to various models (deterministic and probabilistic) suitable to define design curves. The design curve is established by adopting characteristic value (probability of failure) that lay a certain number of standard deviation below the mean ε-N curve. The last part deals with the fatigue life assessment of a component subjected to thermo-mechanical cyclic loading. For this purpose, the copper mould used in the continuous casting process of steel is considered as an example.

6.1 Stress-based approach

Fatigue started to be investigated in the middle of the nineteenth century when the fatigue failures of railway axes became a widespread problem. The German engineer August Wöhler set up and carried out the first systematic fatigue investigation. August Wöhler investigated the progressive failure of railway axles which had failed after various time in service, at loads considerable less than expected. Wöhler studies resulted in development of the stress-based approach. The stress-based approach is the oldest method used in the fatigue design and it is also referred to as the *S-N* (stress versus number of cycles to failure) approach [Lee, 2005, Stephens, 2001]. The *S-N* approach is distinguished from the other fatigue models by several features: cyclic stresses are the governing parameters for fatigue failure and high-cycle fatigue conditions. To develop the *S-N* diagram, a series of samples are tested at various stress ranges and several samples are tested at each stress range. Generally, *S-N* diagrams are plotted in log-log scale, where the stress amplitude is plotted on the vertical axis and cycles to failure on the horizontal axis, see Figure 6.1. In 1910, Basquin proposed following relationship between stress amplitude and lifetime:

$$\sigma_\mathrm{a} = \sigma_\mathrm{f}'(2N_\mathrm{f})^{b^*} \qquad 6.1$$

where σ_f' is the fatigue strength coefficient, b^* is fatigue strength exponent also known as Basquin exponent and $2N_\mathrm{f}$ is reversals to failure (1 reversal=1/2 cycle). Basquin equation is rewritten in terms of strain based approach in paragraph 6.3. When the stress on a particular region of a material varies sinusoidally from tension to compression and back again is known as fully reversed loading. Fully reversed indicates that loading is alternating about a zero mean stress (σ_m). As can be seen in Figure 6.2, the stress range ($\Delta\sigma$), the stress amplitude (σ_a) and the mean stress are parameters which characterize a cyclic loading and can be expressed as:

$$\Delta\sigma = \sigma_\mathrm{max} - \sigma_\mathrm{min}, \quad \sigma_\mathrm{a} = \frac{\sigma_\mathrm{max} - \sigma_\mathrm{min}}{2}, \quad \sigma_\mathrm{m} = \frac{\sigma_\mathrm{max} + \sigma_\mathrm{min}}{2} \qquad 6.2$$

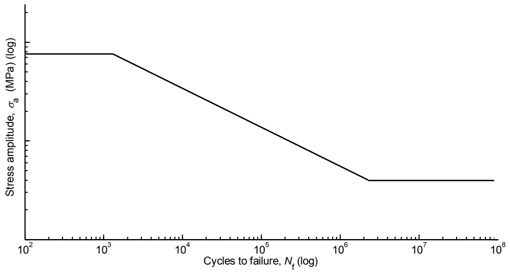

Figure 6.1: *S-N* diagram

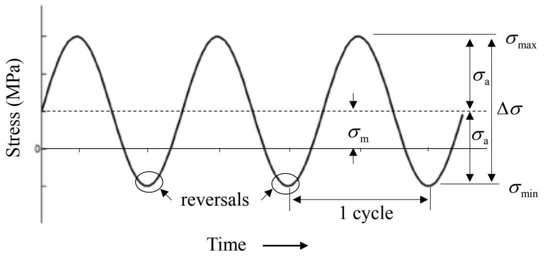

Figure 6.2: Stress versus time

The stress-based approach is not appropriate to be used in situations which involve high stresses, high temperatures or stress concentrations, i.e. in which significant plasticity can be involved. In this kind of situations is more appropriate to use a strain-based approach.

6.2 Strain-based approach

Strain-based approach is used to estimate service life of a component in case of low cycle fatigue. Low-cycle fatigue is relevant for components subjected to small numbers of cycles due to plastic deformations which occur in each cycle [Lee, 2005, Schijve, 2001, Stephens, 2001]. An example for which LCF is important is a pressure vessel which is pressurized a small number of times in many years. Another example is a power generator structure which operates at elevate temperatures consequently significant thermal stresses.

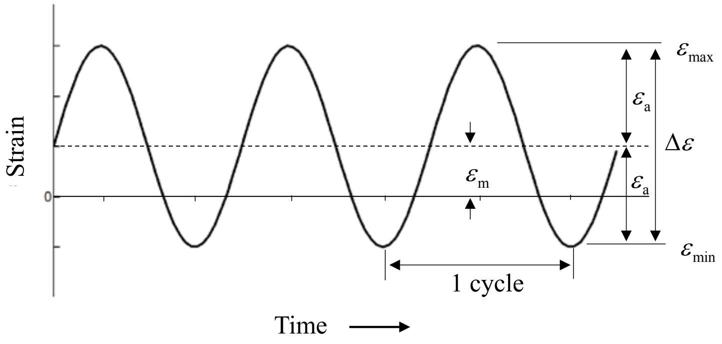

Figure 6.3: Strain versus time

The strain range ($\Delta\varepsilon$) is equal to a difference between the maximum strain (ε_{max}) and the minimum strain (ε_{min}) in a cycle, see Figure 6.3:

$$\Delta\varepsilon = \varepsilon_{\max} - \varepsilon_{\min} \qquad 6.3$$

In situation when maximum and minimum strains are not equal, the mean strain can be presented as:

$$\varepsilon_{\mathrm{m}} = \frac{\varepsilon_{\max} + \varepsilon_{\min}}{2} \qquad 6.4$$

In the mid 1950's, Manson and Coffin were first researchers, working independently, which related the number of cycles to the plastic strain amplitude. Both researchers noted that a linear relationship is obtained when the logarithm of the plastic strain amplitude is plotted against the logarithm of the number of reversals to failure [Manson, 2006]:

$$\frac{\Delta\varepsilon_{\mathrm{pl}}}{2} = \varepsilon_{\mathrm{f}}'\left(2N_{\mathrm{f}}\right)^{c} \qquad 6.5$$

where $\varepsilon_{\mathrm{f}}'$ is the fatigue ductility coefficient and c is the fatigue ductility exponent.

6.3 Strain-life equation for LCF and HCF

Basic relation between the total strain range and the number of reversals to failure is a sum of two power-law terms, one for the plastic and the other for elastic strain [Manson, 2006]:

$$\begin{aligned} \Delta\varepsilon &= \Delta\varepsilon_{\mathrm{el}} + \Delta\varepsilon_{\mathrm{pl}} = \\ &= J(2N_{\mathrm{f}})^{j} + V(2N_{\mathrm{f}})^{v} \end{aligned} \qquad 6.6$$

where J, j and V, v are the coefficient and exponent terms relating to the elastic and the plastic strain range, respectively. The format of equation (6.6) was used in period between 1952 and 1964 after which an alternative notation in term of the total strain amplitude ($\Delta\varepsilon/2$) was introduced by Morrow (1965). Dividing the Basquin equation (6.1) by E, the elastic strain amplitude can be obtained as:

$$\frac{\Delta\varepsilon_{\mathrm{el}}}{2} = \frac{\sigma_{\mathrm{a}}}{E} = \frac{\sigma_{\mathrm{f}}'}{E}\left(2N_{\mathrm{f}}\right)^{b^*} \qquad 6.7$$

Combining the Basquin's equation (6.7) with the Manson-Coffin equation (6.5) finally gives an equation that can be used to estimate the entire range of fatigue live to failure in reversals ($2N_{\mathrm{f}}$):

$$\frac{\Delta\varepsilon}{2} = \frac{\sigma_{\mathrm{f}}'}{E}\left(2N_{\mathrm{f}}\right)^{b^*} + \varepsilon_{\mathrm{f}}'\left(2N_{\mathrm{f}}\right)^{c} \qquad 6.8$$

Equation (6.8) is known as the Manson-Coffin-Basquin fatigue model and it can be also presented graphically. As shown in Figure 6.4, plotting the elastic and plastic relations on log-log coordinates, both curves become straight lines. Superposition of the elastic and the plastic components gives the fatigue life in terms of total strain.

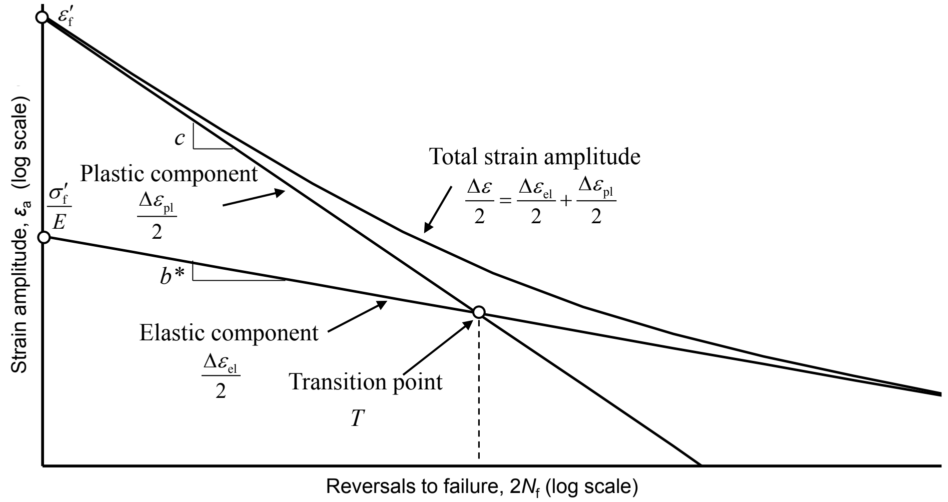

Figure 6.4: Manson-Coffin-Basquin strain life curve

Transition fatigue life (point T in Figure 6.4) is obtained by intersection of the elastic and the plastic strain lines. Transition fatigue life presents the fatigue life at which the elastic strain amplitude and the plastic strain amplitude are equal, see Figure 6.4. Equation for the transition fatigue life ($2N_t$) can be derived by equations (6.5) and (6.7):

$$2N_t = \left(\frac{\varepsilon_f' E}{\sigma_f'}\right)^{1/\left(b^*-c\right)} \tag{6.9}$$

Region in which the plastic deformation is dominant, left of the transition point, is referred to as the low cycle fatigue (LCF) region. The high-cycle fatigue (HCF) region, in which the elastic strain is dominant, is placed right regarding the transition point.

6.4 The Universal Slopes equation

Often fatigue life of a component with a reasonable degree of accuracy is desirable to estimate using some simpler approach. For example, fatigue test data is required to estimate four Manson-Coffin-Basquin parameters. Conduction of fatigue tests can be more time-consuming and expensive in comparison with monotonic tension tests. This leads to development of several methods which correlate monotonic strength and fatigue life. Basic material properties such as the Young's modulus, the ultimate tensile strength and the ductility can be obtained from monotonic tension test. It is important to note that the stress-strain behaviour obtained from tension test can, however, be quite different from one obtained under cyclic loading, because cyclic loading can cause hardening and/or softening of a material.

In 1965, Manson and Hirschberg presented the method of Universal Slopes equations that use only tensile test properties. Elaborating fatigue data obtained for 29 different types of materials, Manson found out that the slopes of the elastic and the plastic lines have same values for all materials. The elastic component has an average slope of -0.12, while the plastic component has an average slope value of -0.6 [Manson, 1965, Manson, 1968, Manson, 2006]. One point on each of these components was determined at the intercept on the strain axis at N_f=1. For the plastic component, it has been found that the intercept point depends only on ductility (D). For the elastic component, the intercept point was found that depends on ultimate tensile strength (σ_{uts}) and the Young's modulus. The total strain range gives as the sum of elastic and plastic components, thus becomes:

$$\Delta\varepsilon_{US} = 3.5\frac{\sigma_{uts}}{E}N_f^{-0.12} + D^{0.6}N_f^{-0.6} \qquad 6.10$$

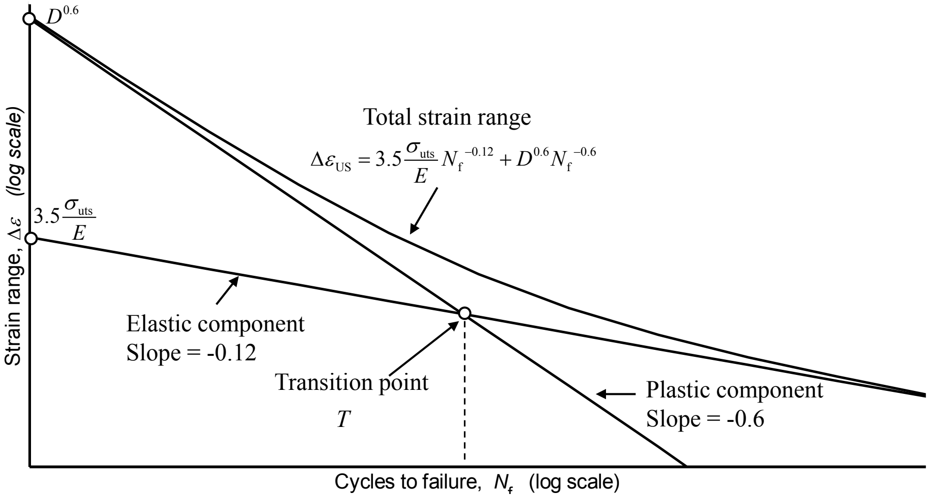

Figure 6.5: The Universal Slopes equation

The method of Universal Slopes equation firstly had been developed for estimating fatigue behaviour at room temperature. Although originally proposed for steel [Manson, 1968], in this work the Universal Slopes equation will be applied to a copper alloy.

6.5 10% and 20% Rule

Next attempt was to apply the Universal Slopes equation using the tensile properties at high temperature of interest. The fatigue life for a given strain range at high temperature may be expected to be lower than that for the same strain range at a temperature below half the melting point. Creep, oxidation and high temperatures are known to reduce up to 90% of fatigue life. A rough estimate is provided by 10% Rule as suggested in [Manson, 1967, Manson, 1968, Manson, 2006, Manson, 2009]. The 10% Rule estimates that, at the high temperatures, only 10% of the life computed by the Universal Slopes equation will actually be achieved. The Universal Slopes equation gives the upper bound life, while the 10% Rule gives the lowest expected life i.e. lower bound life.

Median expected life is estimated to be 2 times of the lowest bound life [Manson, 2009]. The 20% Rule assumes that, at the high temperatures, only 20% of the life computed by the Universal Slopes equation will actually be achieved. Since as suggested [Manson, 1968] an average mean fatigue life has been estimated to be twice of the lower bound (20%).

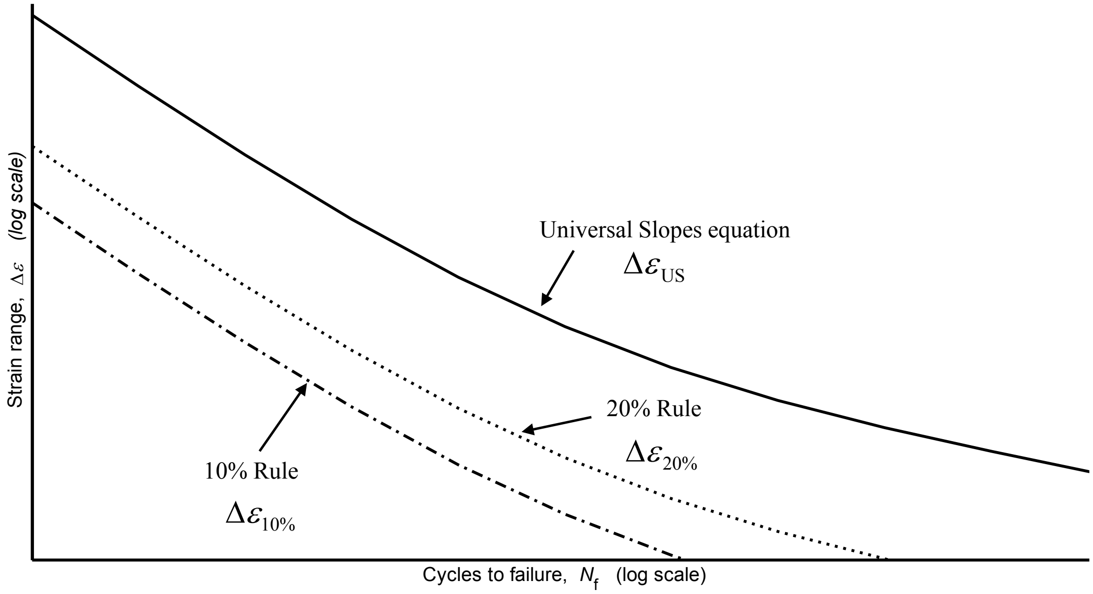

Figure 6.6: 10% and 20% Rule

6.6 The Modified Universal Slopes equation

In 1986, Muralidharan and Manson conducted a study on 50 different materials with the intention to re-exanimate and to improve the Universal Slopes equation accuracy. The Universal Slopes equation (6.10) was further modified to the following expression [Manson, 2006, Pope, 1997]:

$$\Delta\varepsilon_{\mathrm{MUS}} = 1.17\left(\frac{\sigma_{\mathrm{uts}}}{E}\right)^{0.832} N_{\mathrm{f}}^{-0.09} + 0.0266 D^{0.155}\left(\frac{\sigma_{\mathrm{uts}}}{E}\right)^{-0.53} N_{\mathrm{f}}^{-0.56} \qquad 6.11$$

In the first term, representing the elastic component, slope has become -0.09 instead of -0.12. Lower value (-0.09) contributes that the elastic line calculated by equation (6.11) is shifted above regarding the elastic line calculated by equation (6.10), see Figure 6.7. In the second term, representing the plastic component, new exponent -0.56 differs little from the original value of -0.6; but instead of involving only a ductility term, the new equation contains both the strength term [$\approx(\sigma_{\mathrm{uts}}/E)^{1/2}$] and the ductility term with a considerable lower exponent [Manson, 2006]. As can be seen in Figure 6.7, the plastic line calculated by equation (6.11) is shifted above the plastic line calculated by equation (6.10). Finally, the curve $\Delta\varepsilon_{\mathrm{MUS}}$, which is the sum of the elastic and plastic components, is thus displaced slightly upward regarding Universal Slopes Equation obtained with parameters from tensile test data at 250 °C. The displacement is the greatest in the region of HCF where the elastic component predominates. The equation (6.11) should be used only in the sub-creep temperature range (up to about half of the absolute melting temperature of a material). Furthermore, the ductility and the ultimate strength used in equation should be estimated at a temperature for which the fatigue life is calculated [Edward, 1997].

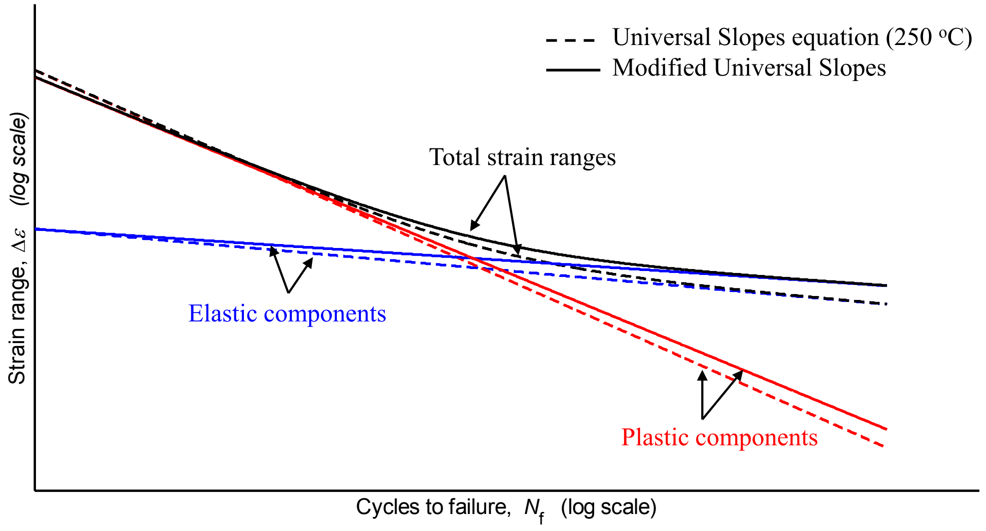

Figure 6.7: Comparison between Universal Slopes and Modified Universal Slopes equations

6.7 Statistical aspects of fatigue

Generally, fatigue experimental data are subjected to considerable scatter. Statistical analyses are used to describe and to analyse fatigue properties as well as to determine the probability associated with fatigue life of a component. Some basic concepts commonly adopted for the statistic characterization of fatigue data is given hereafter. Figure 6.8 illustrates the statistical scatter typical for fatigue data. Plenty of factors contribute to scatter:

- production and surface quality of a specimen,
- accuracy of test equipment as well as skill of laboratory technicians,
- environment in a laboratory (controlled temperature and humidity) etc.

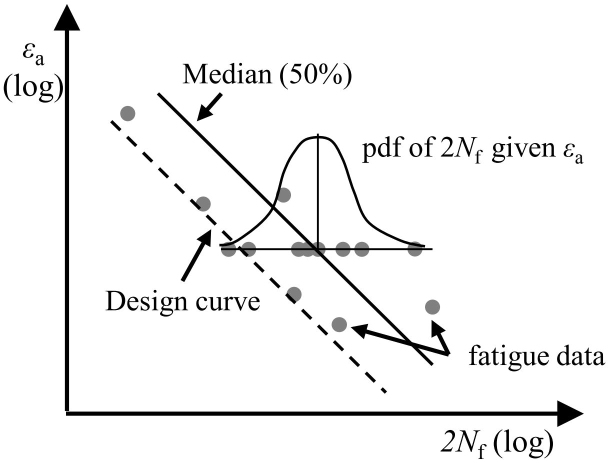

Figure 6.8: Schematically description of a strain-based fatigue curve

A quantity such as the fatigue data has a statistical variation called ″stochastic variable″, *X*. Characteristics of a variable for a population are usually obtained from a small part of the population, called a sample [Stephens, 2001]. The mean or average for a sample size *n* is defined as:

$$\overline{X} = \frac{1}{n}\sum_{i=1}^{n} X_i \tag{6.12}$$

Here, X_i denotes a random variable such as the plastic strain amplitude in the strain-life fatigue test. The mean value gives a measure of the central value of the sample. Dispersion of values in the sample is measured by the sample standard deviation [Stephens, 2001]:

$$S = \sqrt{\frac{\sum_{i=1}^{n}\left(X_i - \overline{X}\right)^2}{(n-1)}} \tag{6.13}$$

Standard deviation gives a measure of the magnitude of the variation. Parameter which is widely used to describe the uncertainty is the coefficient of variation, C, which is given by:

$$C = \frac{S}{\overline{X}} \qquad 6.14$$

Fatigue data have significant scatter which can be described by the probability density function (pdf) as shown in Figure 6.8. Generally, statistical models are employed to describe the distribution of the observed factor. For instance, the random variable N_f is usually described with 2-parameter Weibull or normal model.

6.7.1 Linear model

The scatter diagram, presented in Figure 6.9, shows the plastic strain amplitude versus the number of reversal to failure plotted on a log-log diagram. It can be noticed that there is a strong indication that points (e.g. experimental data) lie scattered randomly around a straight line.

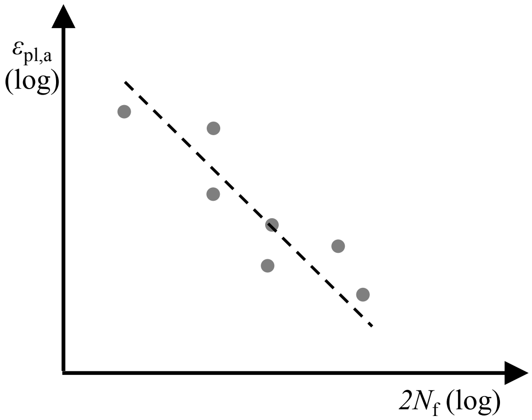

Figure 6.9: Scatter diagram of a fatigue data

Identification of a straight line can be done by adopting a simple linear model [Martinez, 2002, Marques, 2007, Montgomery, 2003, Stephens, 2001]:

$$Y = A + BX \qquad 6.15$$

in which X is a single independent or controlled variable and Y is a dependent variable, the relation is usually denoted as $Y|X$. In case of Manson-Coffin equation (6.5), $Y=\log(\varepsilon_{pl,a})$ and $X=\log(2N_f)$. The intercept (A) and slope (B) are unknown regression coefficients. More appropriate way to solve this problem takes into consideration also the normal distributed random variable error, ε:

$$Y = A + BX + \varepsilon \qquad 6.16$$

where the error has mean zero and variance S^2 which is unknown. Taking into account the error variability, Y is also a random variable. Using equation (6.16), it is possible to express the n observations in the sample as:

$$Y_i = A + BX_i + \varepsilon_i\,, \qquad i=1, 2,\ldots,\mathrm{n} \tag{6.17}$$

The least squares estimates of the slope and intercept in the simple linear regression model are:

$$\hat{B} = \frac{\sum_{i=1}^{n}\left(X_i - \overline{X}\right)\left(Y_i - \overline{Y}\right)}{\sum_{i=1}^{n}\left(X_i - \overline{X}\right)^2} \tag{6.18}$$

$$\hat{A} = \overline{Y} - \hat{B}\overline{X} \tag{6.19}$$

where $\hat{A}$, $\hat{B}$ are least squares estimators and $\overline{X}$, $\overline{Y}$ are the average values of X and Y:

$$\overline{Y} = \frac{1}{n}\sum_{i=1}^{n} Y_i\,, \quad \overline{X} = \frac{1}{n}\sum_{i=1}^{n} X_i \tag{6.20}$$

The fitted or estimated regression line has the following form:

$$\hat{Y} = \hat{A} + \hat{B}X \tag{6.21}$$

Noting that each pair of observations satisfies the relationship:

$$Y_i = \hat{A} + \hat{B}X_i + \mathrm{e}_i\,, \qquad i=1,2\ldots,n \tag{6.22}$$

where e_i is the residual expressed as:

$$\mathrm{e}_i = Y_i - \hat{Y}_i \tag{6.23}$$

The residuals describe the error in the fit of the model to the i^{th} observation Y_i. The sum of squared errors is defined as:

$$SSE = \sum_{i=1}^{n} \mathrm{e}_i^2 = \sum_{i=1}^{n} (Y_i - \hat{Y}_i)^2 \tag{6.24}$$

The sum of squares due to regression is expressed as:

$$SSR = \sum_{i=1}^{n} (\hat{Y}_i - \overline{Y}_i)^2 \tag{6.25}$$

While the total sum of squares is:

$$SST = \sum_{i=1}^{n} (Y_i - \overline{Y}_i)^2 \tag{6.26}$$

R-squared (R^2) is the statistic measure which shows how close the data are to the fitter regression line, it is also known as the coefficient of determination.

$$R^2 = \frac{SSR}{SST} = 1 - \frac{SSE}{SST} \tag{6.27}$$

In general, R^2 is always between 0 and 1.0. The higher the R^2 is, the model better fits to the data. In the Chapter 4, the *SSE* as well as R^2 have been used to provide information about adequacy of the fitted model.

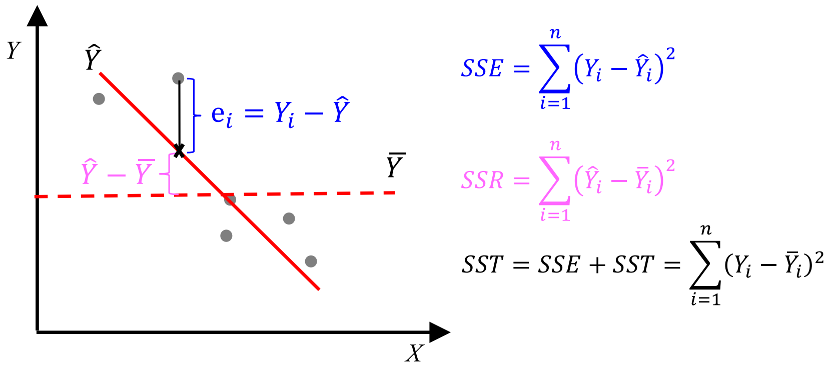

Figure 6.10: Schematically representation of *SSE*, *SSR* and *SST*

6.8 Identification procedure of fatigue life parameters

The identification procedure of Manson-Coffin-Basquin parameters is described in this paragraph. Parameters are estimated using low cycle fatigue experimental data of a CuAg alloy at three temperature levels (20 °C, 250 °C and 300 °C). Afterwards, three main parameters that define the Universal Slopes equation and Modified Universal Slopes equation are estimated using tensile test data of a CuAg alloy performed at 20 °C, 250 °C and 300 °C.

6.8.1 Manson-Coffin-Basquin parameters

Several low cycle fatigue tests with a load ration R_ε=-1 at different strain ranges are necessary to perform to identify four Manson-Coffin-Basquin parameters. In general, fatigue tests are expensive, time-consuming and therefore often large sizes of samples are not possible. Sufficient numbers of specimens are important to test in order to obtain statistical meaningful results due to a considerable amount of scattering which appears in fatigue test data. Parameters uncertainty is relatively large in case of small number of samples.

Four Manson-Coffin-Basquin parameters are estimated separately by performing linear regression analysis [Nieslony, 2008]. The estimated parameters are valid in the range of the experimental data. Linearization of the Manson-Coffin equation (6.5) leads to:

$$Y = \log(\varepsilon_{\mathrm{f}}') + cX \qquad 6.28$$

where

$$Y = \log\left(\varepsilon_{\mathrm{pl,a}}\right), \qquad X = \log\left(2N_{\mathrm{f}}\right) \qquad 6.29$$

the fatigue ductility parameter ($\varepsilon_{\mathrm{f}}'$) and the ductility exponent, (c), are the intercept and the slope, respectively, of the linear least square fit to the plastic strain amplitude versus the reversals to failure, using a log-log scale. Next step is to apply the least-squares method using equations 6.13, 6.18 and 6.19 to estimate S, $\hat{A}$ and $\hat{B}$, respectively. Once all values are calculated, the Manson-Coffin parameters could be estimated with following relations:

$$\hat{c} = \frac{1}{\hat{B}} \qquad \hat{\varepsilon}_{\mathrm{f}}' = 10^{-\hat{A}\hat{c}}$$

Linearization of Basquin's equation (6.1) gives:

$$Y = \log\left(\frac{\sigma_{\mathrm{f}}'}{E}\right) + b^{*}X \qquad 6.30$$

where

$$Y = \log\left(\varepsilon_{\mathrm{el,a}}\right), \qquad X = \log\left(2N_{\mathrm{f}}\right) \qquad 6.31$$

Similarly, the fatigue strength coefficient (σ_{f}') and the fatigue strength exponent (b^{*}) are the intercept and slope, respectively, of the linear least squares fit to the elastic strain amplitude versus reversals to failure, using a log-log scale. Finally, the Basquin parameters are obtained also by applying the least squares method and using the following relations:

$$\hat{b}^{*} = \frac{1}{\hat{B}} \qquad \frac{\hat{\sigma}_{\mathrm{f}}'}{\mathrm{E}} = 10^{-\hat{A}\hat{b}^{*}}$$

Figure 6.11 shows calculated strain life curve regarding LCF experimental data for CuAg alloy performed at 20 °C.

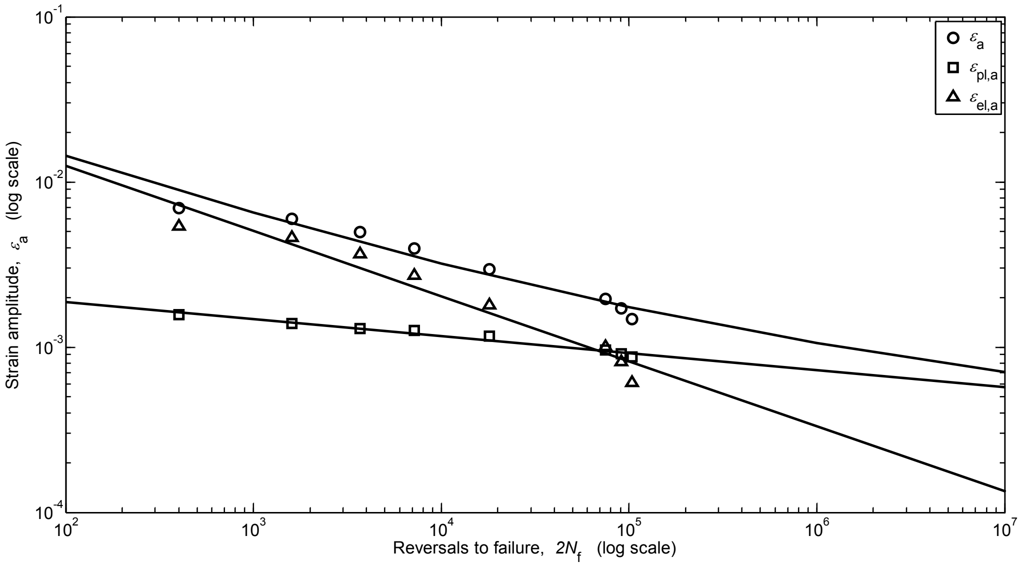

Figure 6.11: Strain-life curves of CuAg for T=20 °C

Manson-Coffin-Basquin parameters (σ_f', b^*, ε_f', c) have been estimated with the least-squares method explained earlier and considering LCF tests of CuAg alloy at three temperature levels (20 °C, 250 °C and 300 °C). The parameters are summarized in Table 6.1. Experimental data of 8 specimens were available for test performed at 20 °C, while 7 specimens were tested at 250 °C and 300 °C.

Figure 6.12 and Figure 6.13 show calculated strain life curves with respect to LCF data of CuAg alloy at 250 °C and 300 °C, respectively. The parameters determined with the least-squares method are valid in the range of the experimental data [Lee, 2005].

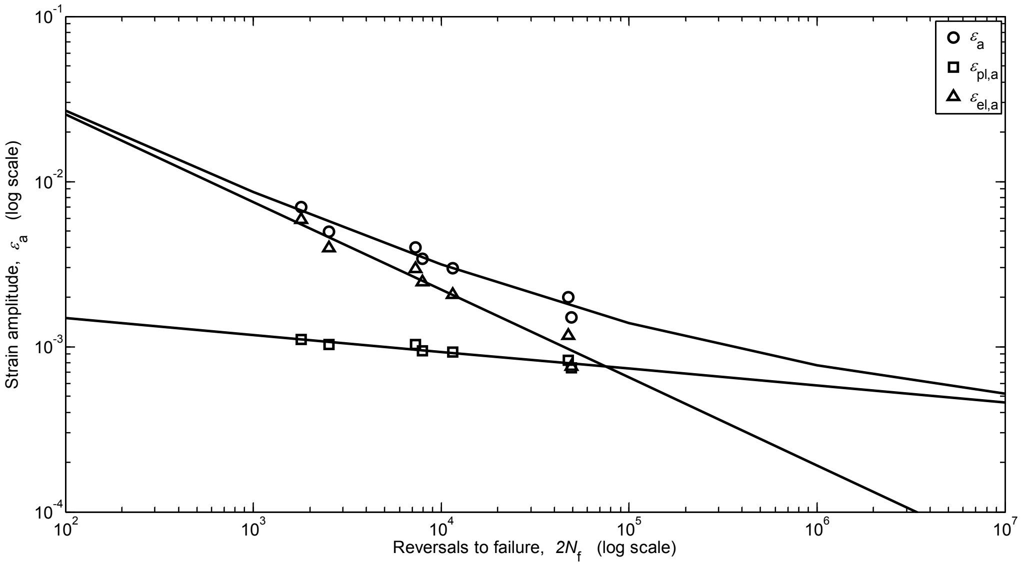

Figure 6.12: Strain-life curves of CuAg for T=250 °C

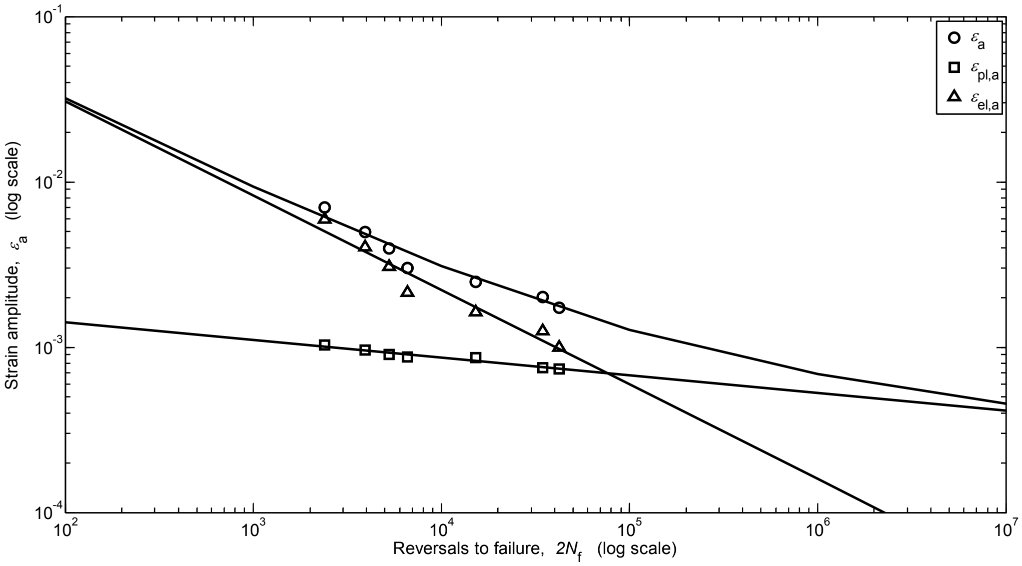

Figure 6.13: Strain-life curves of CuAg for T=300 °C

Determined Manson-Coffin-Basquin parameters are summarized in Table 6.1 with respect to temperature at which tests have been performed.

Table 6.1: Estimated parameters for Manson-Coffin-Basquin method

Temperature (°C)	σ_f' (MPa)	b^*	ε_f'	c
20	359.1	-0.1065	0.09485	-0.4167
250	253.6	-0.1133	0.3666	-0.5551
300	240.4	-0.1125	0.5747	-0.6035

Comparison between strain-life curves calculated with respect to CuAg alloy at different temperatures is presented in Figure 6.14. As can be seen in Figure 6.14, the total strain-life curve for 20 °C is situated below the total strain-life curves for 250 °C and 300 °C in the region $2N_f<10^4$. While situation is opposite in the region $2N_f>10^4$, where the total strain curve for 20 °C is situated above the curves for 250 °C and 300 °C, consequently predicting the highest life for strain amplitudes below ε_a=0.003.

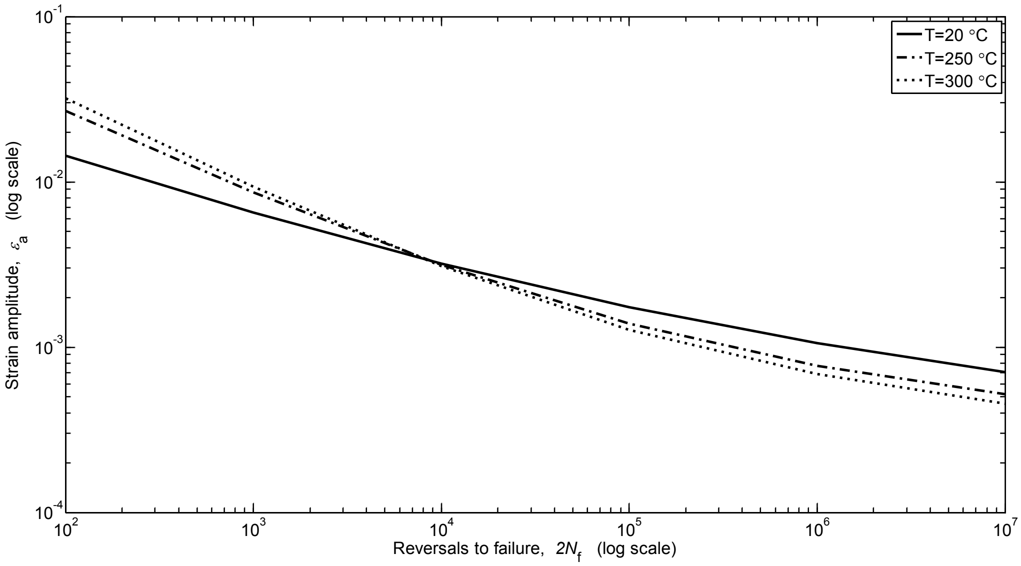

Figure 6.14: Temperature dependence of total strain-life curves

6.8.2 Universal Slopes parameters

Both Universal Slopes and Modified Universal Slopes equations are based on the ultimate strength and ductility that can be determined from a tensile test. All necessary parameters (the ultimate strength, reduction in area and ductility) are estimated from the tensile test data of CuAg alloy performed at 20°C, 250°C and 300°C. The reduction in area (%*RA*) is calculated using equation (2.7), where the initial cross-section area and the area at fracture of each specimen is needed to measure. Ductility is calculated with equation (2.8). Obtained parameters are listed in Table 6.2.

Table 6.2: Material parameters for Universal Slopes and Modified Universal Slopes equations

Temperature (°C)	σ_{uts} (MPa)	%*RA*	*D*
20	234	78.5	1.54
250	168	64.7	1.04
300	158	64.6	1.03

6.9 Design curves

A strain-life curve obtained using the least squares method represents median i.e. curve with 50% probability of failure. Design curves that incorporate the safety factor to be on the safe side during the designing process are important take into consideration. Design curves are constructed to ensure that a major of the fatigue data falls above the minimum or lower bound value. The choice of the lower bound strain-life curve depends upon material cost, safety policy and industrial standards. Two possible approaches (i.e. a deterministic and a probabilistic approach) exist to incorporate fatigue experimental data into a design procedure. [Schneider, 2003, Williams, 2003]

6.9.1 Deterministic approach

The deterministic approach considers only scatter of a material which can be described with the variance (S^2) and calculated using equation (6.13). At the same time neglecting the fact that parameters estimated using least squares method are random variables.

The deterministic approach assumes that a design curve is established on the safe side of data. It is possible to establish a curve below which only 10% of the points would be expected to fall by considering that $Y|X$ is normal with standard deviation of S. Let β denote a probability of Y (or N) being less than the design curve for any X. The standard normal variable associated with β is denoted as z_β. The design curve can be calculated using following expression:

$$\log 2N_{\mathrm{D}} = \hat{Y} - z_{1-\beta} S \qquad 6.32$$

where $2N_{\mathrm{D}}$ is the number of reversals to failure with a probability β. Obtained design curve is transferred to the left for a value $z_\beta S$ in regard to the curve calculated by the least squares method as can be seen in Figure 6.15. Figure 6.15 shows comparison between two different approaches (the least squares method vs. deterministic approach with a probability β=10%) considering fatigue data for CuAg alloy at 20 °C. Figure 6.15 shows elastic, plastic and total strain amplitude versus number of reversals to failure plotted on different graphs due to better overview.

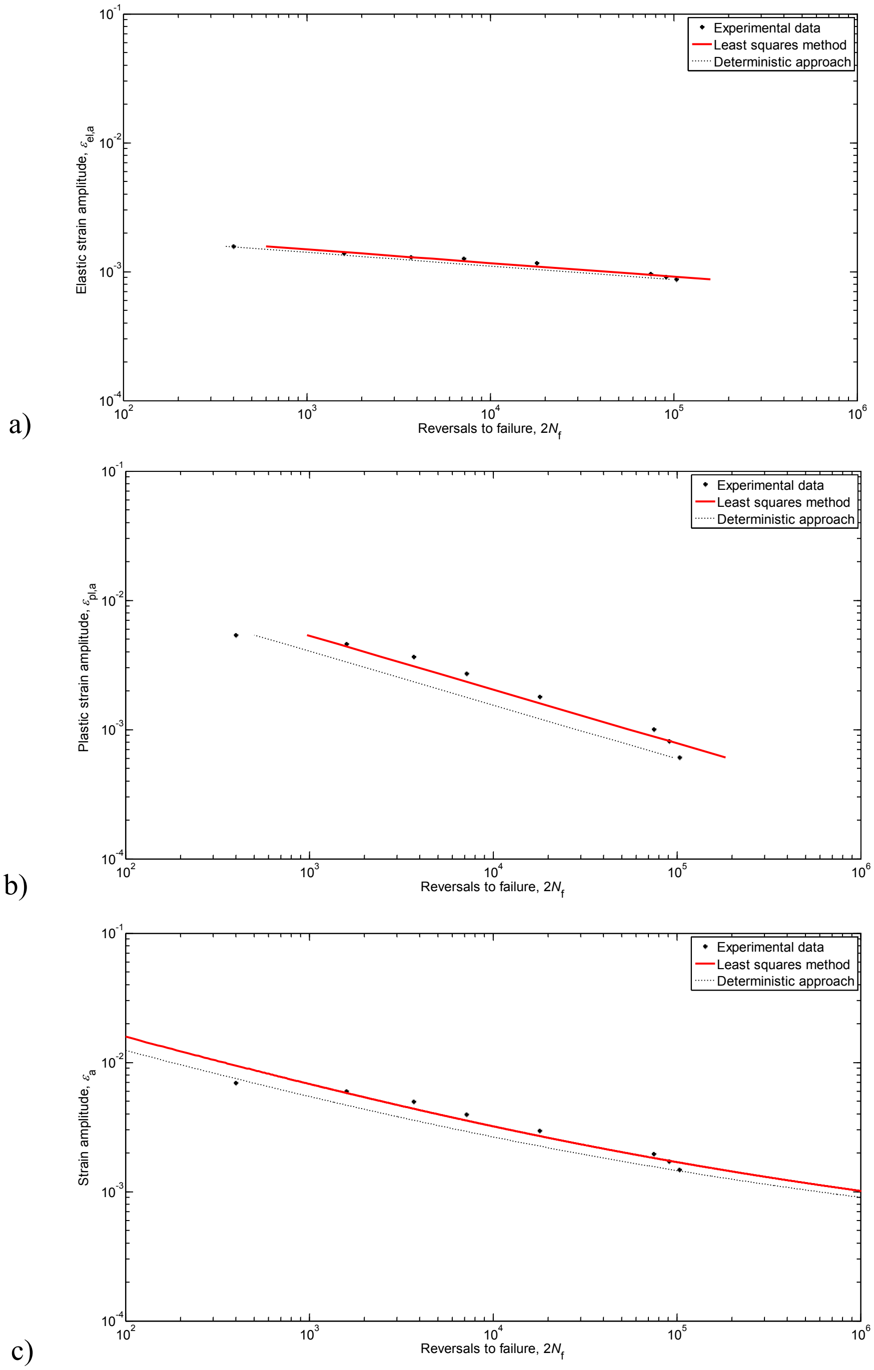

Figure 6.15: Least squares method vs. deterministic approach

The deterministic approach for small number of tested specimens is unconservative [Wirsching, 1980]. Since this method neglects the fact that parameters estimated using least squares method are random variables, it is not suitable for assessing fatigue life. Therefore, the probabilistic methods are presented in the following.

6.9.2 Probabilistic approach

In contrast to deterministic approach, the probabilistic approach assumes that the randomness is present. Therefore, variables are not described by unique values, but rather by probability distribution. Three different probabilistic methods can be used to identify design curves. All three methods are applied on material parameters estimated considering CuAg material and using the least squares method.

6.9.2.1 Tolerance interval method

Application of the tolerance interval method gives a more conservative design curve. Generally, statistical variations ($\bar{X}$ and S) are calculated from a random sample size n, which often represent a small part of a population. Advantage of this method is that it explicitly allows for uncertainty in estimates of population statistic (e.g. standard deviation) from a small sample. Defining a confidence level (δ) provides a quantitative measure of uncertainty. The one-side tolerance limit factor ($K_{\beta,\delta}$) based on a probability of survival (β) with a confidence level (δ) and for a sample size (n) is possible to determine from Table 6.3 [Montgomery, 2003, Stephens, 2001]. The tolerance interval at any strain level lies to the left of the least squares line Y with a distant of $K_{\beta,\delta}S$ [Wirsching, 1980]. The design curve can be calculated by:

$$\log 2N_{\mathrm{T}} = \hat{Y} - K_{\beta,\delta} S \tag{6.33}$$

Table 6.3: One-side tolerance limits assuming normal distribution [Stephens, 2001]

		δ =50%			δ =90%			δ =95%		
n	β	90%	99%	99.9%	90%	99%	99.9%	90%	99%	99.9%
4		1.42	2.60	3.46	3.19	5.44	7.13	4.16	7.04	9.21
6		1.36	2.48	3.30	2.49	4.24	5.56	3.01	5.06	6.61
8		1.34	2.44	3.24	2.22	3.78	4.95	2.58	4.35	5.69
10		1.32	2.41	3.21	2.07	3.53	4.01	2.35	3.98	5.20
20		1.30	2.37	3.14	1.77	3.05	3.60	1.93	3.30	4.32
50					1.56	2.73	3.44	1.65	2.86	3.77
100					1.47	2.60	3.24	1.53	2.68	3.54
500					1.36	2.44	3.09	1.39	2.48	3.28

Figure 6.16 shows design curves calculated with the tolerance interval for low cycle fatigue data for CuAg alloy at 20 °C. The elastic, plastic and total strain amplitude versus number of reversals are plotted individually due to better overview. The design curves are created considering β=90% and δ=90% (i.e.

assuming 10% probability of failure) and 8 number of tested specimens. Based on this assumption $K_{\beta,\delta}$=2.22, taken from Table 6.3. Table 6.3 lists the values of the one-side factor based on normal distribution for various sample sizes, confidence levels and probability of survival.

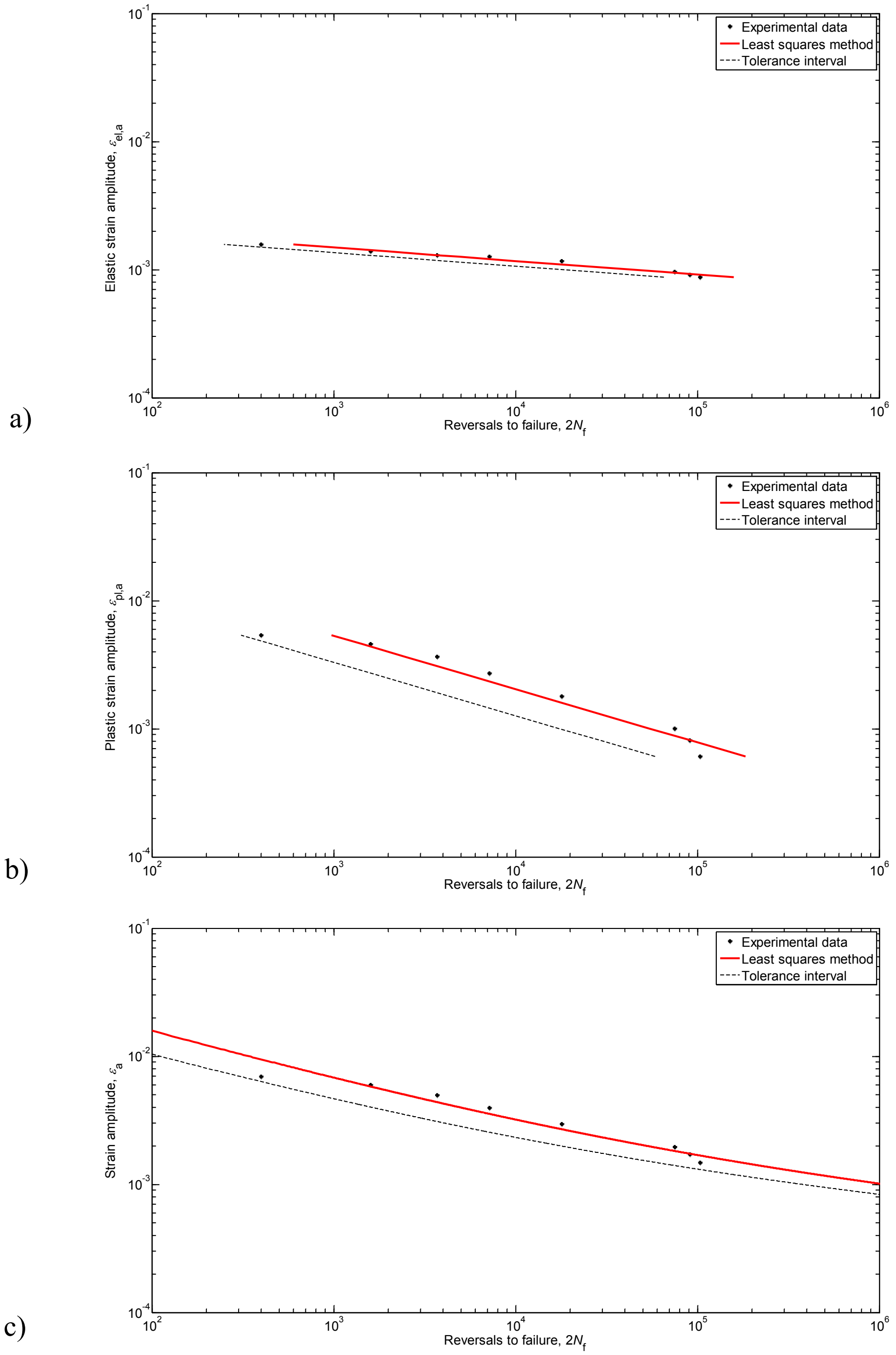

Figure 6.16: Least squares method vs. design curve - tolerance interval

6.9.2.2 Student's distribution - t

The Student's distribution is suggested to use in order to calculate the variability of experimental data for small number of samples; even if phenomenon can be described with normal distribution. Student's distribution is symmetric [Montgomery, 2003]. The design curve can be defined considering the probability of failure β and Student's distribution with n-2 degrees of freedom by equation:

$$\log 2N_\mathrm{S} = \hat{Y} - t_{1-\beta;n-2} S \sqrt{\frac{1+n}{n} + \frac{\left(X-\overline{X}\right)^2}{nS_\mathrm{X}^2}} \tag{6.34}$$

where $2N_\mathrm{S}$ is number of reversal with a probability of failure β, t is the Student's variate and can be find in the statistical tables of a Student's distribution. While

$$S_\mathrm{X}^2 = \frac{1}{n}\sum_{i=1}^{n}\left(X-\overline{X}\right)^2 \tag{6.35}$$

Figure 6.17 shows comparison between design curves obtained with three different methods. Both curves, (Student's and deterministic) are calculated with the probability of failure 10%. As can be seen, the design curve obtained with the Student's distribution is the most conservative while the curve calculated with deterministic approach is less conservative. Moreover, the Student's curve is not a straight line but it is slightly curved. Only the plastic strain range versus the number of reversals is plotted. However, plotting the elastic or the total strain versus the number of reversals gives the same results. The Student's curve can be interpreted as follows: on the basis of the available data, there is a 10% chance that the next *Y*\|*X* selected would fall below this curve.

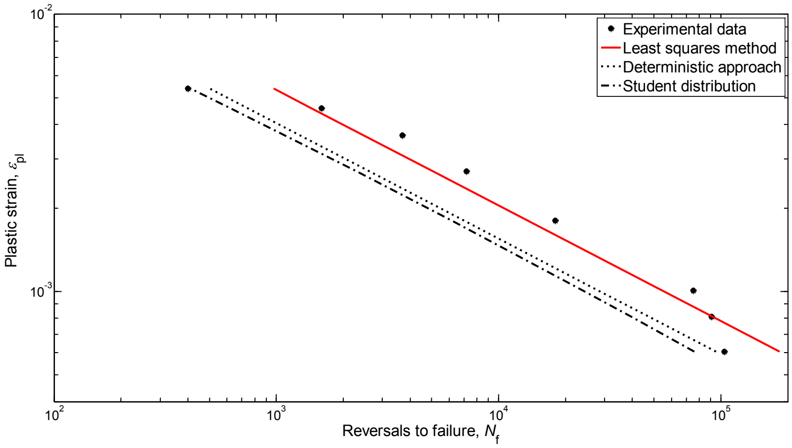

Figure 6.17: Least squares method vs. design curve - tolerance interval and Student's distribution

Analysing the equation (6.34) can be demonstrated that for large number of samples ($n \rightarrow \infty$) it is obtained that $t_{1-\beta;n-2} \rightarrow z_{1-\beta}$ and the radical term tends to 1. Therefore for a large n, equation (6.34) approaches equation (6.32), i.e. Student's distribution tends to the normal distribution.

6.9.2.3 Equivalent prediction interval (EPI)

The equivalent prediction interval (EPI) approach is based on linearization of a curve calculated by the Student's distribution. It is assumed that $Y\backslash X$ has a normal distribution with mean to model the uncertainty in Y [Wirsching, 1983]:

$$\hat{Y} = \hat{A} + \hat{B}X$$

and equivalent standard deviation, S_e. where combination of equation (6.32) and equation (6.34) gives S_e. Moreover, S has been replaced with S_e considering the equation (6.32). It is obtained:

$$z_{1-\beta} S_{\mathrm{e}} = S\left(t_{1-\beta;n-2} \sqrt{\frac{1+n}{n} + \frac{\left(X - \overline{X}\right)^2}{n S_{\mathrm{X}}^2}} \right) \qquad 6.36$$

Probabilities associated with the normal and Student's are assumed to be equal. As they are two different models, equality can exist only at one point β. Finally based on equality, the equivalent standard deviation is defined as:

$$S_{\mathrm{e}} \equiv S_{\mathrm{e}}(X, n, \beta) = S\left[\frac{t_{1-\beta;n-2}}{z_{1-\beta}} \sqrt{\frac{1+n}{n} + \frac{\left(X - \overline{X}\right)^2}{n S_X^2}} \right] \qquad 6.37$$

The equivalent standard deviation, defined in the equation (6.37), seems to be quite complicate for an engineering scope. Furthermore, S_e does not assume a constant value as it depends on X, n as well as on β. However, the standard deviation should be a constant value. This problem can be fixed introducing a new term. As it has been already explained, the design curve calculated by the Student's distribution becomes flat as number of samples is equal or higher than 15 ($n \geq 15$) [Wirsching, 1980]. This characteristic gives a possibility of simplifying the model by introducing an equivalent and constant standard deviation, S_o. The equivalent constant standard deviation gives ability that these probability design curves can be approximated as straight lines. Obtained lines are called herein as equivalent prediction intervals or abbreviated EPI. The equivalent constant standard deviation of Y is defined as [Wirsching, 1980]:

$$S_{\mathrm{o}} = S g(n, \beta) \qquad 6.38$$

where $g(n, \beta)$ is an approximation to the terms in brackets in equation (6.37) and also an adjustment factor of the S which takes into consideration uncertainty in the estimates of $\hat{A}$, $\hat{B}$ and S. The adjustment factor is applied to standard deviation previously calculated with linear regression and it can be calculated as:

$$g(n,\beta) = \exp\left[A(\beta)(\ln n)^{-B(\beta)} \right] \qquad 6.39$$

in which:

$$\begin{aligned} A(\beta) &= 1.56\left[\tanh^{-1}(1-\beta)\right]^{1.12} \\ B(\beta) &= 3.32 - 1.7\beta \end{aligned} \qquad 6.40$$

The equivalent constant standard deviation (S_o) is recommended to use within following limits:

$$6 \le n \le 50;\ 0.01 \le \beta \le 0.15$$

The adjustment factor (g) tends to 1 as $n \to \infty$, because the Student's distribution for large enough number of specimens tends to normal distribution, therefore also S_o tend to the S.

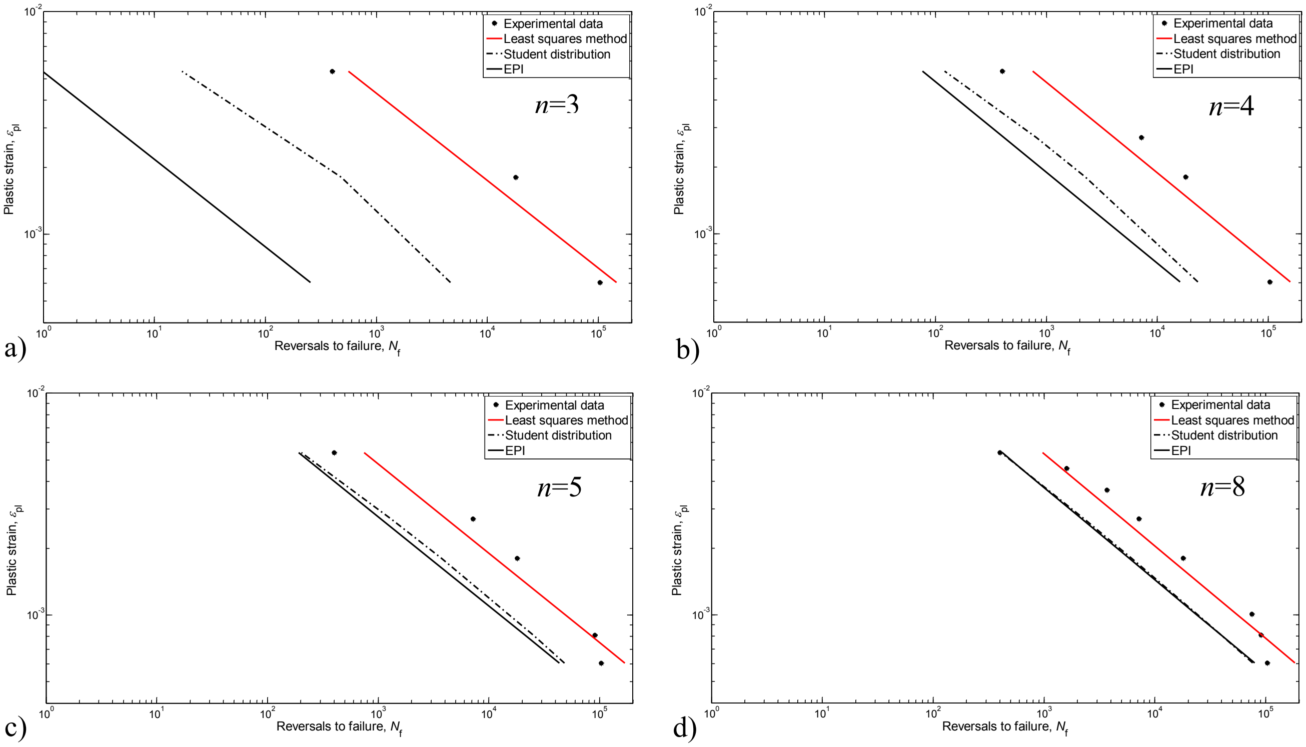

Figure 6.18: Design curves: Student's vs. EPI approach

Figure 6.18 shows comparison between design curves obtained with Student's and EPI for various number of tested samples. As can be seen in Figure 6.18, for $n \le 6$ there is no agreement between two curves obtained with Student's and EPI methods, respectively. On the other hand, the curve calculated with EPI approach becomes a good approximation of the Student's curve when $n > 6$, see Figure 6.18 d; i.e. obtained curves overlap each other. The EPI curve gets closer to the Student's curve with increasing number of tested sample. Figure 6.19 shows elastic, plastic and total strain amplitude versus number of reversals plotted on different graphs due to better overview.

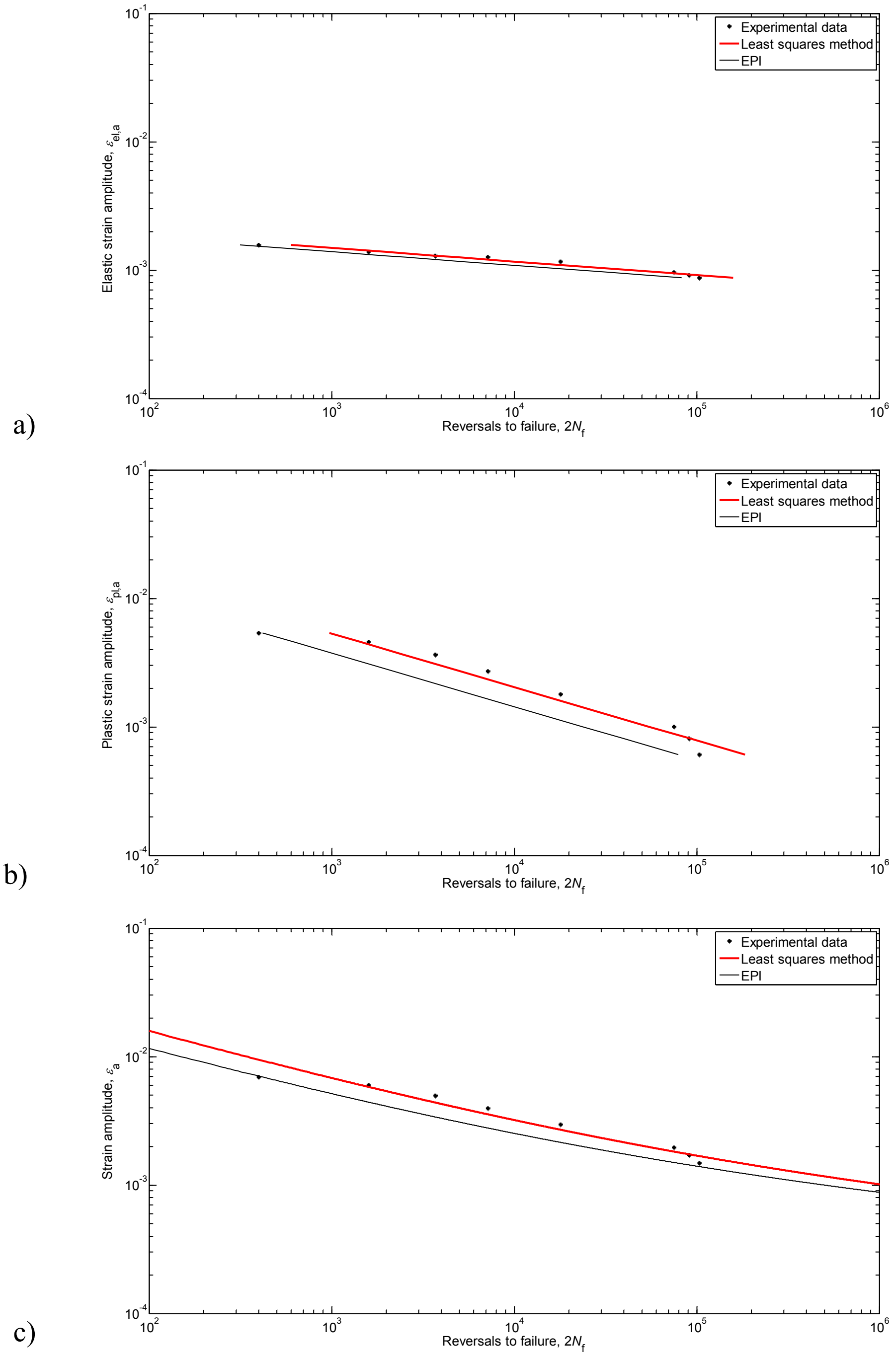

Figure 6.19: Least squares method vs. design curve - EPI

Figure 6.20 shows comparison between design curves obtained with the deterministic approach, the tolerance interval and the EPI method considering the CuAg alloy at different temperature levels. Utilized parameters are summarized in Table 6.4, Table 6.5 and Table 6.6 with respect to temperature that has been used during the estimation procedure. All curves consider the probability of failure *β*=10%. As it can be noticed, the most conservative curve for all three temperature levels is the one calculated with the tolerance interval, while the deterministic approach gives the less conservative curve. The tolerance interval method is suggested to use from designing point of view to be on the safe side.

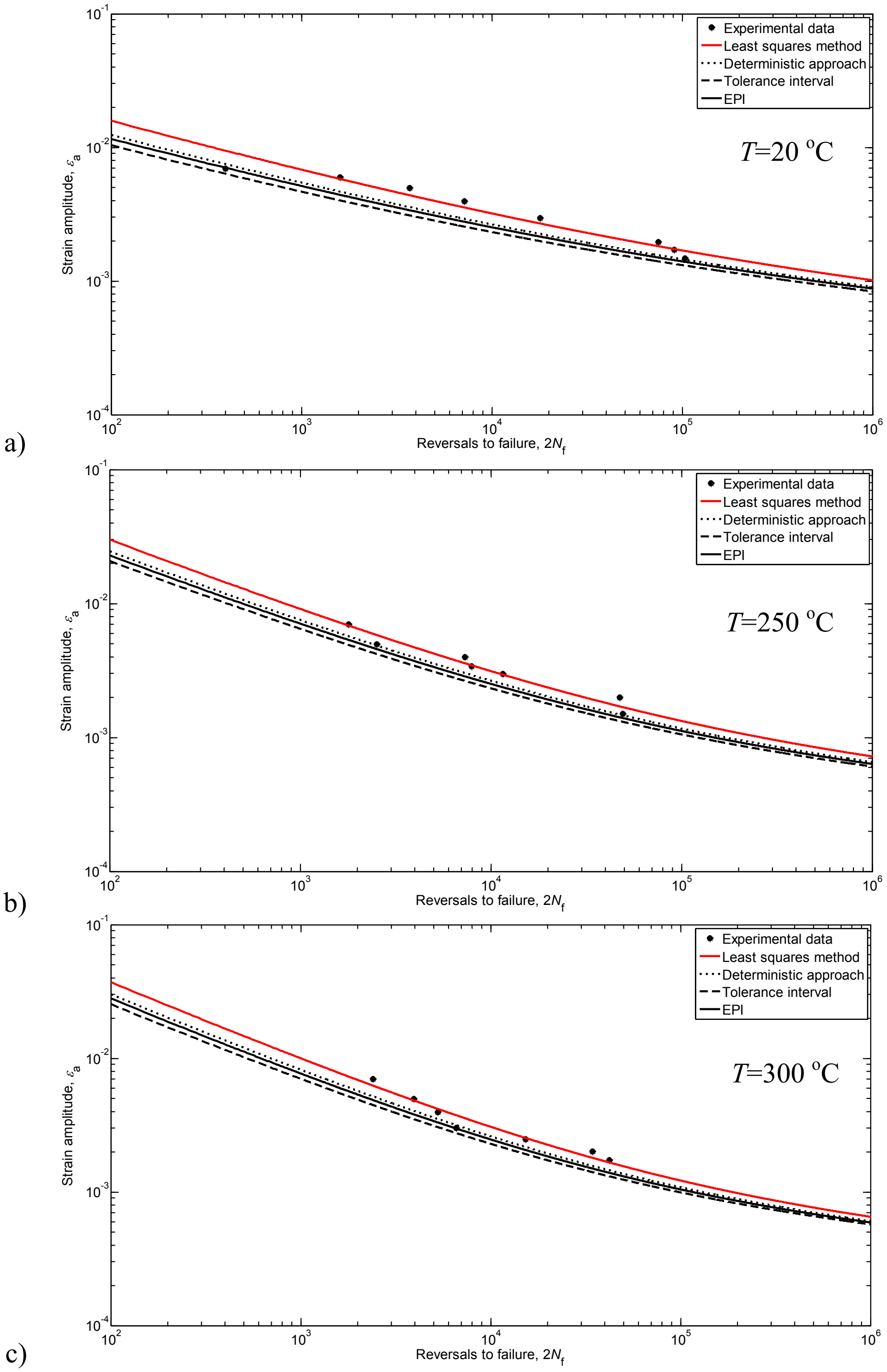

Figure 6.20: Design curves at different temperatures

Parameters for the deterministic approach, the tolerance interval method and for the EPI method have been estimated considering the probability of survival equal to β=10%. Furthermore, LCF data of CuAg alloy at three temperature levels have been used during the estimation procedure. All estimated parameters are summarized in the following tables with respect to temperature.

Table 6.4: Estimated parameters for design curves – T=20 ^{O}C

	σ_f'/E (MPa)	b^*	ε_f'	c
Linear regression (β=50%)	0.00311	-0.1065	0.09485	-0.4167
Deterministic approach (β=10%)	0.00295	-0.1065	0.07201	-0.4167
Tolerance interval method (β=10%, δ=90)	0.00283	-0.1065	0.05886	-0.4167
EPI (β=10%)	0.00291	-0.1065	0.06683	-0.4167

Table 6.5: Estimated parameters for design curves – T=250 ^{O}C

	σ_f'/E (MPa)	b^*	ε_f'	c
Linear regression (β=50%)	0.00264	-0.1133	0.3666	-0.5551
Deterministic approach (β=10%)	0.00247	-0.1133	0.2975	-0.5551
Tolerance interval method (β=10%, δ=90)	0.00235	-0.1133	0.2506	-0.5551
EPI (β=10%)	0.00242	-0.1133	0.2769	-0.5551

Table 6.6: Estimated parameters for design curves – T=300 ^{O}C

	σ_f'/E (MPa)	b^*	ε_f'	c
Linear regression (β=50%)	0.00244	-0.1125	0.5747	-0.6035
Deterministic approach (β=10%)	0.00234	-0.1125	0.4626	-0.6035
Tolerance interval method (β=10%, δ=90)	0.00227	-0.1125	0.3872	-0.6035
EPI (β=10%)	0.00231	-0.1125	0.4294	-0.6035

6.10 Life assessment in terms of material models and fatigue models

Various material models, able to numerically simulate cyclic elasto-plastic material behaviour, are described in Chapter 5. The equivalent strain range is needed to calculate in order to investigate correlation between various material models and fatigue models. The strain is always triaxial even if in a component the stress state is uniaxial. In case of multiaxial stress and strain states, the equivalent strain range ($\Delta\varepsilon_{\mathrm{eq}}$) has to be calculated:

$$\Delta\varepsilon_{\mathrm{eq}}=\frac{\sqrt{2}}{3}\sqrt{\left[\Delta\left(\varepsilon_1-\varepsilon_2\right)\right]^2+\left[\Delta\left(\varepsilon_2-\varepsilon_3\right)\right]^2+\left[\Delta\left(\varepsilon_3-\varepsilon_1\right)\right]^2} \tag{6.41}$$

where $\Delta(\varepsilon_i$-$\varepsilon_j)$ is the range of the difference between principal strains. Correction of the elastic part in equations (6.8), (6.10) and (6.11) must be done as suggested in [Manson, 1966] before proceeding with determination of a service life. The elastic part in equations must be shifted downward:

$$\frac{\Delta\varepsilon_{\mathrm{eq}}}{2}=\left[\frac{2}{3}(1+v)\right]\frac{\sigma_{\mathrm{f}}'}{E}\left(2N_{\mathrm{f}}\right)^{b^*}+\varepsilon_{\mathrm{f}}'\left(2N_{\mathrm{f}}\right)^{c} \tag{6.42}$$

$$\Delta\varepsilon_{\mathrm{eq}}=\left[\frac{2}{3}(1+v)\right]3.5\frac{\sigma_{\mathrm{uts}}}{E}N_{\mathrm{f}}^{-0.12}+D^{0.6}N_{\mathrm{f}}^{-0.6} \tag{6.43}$$

$$\Delta\varepsilon_{\mathrm{eq}}=\left[\frac{2}{3}(1+v)\right]1.17\left(\frac{\sigma_{\mathrm{uts}}}{E}\right)^{0.832}N_{\mathrm{f}}^{-0.09}+0.0266D^{0.155}\left(\frac{\sigma_{\mathrm{uts}}}{E}\right)^{-0.53}N_{\mathrm{f}}^{-0.56} \tag{6.44}$$

Figure 6.21 shows the comparison between strain-life curves calculated with respect to different methods explained so far and using parameter estimated from experimental data of CuAg alloy. The Universal Slopes curves are obtained considering material parameters estimated from tensile test data at 20 $^{\mathrm{o}}$C and 250 $^{\mathrm{o}}$C, respectively. The Universal Slopes equation has been applied for CuAg alloy at room temperature and at elevated temperature (T=250 $^{\mathrm{o}}$C) in this work. Although, the originally Universal Slopes equation is suggested to use for steel at room temperature. The Modified Universal Slopes curve is obtained with material parameters estimated from tensile test data at 250 $^{\mathrm{o}}$C. The Manson-Coffin-Basquin curve is calculated with parameters identified from LCF data at 250 $^{\mathrm{o}}$C. As can be seen in Figure 6.21, the Universal Slopes curve (T=20 $^{\mathrm{o}}$C - upper bound life) seems to be under conservative compared to the Universal Slopes curve (T=250 $^{\mathrm{o}}$C). Therefore, 10% Rule (lower bound) and 20% Rule (average) are calculated based on the Universal Slopes for T=250 $^{\mathrm{o}}$C to be on the safe side. It is worth noting how 10% Rule seem to be over conservative, at least for this type of alloy and at this temperature. Quite surprisingly, shape of the Modified Universal Slopes curve is very similar to the Manson-Coffin-Basquin curve. However, the Modified Universal Slopes is situated in under conservative part. A quite good agreement and similarity between Manson-Coffin-Basquin (250 °C) and Universal Slopes (250 °C) curves is observed in the region beyond $\Delta\varepsilon_{eq}$=0.003.

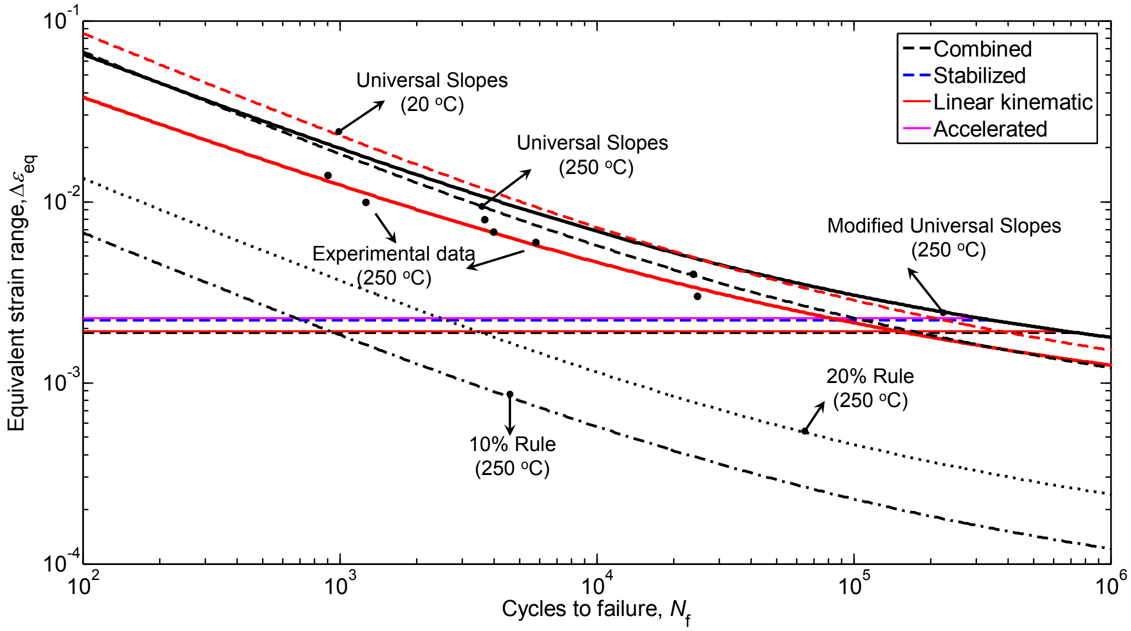

Figure 6.21: Equivalent strain range vs. number of cycles to failure – Fatigue models

The fatigue life of the copper mould is estimated with respect to the most critical point A, described and discussed in Chapter 5. The critical point A corresponds to the place in which occurs the highest thermal gradient across the thickness, simultaneously causing high thermal stresses. Mechanical analyses are performed adopting the several material models (combined model, stabilized, linear kinematic and accelerated models), where temperature dependence of material parameters have been also taken into consideration. The fatigue life for the most critical point A is calculated considering different material models used in simulations as well as several fatigue curves (experimental curve 250 °C, Universal Slopes 20 °C, Universal Slopes 250 °C, Modified Universal Slopes 250 °C, 10% and 20% Rule), see Table 6.7.

Table 6.7: Fatigue life estimation with respect to the critical point A and considering fatigue models

Material Models	$\Delta\varepsilon_{eq}$	Number of cycles to failure					
		Experimental data (250°C)	Universal Slopes (20°C)	Universal Slopes (250°C)	10% Rule (250°C)	20% Rule (250°C)	Modified Universal Slopes (250°C)
Combined	0.00189	161141	401424	182499	959	3618	732596
Stabilized	0.00221	90147	229276	110928	717	2651	347168
Linear kin.	0.00193	148310	369460	167967	920	3471	660419
Accelerated	0.00226	82969	211020	102096	688	2543	319524

Results summarized in Table 6.7 show that similar fatigue lives are calculated with the combined and the linear kinematic material models, regardless of the fatigue curve. This is due to fact that the combined material model requires 60567 cycles to reach stabilized stress-strain state; its response after 20 cycles is almost similar to the linear kinematic one. On the other hand, with the stabilized material model plasticization phenomena area enhanced in the first cycles due to the lower yield stress, σ_{0*}. In fact, it has been observed in [Chaboche, 1986b] that direct use of the stabilized model could leads to heavy mistakes especially in the case of softening materials. Therefore, the accelerated material model seems to be a good compromise among the previously discussed approaches. Figure 6.22 shows results taken from the Table 6.7 and expressed in percentage, where 100% is a sum of fatigue lives obtained with different material models for each fatigue model, respectively. Observing Table 6.7 and Figure 6.22 can be noticed that the accelerated model predicts the lowest fatigue life for all 6 fatigue curves. Therefore, the accelerated method seems suitable to use according to safe engineering design. On the other hand, the combined material model predicts the highest life prediction.

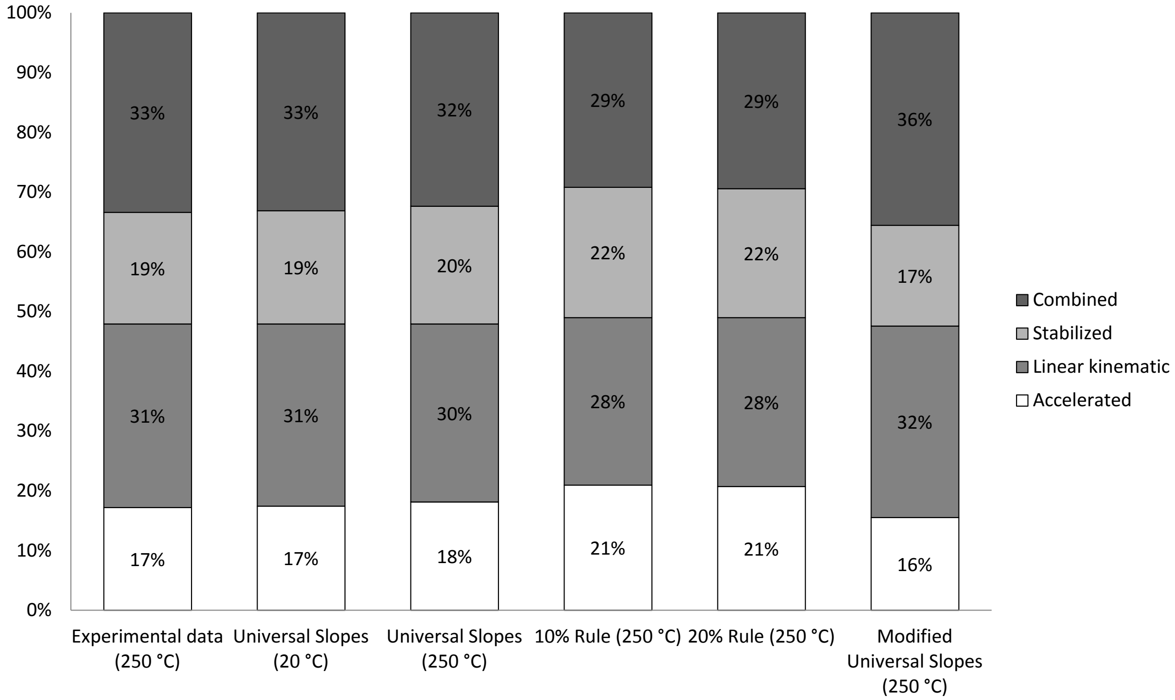

Figure 6.22: Graphical demonstration of Table 6.7 expressed in percentage

Figure 6.23 shows the comparison between several material models (combined model, stabilized, linear kinematic and accelerated models) and design curves (deterministic approach, tolerance interval, EPI). Design curves are calculated considering low cycle fatigue data of CuAg alloy at T=250 ^{o}C and the probability of failure β=10%. As in previous case, the fatigue life of the copper mould is estimated with respect to the most critical point A. Therefore, equivalent strain ranges in both cases are the same since the same material models and the same critical point have been considered.

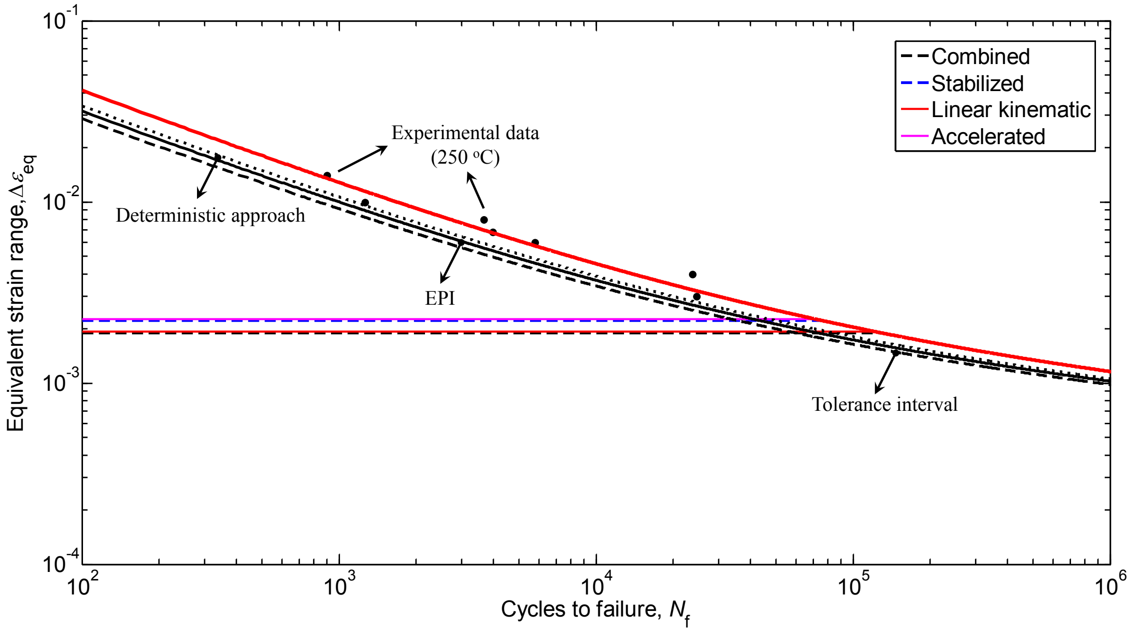

Figure 6.23: Equivalent strain range vs. number of cycles to failure - Design curves (T=250 °C)

Observing Figure 6.23 can be noticed that all design curve are situated left with respect to experimental curve obtained with the Manson-Coffin-Basquin parameters for T=250 °C. As a consequence, all design curves predict lowest fatigue life. However, the lowest fatigue life is predicted with the tolerance interval curve, confirming that it is the most conservative with respect to other design curves (deterministic approach and EPI), see Figure 6.23, Figure 6.24 and Table 6.8.

Table 6.8: Fatigue life estimation with respect to the critical point A and considering design curves

Material Models	$\Delta\varepsilon_{eq}$	Number of cycles to failure			
		Experimental data (250°C)	Deterministic approach	Tolerance interval	Equivalent prediction interval (EPI)
Combined	0.00189	161141	85130	60140	73580
Stabilized	0.00221	90147	50470	35890	43750
Linear kin.	0.00193	148310	79170	55980	68460
Accelerated	0.00226	82969	47000	33440	40750

Figure 6.24 presents results taken from the Table 6.8 and expressed in percentage, where 100% is a sum of fatigue lives obtained with different material models for each design curve model, respectively. Based on obtained results and in terms of design curves the tolerance interval method is suggested to use from designing point of view to be on the safe side.

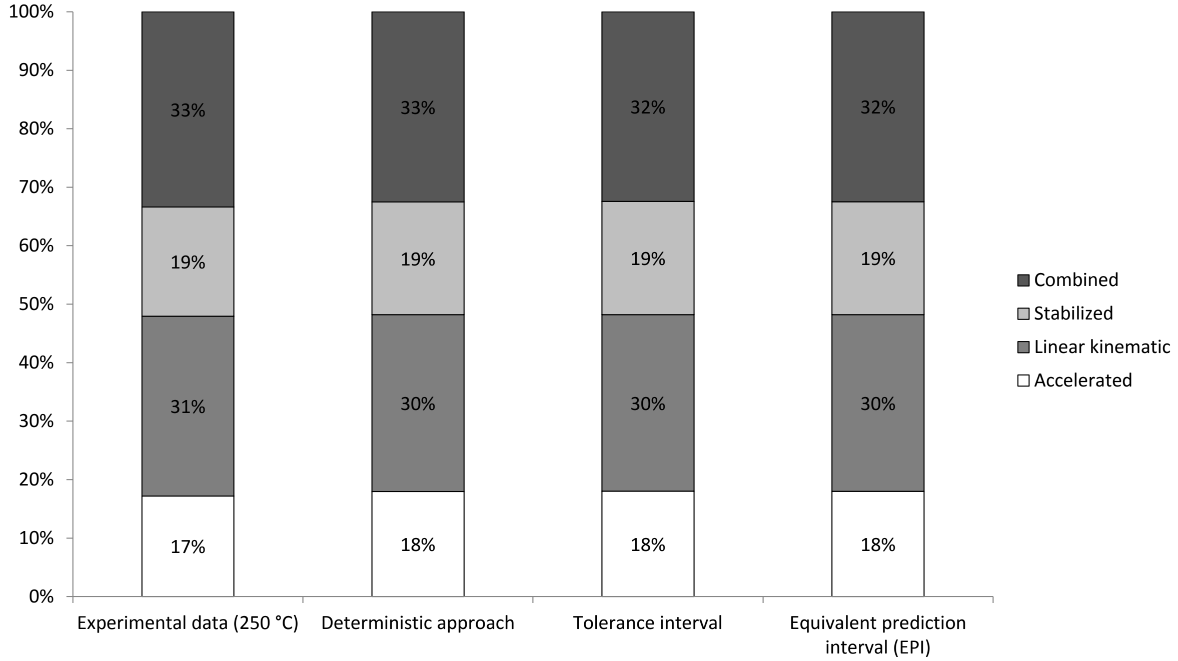

Figure 6.24: Graphical demonstration of Table 6.8 expressed in percentage

Chapter 7

Conclusions

As a contribution to material modelling and parameter identification, this research work has investigated behaviour of a component subjected to cyclic thermal loads and assessment of fatigue lives considering several material and fatigue models, respectively. The copper mould was taken into consideration as a case study. Therefore, the thermo-mechanical analysis of the copper mould for the continuous steel casting was described and analysed.

Firstly, the numerical simulations and sensitivity analyses were performed, presented and described in Chapter 3, with the aim to get the overview and the link between theoretical part and practical use of several material models. The numerical simulations were done with respect to the three different material models (the Armstrong and Frederick' model, the nonlinear isotropic and the combined model). As could be seen, the nonlinear kinematic model is able to capture monotonic hardening and Bauschinger effect; while with the nonlinear isotropic model is possible to simulate cyclic hardening or softening phenomena. Combination of the nonlinear kinematic and nonlinear isotropic model is appropriate for applications subjected to cyclic loading where monotonic hardening, Bauschinger effect and cyclic hardening or softening phenomena is needed to capture. The sensitivity analyses were shown which parameters do really affect and how on the material response.

During the work, one of the most challenging steps was to define a suitable material model for the thermo-mechanical analysis of a component subjected to cyclic thermal loads in order to produce meaningful results; since amount of the resulting plastic and the elastic strain is controlled by the material model. The combined (nonlinear kinematic and nonlinear isotropic) material model was found to be the most suitable and reliable for applications subjected to cyclic loadings among various elasto-plastic material models available in the literature. This was also confirmed with the numerical simulation performed in Chapter 3. Appropriate identification procedures for the nonlinear kinematic and the nonlinear isotropic parameters were necessary to selected before proceeding with the analysis; since several different approaches are suggested to use in the literatures. The identification procedure for the nonlinear kinematic and the nonlinear isotropic parameters were done separately using experimental isothermal low-cycle fatigue data of CuAg alloy at different temperatures levels (20 °C, 250 °C, 300 °C).

During the literature review, it was observed that many authors use two and more pairs of material parameters (C_i, γ_i) without explaining and justifying reasons. In this work, it was demonstrated that one pair of material parameter (C_i, γ_i) provides satisfactory agreement between the experimental and the simulated stress-strain loops. Parameters calibration should be performed step-by-step and as precise as possible to obtain quality parameters. Using poorly estimated parameters in numerical analyses can give misleading even wrong results what can be very dangerous, since the stress-strain response of a component is closely related with the lifetime prediction.

Requirement of huge computational time (≈630 days) to capture the stabilized condition with the adopted combined model was discovered once the material parameters had been calibrated and the thermo-mechanical analysis had been performed. Since 630 days of simulation is unfeasible to perform, some alternative material models (the stabilized, the linear kinematic and the accelerated model) were investigated and adopted. As it is well known, the linear kinematic model is incapable to simulate cyclic hardening or softening behaviour of a material. However, simplicity of its estimation procedure makes it suitable to use at very early stage of the designing process to get an overview of component response; before performing expensive and extensive experimental tests. With a further investigation, it was noticed that direct use of stabilized model could lead to heavy mistakes, especially in the case of softening materials. The accelerated model, which takes into consideration speed of stabilization, seemed to be a good compromise among the previously discussed models. Based on obtained results, the accelerated model was proposed to use when huge number of cycles are needed to simulate before reaching stabilized condition. The accelerated model is suitable especially for industrial applications, where the choice of a material model is usually a result of balancing and compromising between computational time, model complexity, availability of experimental data to estimate material parameters etc.

Several strain-based fatigue models (i.e Manson-Coffin-Basquin, Universal Slopes equation, Modified Universal Slopes equation, 10% Rule and 20% Rule) were investigated and discussed in the second part of the thesis. The main focus was on the alternative fatigue models (Universal Slopes equation, Modified Universal Slopes equation, 10% Rule and 20% Rule) whose parameters can be estimated using tensile test data. These models were investigated because in most cases conducting an extensive experimental test, especially at beginning of research, cannot be performed. The alternative fatigue models are able to preliminary assess a fatigue life without involving prior knowledge of fatigue behaviour. However, awareness of the facts should be present that all these fatigue models neglect some important effects as for instance creep, influence of temperature and difference between monotonic and cyclic tests. Neglecting some of those effects contribute of using 10% Rule and 20% Rule to be on the safe side during assessment of a fatigue life.

Mostly in literatures, problems related with material characterization and lifetime predictions are addressed separately. Systematic investigation is preformed considering correlation between several material models and fatigue models as well as design curves in this work. From designing point of view, the main intention of this research work was to point out and to clarify that sometimes in order to obtain a survey of a component behaviour and life prediction, balance between choosing very sophisticated but complex and simplified numerical, material and fatigue models is necessary to make. All steps should be at the same level of approximation. First of all, developing and analysing very complex numerical models require powerful computational memory, time, so most of the time is necessary to model and to use simplified numerical model able to capture relevant phenomenon. Moreover, in some cases as happened in this work, using of the most suitable and complex combined material model requires unfeasible computational effort and time to reach the stabilized stress-strain loop.

Acknowledgments

First and foremost, I would like to express my sincere gratitude to Professor Denis Benasciutti, Professor Francesco De Bona, Professor Mircea Gh Munteanu and PhD Luciano Moro for their continuous support, helpful suggestions, patience and guidance throughout this research. It has been an honor and pleasure working with ***You.***

My sincere thanks go to the Professor Florian Grun and Aleksandar Stanojevic (Montanuniversity Leoben, Austria) on an academic collaboration and support during the Erasmus exchange program.

I am grateful to PhD Alex Lanzutti for generously sharing his time and knowledge during metallurgical analysis of the copper mould.

I gratefully acknowledge the members of my dissertation committee, Professors Paolo Livieri and Saša Zelenika for their time and critical comments which enabled me to make necessary improvements of my thesis.

Veliku zahvalnost dugujem svojim roditeljima Zlatku i Štefaniji te bratu Tomici na bezuvjetnoj podršci tijekom cijelog školovanja, na stalnom ohrabrivanju i neizmjernoj vjeri u moj uspjeh.

I na kraju, nikada dovoljno reci HVALA mojem suprugu Velimiru na svakodnevnom strpljenju, razumijevanju i podršci. Hvala ti što si bio uz mene u svim onim trenucima, ohrabrivao me i vjerovao u mene.

Ovaj rad posvećujem svojoj obitelji.
Konačno ste me odškolovali!!!

Bibliography

[Ansoldi, 2012] Ansoldi M., Bazzaro G., Benasciutti D., De Bona F., Luvarà G., Moro L., Munteanu M. Gh. and Vecchiet F.: Thermo-Mechanical Analysis of a Copper Mould for Continuous Casting of Steel, In International NT2F12 Congress, Brasov (RO), May 2012.

[Ansoldi, 2013] Ansoldi M., Bazzaro G., Benasciutti D., De Bona F., Luvarà G., Moro L., Munteanu M. Gh. and Vecchiet F.: Thermo-Mechanical Analysis of a Copper Mould for Continuous Casting of Steel. Proc. 7th Int. Conference on Low Cycle Fatigue "LCF7", Aachen, 9-11 September 2013, pp. 527-532 (ISBN 978-3-9814516-2-7).

[ASM, 2000] ASM Handbook: *Mechanical Testing and Evaluation*, Vol. 8, October 2000.

[ASM, 2004] ASM International: *Tensile Testing*, Second edition, 2004

[ASTM] ASTM International: Standard Test Methods for Tension Testing of Metallic Materials, E 8-04.

[Barella, 2014] Barella S., Gruttadauria A., Mapelli C., Mombelli D.: Investigation of Failure and Damages on a Continuous Casting Copper Mould, *Engineering Failure Analysis*, Vol. 36: 432-438, 2014.

[Besson, 2010] Besson J., Cailletaud G., Chaboche J. L. and Forest S.: *Non-Linear Mechanics of Materials*, Springer Dordrecht Heidelberg London New York, 2010.

[Broggiato, 2008] Broggiato G. B., Campana F. and Cortese L.: The Chaboche Nonlinear Kinematic Hardening Model: Calibration Methodology and Validation, *Meccanica*, Vol. 43: 115-124, 2008.

[Budahazy, 2013] Budahazy L. and Dunai L.: Parameter-Refreshed Chaboche Model for Mild Steel Cyclic Plasticity Behavior, *Civil Engineering*, Vol. 57, No. 2: 139-155, 2013.

[Chaboche, 1983a] Chaboche J. L. and Rousselier G.: On the Plastic and Viscoplastic Constitutive Equations – Part I: Rules Developed With Internal Variable Concept, *Journal of Pressure Vessel Technology*, Vol. 105: 153-158, 1983.

[Chaboche, 1983b] Chaboche J. L. and Rousselier G.: On the Plastic and Viscoplastic Constitutive Equations – Part II: Application of Internal Variable Concepts to the 316 Stainless Steel, *Journal of Pressure Vessel Technology*, Vol. 105: 159-164, 1983.

[Chaboche, 1986a] Chaboche J. L.: Time-Independent Constitutive Theories for Cyclic Plasticity, *International Journal of Plasticity*, Vol. 2, No. 2: 149-188, 1986.

[Chaboche, 1986b] Chaboche J. L. and Cailletaud G.: On the Calculation of Structures in Cyclic Plasticity or Viscoplasticity, *Computers & Structures*, Vol. 23: 23-31, 1986.

[Chaboche, 1989] Chaboche J. L.: Constitutive Equations for Cyclic Plasticity and Cyclic Viscoplasticity, *International Journal of Plasticity*, Vol. 5: 247-302, 1989.

[Chaboche, 2008] Chaboche J. L: A Review of Some Plasticity and Viscoplasticity Constitutive Theories, *International Journal of Plasticity*, Vol. 24: 1642-1693, 2008.

[Chen, 1988] Chen W. F. and Han D. J.: *Plasticity for Structural Engineers*, Springer-Verlang, New York, 1988.

[Coffin, 1972] Coffin L. F. Jr.: *Fatigue*, Corporate Research and Development, General Electric Company, Schenectady, New York, 1972.

[Desmorat, 2005] Desmorat L. R.: *Engineering Damage Mechanics*, Springer-Verlag, Berlin Heidelberg, 2005.

[Dunne, 2005] Dunne F. and Petrinic N.: *Introduction to Computational Plasticity*, University press, Oxford, 2005.

[Edward, 1997] Edward Pope J.: *Rules of Thumb for Mechanical Engineers*, Golf Publishing Company, Houston, 1997.

[Elfsberg, 2003] Elfsberg J.: *Oscillation Mark Formation in Continuous Casting Processes*, Royal Institute of Technology, Stockholm, Sweden, 2003.

[Franulović, 2009] Franulović M., Basan R. and Prebil I.: Genetic Algorithm in Material Model Parameters' Identification for Low-Cycle Fatigue, *Computational Material Science*, Vol. 45: 505-510.

[Franulović, 2014] Franulović M., Basan R. and Krizan B.: Kinematic Hardening Parameters Identification with Respect to Objective Function, International Scholarly and Scientific Research & Innovation, Vol. 8, No. 4: 685-689, 2014.

[Gong, 2009] Gong Y., Hyde C. J., Sun W. and Hyde T. H.: Determination of Material Properties in the Chaboche Unified Viscoplasticity Model, *Proc. IMechE, Part L: J. Materials Design and Applications*, Vol. 224: 19-29, 2009.

[Halama, 2012] Halama R., Sedlak J. and Šofer M.: *Phenomenological Modelling of Cyclic Plasticity*, Numerical Modelling edited by Peep Miidla, 329-351. Intech, 2012.

[Hales, 2002] Hales R., Holdsworth S. R., O'Donnell M. P., Perrin I. J. and Skelton, R. P.: A Code of Practice for Determination of Cyclic Stress-Strain Data, *Materials at high temperature* Vol. 19, No. 4: 165-185, 2002.

[Halford, 1986] Halford G. R.: Low-Cycle Thermal Fatigue, *NASA Technical Memorandum 87225*, Cleveland, Ohio, February, 1986.

[Halford, 1987] Halford G. R. and Saltsman J. F.: Calculation of Thermomechanical Fatigue Life Based on Isothermal Behavior, *5th National Congress on Pressure Vessel And Piping Technology*, San Diego, California, June 28 - July 2, 1987.

[Hu, 1999] Hu W., Wang C. H. and Barter S: *Analysis of Cyclic Mean Stress Relaxation and Strain Ratchetting Behaviour of Aluminium 7050*, DSTO Aeronautical and Maritime Research Laboratory, Victoria, 1999.

[Imaoka, 2008] Imaoka S.: *Chaboche Nonlinear Kinematic Hardening Model*, Memo Number: STI0805A, May 4, 2008.

[Khan, 1995] Khan A. S. and Huang S.: *Continuum Theory of Plasticity*, John Wiley & Sons, New York, 1995.

[Koo, 2011] Koo G. H. and Kwon J. H.: Identification of Inelastic Material Parameters for Modified 9Cr-1Mo Steel Applicable to the Plastic and Viscoplastic Constitutive Equations, *International Journal of Pressure Vessels and Piping*, Vol. 88: 26-33, 2011.

[Lee, 2005] Lee J. L., Hathaway R. B. and Barkey M. E.: *Fatigue Testing and Analysis (Theory and Practice)*, Elsevier Butterworth-Heinemann, 2005.

[Lee, 2009] Lee J. H, Kim K. S., Lee J. B. Yang Y. S. and Yoo M. J.: A Numerical Simulation Model of Cyclic Hardening Behaviour of AC4C-T6 for LNG Cargo Pump Using Finite Element Analysis, Journal of Loss Prevention in the Process Industries, Vol. 22: 889-896, 2009.

[Lee, 2012] Lee Y. L., Barkey M. E. and Kang H. T.: *Metal Fatigue Analysis Handbook*, Butterworth-Heinemann, 2012.

[Lemaitre, 1990] Lemaitre J. and Chaboche J. L.: *Mechanics of Solid Materials*, Cambridge University Press, Cambridge, 1990.

[Lemaitre, 2005] Lemaitre J. and Desmorat R.: *Engineering Damage Mechanics Ductile, Creep, Fatigue and Brittle Failures*, Springer-Verlag Berlin Heidelberg, 2005.

[Li, 2016] Li Mi., Barrett R. A., Scully S., Harrison N. M., Lee S. B. and O'Donoghue P. E.: Cyclic Plasticity of welded P91 material for simple and complex power plant connections, *International Journal of Fatigue*, InPress, 2016.

[Mahapatra, 1991a] Mahapatra R. B., Brimacombe J. K., Samarasekera I. V., Walker N., Paterson E. A. and Young J. D.: Mold Behavior and Its Influence on Quality in the

Continuous Casting of Steel Slabs: Part I. Industrial Trials, Mold Temperature Measurements, and Mathematical Modeling, *Metallurgical Transactions B*, Vol. 22B: 861-874, December, 1991.

[Mahapatra, 1991b] Mahapatra R. B., Brimacombe J. K. and Samarasekera I. V: Mold Behavior and Its Influence on Quality in the Continuous Casting of Steel Slabs: Part II. Mold Heat Transfer, Mold Flux Behavior, Formation of Oscillation Marks, Longitudinal Off-Corner Depressions, and Subsurface Cracks, *Metallurgical Transactions B*, Vol. 22B: 875-888, December, 1991.

[Manson, 1965] Manson S. S.: Fatigue: A Complex Subject – Some Simple Approximations, *Experimental Mechanics*, July, 1965.

[Manson, 1966] Manson S. S.: *Thermal Stress and Low-Cycle Fatigue*, McGraw-Hill, 1966.

[Manson, 1967] Manson S. S. and Halford G.: A Method of Estimating High Temperature Low Cycle Fatigue Behavior of Metals, *Symposium on Thermal and High Strain Fatigue*, London, 1967.

[Manson, 1968] Manson S. S.: A Simple Procedure for Estimating High-temperature Low-Cycle Fatigue, *Experimental Mechanics*, Vol. 8: 349-355, 1968.

[Manson, 2006] Manson S. S. and Halford G. R.: *Fatigue and Durability of Structural Materials*, ASM International, 2006.

[Manson, 2009] Manson S. S. and Halford G. R.: *Fatigue and Durability of Metals at High Temperature*, ASM International, 2009.

[Martinez, 2002] Martinez W. L. and Martinez A. R.: *Computational Statistic Handbook with MATLAB*, Champman & Hall/CRC, 2002.

[Marques, 2007] [Marques de Sa J. P.: *Applied Statistics Using SPSS, STATISTIKA, MATLAB and R*, Springer-Verlag Berlin Heidelberg, 2007.]

[Montgomery, 2003] Montgomery D. C. and Runger G. C.: *Applied Statistics and Probability for Engineers*, John Wiley & Sons, New York, 2003.

[Nieslony, 2008] Nieslony A., el Dsoki C., Kaufmann H. and Krug P.: New Method for Evaluation of the Manson-Coffin-Basquin and Ramberg-Osgood Equations with Respect to Compatibility, *International Journal of Fatigue*, Vol. 30: 1967-1977, 2008.

[Pajand, 2009] Rezaiee-Pajand M. and Sinaie S.: On the Calibration of the Chaboche Hardening Model and a Modified Hardening Rule for Uniaxial Ratcheting Prediction, *International Journal of Solids and Structures*, Vol. 46: 3009-3017, 2009.

[Park, 2002a] Park J. K., Thomas B. G., Samarasekera I. V. and Yoon U.S.: Thermal and Mechanical Behavior of Copper Molds During Thin-Slab Casting (I): Plant Trial and Mathematical Modeling, *Metallurgical and Materials Transactions*, Vol. 33B: 1-12, 2002.

[Park, 2002b] Park J. K., Thomas B. G., Samarasekera I. V. and Yoon U. S.: Thermal and Mechanical Behavior of Copper Molds During Thin-Slab Casting (II): Mold Crack Formation, *Metallurgical and Materials Transactions*, Vol. 33B: 437-449, 2002.

[Pope, 1997] Pope E. J.: *Rules of Thumb for Mechanical Engineers*, Golf Publishing Company, Houston, Texas, 1997.

[Schneider, 2003] Schneider C. R. A. and Maddox S. J.: Best Practice on Statistical Analysis of Fatigue Data, International Institute of welding, Camridge UK, 2003.

[Schijve, 2001] Schijve J.: *Fatigue of Structures and Materials*, Kluwer Academic Publishers, Dordrecht, 2001.

[Silvestre, 2015] Silvestre E., Mendiguren J., Galdos L. and Saenza de Argandona E.: Comparison of the Hardening Behaviour of Different Steel Families: from Mild and Stainless Steel to Advanced High Strength Steels, *International Journal of Mechanical Sciences*, July, 2015.

[Stephens, 2001] Stephens R. I., Fatemi A., Stephens R. R. and Fuchs H. O.: *Metal Fatigue in Engineering*, John Wiley & Sons, New York, 2001.

[Suresh, 1998] Suresh S.: *Fatigue of Materials*, Cambridge University Press, 1998.

[Thomas, 1997] Thomas B. G., Li G., Moitra A. and Habing D.: Analysis of Thermal and Mechanical Behaviour of Copper Molds During Continuous Casting of Steel Slabs, 80th Steelmaking Conference, Chicago (IL), April 1997.

[Thomas, 2002] Thomas B. G.: Modeling of the Continuous Casting of Steel – Past, Present, and Future, *Metallurgical and Material Transactions*, Vol. 33B: 795-812, 2002.

[Tong, 2003] Tong J. and Vermeulen B.: The Description of Cyclic Plasticity and Viscoplasticity of Waspaloy Using Unified Constitutive Equations, *International Journal of Fatigue*, Vol. 25: 413-420, 2003.

[Tong, 2004] Tong J., Zhan Z.-L. and Vermeulen B.: Modelling of Cyclic Plasticity and Viscoplasticity of a Nickel-Based Alloy Using Chaboche Constitutive Equations, *International Journal of Fatigue*, Vol. 26: 829-837, 2004.

[Williams, 2003] Williams C. R., Lee Y.-L. and Rilly J. T.: A practical method for statistical analysis of strain-life fatigue data, *International Journal of Fatigue*, Vol. 25.: 427-436, 2003.

[Wirsching, 1980] Wirsching P. H., ASCE A. M. and Hsieh S.: Linear Model in Probabilistic Fatigue Design, *Journal of the Engineering Mechanics Division*, Vol, 106: 1266-1278, 1980.

[Wirsching, 1983] Wirsching P. H.: *Statistical Summaries of Fatigue Data for Design Purpose*, NASA Contractor Report 3697, 1983.

[You, 2008] You J. H. and Miskiewicz M.: Material Parameters of Copper and CuCrZr Alloy for Cyclic Plasticity at Elevated Temperatures, *Journal of Nuclear Materials*, Vol. 373: 269-274, 2008.

[Zaletelj, 2011] Zaletelj H., Fajdiga G. and Nagode M.; Numerical Methods for TMF Cycle Modeling, *Journal of Mechanical Engineering*, Vol. 54: 458-494, 2011.

[Zhao, 2001] Zhao L. G., Tong B., Vermeulen B. and Byrne J.: On the Uniaxial

Mechanical Behavior of an Advanced Nickel Based Superalloy at High Temperature, *Mechanics of Materials*, Vol. 33: 593-600, 2001.